

Non-hydrostatic wave modelling of coral reefs with the addition of a porous in-canopy model

M. P. de Ridder

TU Delft and NUS Singapore



Cover picture: coral reef with wave impact. Credit: Brian Zgliczynski, CC BY-NC-ND

TU DELFT AND NUS SINGAPORE

Non-hydrostatic wave modelling of coral reefs with the addition of a porous in-canopy model

by

M. P. DE RIDDER

to obtain the degree of Master of Science
at the Delft University of Technology and National University of Singapore,
to be defended publicly on Wednesday March 7, 2018 at 10:00 AM (GMT+1).

Supervised by

Daily supervisor:	ir. C. M. Nederhoff	Deltares
Thesis committee:	ir. A. A. van Rooijen	Deltares
	dr. ir. R. T. McCall,	Deltares
	dr. ir. V. Babovic,	NUS Singapore
	ir. J. P. Van den Bos,	TU Delft
	Prof. dr. ir. A. J. H. Reniers,	TU Delft

An electronic version of this thesis is available at <http://repository.tudelft.nl/>.



Preface

This master thesis concludes my master Hydraulic Engineering and Water Resource Management at the TU Delft and NUS Singapore. This thesis was carried out at Deltares.

I would like to thank my commission members for their feedback and support. Kees for your daily supervising, practical feedback during the meetings and enthusiastic support. Robert and Arnold for their support regarding the XBeach model and the discussions about the understanding the involved processes. At last many thanks to Ad Reniers, Vladan Babovic and Jeroen van den Bos for their support during the different meetings and their critical feedback. Furthermore, Ap van Dongeren for the support of the implementation of the boundary conditions, which I enjoyed to work on.

Second, I would like to thank my family for their moral support and my fellow graduate students at Deltares for the enjoyable time during the lunch and coffee-breaks. Finally, my friends with whom I had an enjoyable student time.

*Menno de Ridder
Delft
February 2018*



Abstract

One sixth of the world's coastline consist of coral reefs and provide natural flood defence for the people who live in the coastal region behind the reef (Roberts et al., 2002; Ferrario et al., 2014). However, a rising sea level, changing wave conditions and degradation of corals threaten the coastal safety of these reefs (Hoegh-Guldberg et al., 2007; Hughes et al., 2003). Numerical models can be applied to study the reef-hydrodynamics and the effects of coral degradation on the reef-hydrodynamics. When non-linear processes are important or the individual waves need to be determined, a phase resolving model is preferred. Within this thesis two issues regarding the application of non-hydrostatic models to coral reefs were studied.

Due to the large bottom gradient in front of a reef, the offshore boundary has to be located in deep water, which means that frequency dispersion becomes important. The accuracy of frequency dispersion within non-hydrostatic models depends on the number of vertical layers. However, the addition of a vertical layer increases the computational time extremely. Therefore, Smit (2014) developed a reduced two layer non-hydrostatic model (XBeach-nh+) with the assumption of a constant non-hydrostatic pressure in the lower layer. In theory, XBeach-nh+ is capable of modelling the wave transformation from deep to shallow water, but the applied boundary conditions cannot force deep water waves. On top of that XBeach-nh+ has never been properly validated for reef environments.

Furthermore, the corals (growing on the reef flat) have a large effect on the reef-hydrodynamics by dissipating a large part of the wave energy. There exist different formulations to include vegetation into a non-hydrostatic wave model, but these formulations are mainly applicable for cylinder shaped geometries, whereas corals are more complex in shape. Apart from the shape, the in-canopy velocity can be significantly different from the free stream velocity. Therefore, a porous in-canopy model was implemented to model the in-canopy velocity, which was used to determine the canopy-induced force on the depth-averaged flow computation.

Firstly, the inclusion of the second reduced layer improves the dispersion relation up to a relative depth (kh) of 5 for linear waves. A simulation of biochromatic waves over a plane beach showed that XBeach-nh+ is capable of modelling the energy transfer between the major wave

components. Both steeping and reflection of the sub-harmonic were modelled according to the measurements. Furthermore, the validation of random waves over a fringing reef showed the capability of XBeach-nh+ to model the reef-hydrodynamics for different wave conditions (rel. bias of -0.003 for total wave height, -0.081 for LF-waves and -0.103 for the setup). Moreover, the addition of the second reduced layer gives a more robust prediction for all modelled wave conditions, whereas the one-layer model contains more scatter.

Secondly, the in-canopy model captures the canopy-induced force when the canopy parameters were known. Both the in-canopy flow of unidirectional and oscillating flow fields was accurately modelled when the results were compared to the measured velocity through cylinders and corals. Although, the canopy parameters were not always known, it was shown that an un-calibrated in-canopy model, based on porosity and canopy height, gives a competitive result compared to a fully calibrated shear stress formulation. The applicability of XBeach-nh+ in 2-dimensional domain with a coral covered reef flat was shown by modelling a 5 day Swell event at Ningaloo Reef. Reasonably accurate results were achieved when using the in-canopy model, based on the canopy properties.

Contents

1	Introduction	1
1.1	Social relevance	1
1.2	Problem description	2
1.3	Objectives and research questions	4
1.4	Thesis outline and approach	5
2	Background	7
2.1	The definition of coral reefs	7
2.2	Reef hydrodynamics	8
2.3	Effect vegetation on hydrodynamics	10
2.4	In-canopy flow	12
3	XBeach-nh+	17
3.1	Introduction	17
3.2	Formulation	18
3.3	Dispersive behavior	21
3.4	Layer averaged boundary condition	23
3.5	Second order wave interaction in the boundary condition	25
3.6	Effect layer averaged formulation	28
3.7	Effect second order bound waves	30
3.8	Conclusion	31
4	Validation: hydrodynamics	33
4.1	Introduction	33
4.2	Noorloos experiment	34
4.2.1	Model set-up	34
4.2.2	Calibration	35
4.2.3	Results and discussion	36
4.2.4	Sensitivity of the second order wave interaction at the boundary	41

4.3	Buckley experiment	43
4.3.1	Model set-up	43
4.3.2	Calibration	44
4.3.3	Results and discussion	45
4.4	Conclusion	49
5	In-canopy flow model	51
5.1	Conceptual model	51
5.2	Governing equation	52
5.3	Canopy parameters	54
5.4	Numerical implementation	56
5.5	Computation chart	56
6	Validation: in-canopy flow model	59
6.1	Validation: in-canopy flow	59
6.1.1	Model set-up	59
6.1.2	Flume experiment: 1) Lowe 2005	60
6.1.3	Flume experiment: 2) Lowe 2008	61
6.1.4	Results and discussion	61
6.2	Validation of the drag force	65
6.2.1	Model set-up and calibration	65
6.2.2	Results and discussion	65
6.3	Conclusion	75
7	Validation: Ningaloo Reef	77
7.1	Introduction	77
7.2	Data Analysis	77
7.3	Model setup	80
7.3.1	In-canopy model	82
7.4	Results and discussion	84
7.5	Conclusion	91
8	Discussion	93
8.1	XBeach-nh+	93
8.2	Boundary conditions	94
8.3	In-canopy model	95
8.4	Validation resistance	95
8.5	Estimation canopy parameters	96
9	Conclusions and recommendations	97
9.1	Conclusions	97
9.2	Recommendations	100

CONTENTS

A	Noorloos Experiment	113
A.1	Second order wave interaction	113
A.2	Calibration	115
A.3	Results test B4	117
B	Buckley experiment - smooth	121
B.1	Accuracy Buckley experiment	121
B.2	Calibration	121
B.2.1	Grid resolution	121
B.2.2	Breaker steepness and bottom friction	123
B.3	Effect layer distribution	125
C	In-canopy model - bottom correction	127
D	Buckley experiment - rough	129
E	Ningaloo reef	131
E.1	Sensitivity	131
E.2	Results Ningaloo reef - run: shear stress formulation	132
F	Skill scores	135
G	XBeach-nh background	137
G.1	XBeach non hydrostatic	137
G.2	Governing equations	137
G.3	Domain definitions	140
G.4	Numerical domain	141
G.5	Breaking	142

List of symbols

Greek symbols	Description	Unit
α	i) Layer distribution XBeach-nh+ ii) attenuation parameter	[-] [-]
β	Empirical coefficient	$[m^{-1}]$
ϵ	Porosity	[-]
η	Free surface elevation	$[m]$
$\bar{\eta}$	Setup	$[m]$
λ_p	Dimensional plan area (1- ϵ)	[-]
τ	Shear stress	$[N/m^2]$
τ_b	Bottom shear stress	$[N/m^2]$
θ	Wave direction	$[rad]$
μ	Kinematic viscosity	$[m^2/s]$
ξ	Free surface elevation	$[m]$
ρ	Mass density	$[kg/m^3]$
ϕ	Phase	$[rad]$
ω	Radial frequency	$[rad/s]$
Roman Symbols	Description	Unit
a	Amplitude	$[m]$
A_{∞}^{rms}	Orbital excursion length	$[m/rad]$
c	Wave celerity	$[m/s]$
c_g	Group velocity	$[m/s]$
C_M	Inertia coefficient	[-]
C_f	Empirical friction coefficient	[-]
d	water depth	$[m]$
Δu	Velocity difference	$[m/s]$
f	Frequency	$[1/s]$

F_{veg}	Canopy-induced force	[N]
g	Gravitational acceleration	[m/s^2]
h	Water depth	[m]
h_c	Canopy height	[m]
H_s	Significant wave height	[m]
H_{rms}	Root mean squared wave height	[m]
$H_{rms,LF}$	Root mean squared low frequency wave height	[m]
k	Wave number	[rad/m]
K_p	Permeability	[m^2]
q	i) Non-hydrostatic pressure	[N/m^2]
	i) Flux	[m^2/s]
S_{xx}	Radiation stress	[N/m]
T_p	Peak period	[s]
U	Depth averaged velocity	[m/s]
u_1	Layer averaged velocity (layer 1)	[m/s]
u_1	Layer averaged velocity (layer 2)	[m/s]
U_c	In-canopy velocity	[m/s]
U_∞	Free stream velocity	[m/s]
n	Manning friction coefficient	[$s/m^{1/3}$]
P	Pressure	[N]
q	Normalized non-hydrostatic pressure	[m^2/s^2]
t	Time	[s]
z_b	Bed level XBeach	[m]

Acronyms	Description
Rel. bias	Relative bias
SCI	Scatter index
rms	Root mean square
LF-wave	Low frequency wave
nh+2DV	Reduced two layer non-hydrostatic model (XBeach-nh+) with two layers ($\alpha = 0.33$)
nh+1DV	Reduced two layer non-hydrostatic model (XBeach-nh+) with one layers ($\alpha = 0$)
nh	Original depth-averaged non-hydrostatic model (XBeach-nh)
nh+	Reduced two layer non-hydrostatic model (XBeach-nh+) with two layers ($\alpha = 0.33$)

1

Introduction

1.1 Social relevance

One sixth of the world's coastline consist of coral reefs (Roberts et al., 2002). Due to the offshore wave dissipation at the reef crest, these reefs provide natural flood defence for the people who live in the coastal region behind the reef (Ferrario et al., 2014). The number of people who benefit from the coastal safety of a reef is shown Figure 1.1 by country. However, a rising sea level, changing wave conditions and degradation of corals threaten the coastal safety of these reefs (Hoegh-Guldberg et al., 2007; Hughes et al., 2003).

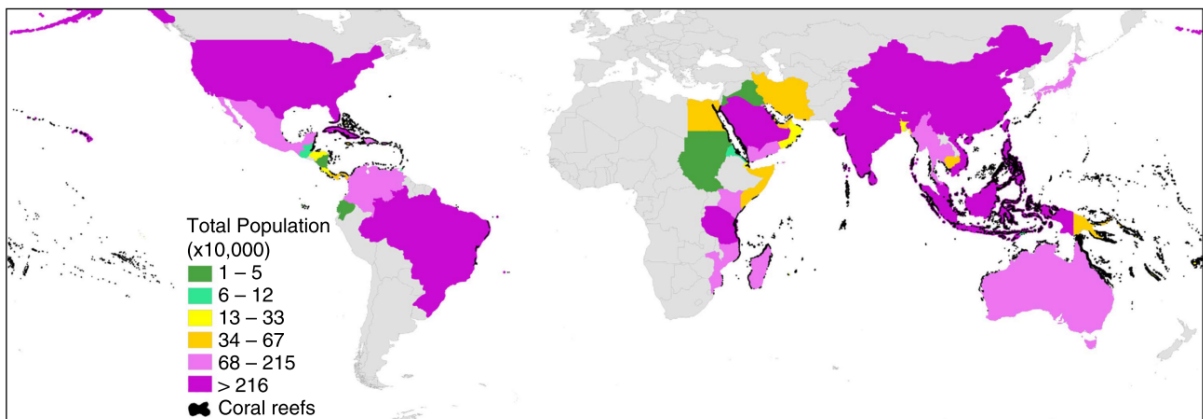


Figure 1.1: Number of people which receive risk reduction benefits from reefs by country (Ferrario et al., 2014). The numbers are based on people who live below 10 m elevation and within 50 km of coral reefs. The grey countries do not have people who meeting these conditions or do not have data. Source: Ferrario et al. (2014)

In particular, low lying islands states (e.g. coral atolls in the Pacific) suffer from sea level rise

as they are not higher than a few meters above mean sea level (Pernetta, 1992), which makes these islands vulnerable for flooding events. In Quataert et al. (2015) it was shown that a higher water level results in larger wave runup for atoll islands. Moreover, a flooding event is not only undesired for their destructive effect, but it also affects the fresh water storage of these islands. With every flooding event, the fresh water storage (which is already limited) decreases and makes the habitability of these islands less straightforward (Holding et al., 2016). Although, the area of these states is relatively small, a total of 63.2 million people live on these islands (Holding et al., 2016). Thus, a flooding event has a large social and economic impact for these islands.

Not only the changing hydrodynamic conditions affect the coastal safety, but also the degradation of corals influence the near-shore hydrodynamics. Corals play an important role in the dissipation of wave energy (Lowe et al., 2005a; Huang et al., 2012). It is estimated that already 30% of the current reefs have been damaged due to sea temperature rise and over-fishing (Hughes et al., 2003). Sheppard et al. (2005) showed that the degradation of corals can lead to coastal erosion and less attenuate wave energy at the shore. Moreover, the reduction of corals can have an impact on the risk of flooding in the coastal zone (Quataert et al., 2015; Ferrario et al., 2014).

To study both the effects of changing hydrodynamic conditions and coral degradation, numerical models can be applied. The major advantage of numerical models is that different scenarios can be modelled and that multiple interventions can be verified (e.g. play so called 'what-if' games). Therefore, it is important that these numerical models predict the reef hydrodynamics accurately and that the coral resistance can easily be included in the wave-study. When coupling these hydrodynamic models to sediment transport rates, it is even possible to model the reef morphologies and ecological processes (Storlazzi et al., 2011).

1.2 Problem description

A wave-model which can be applied for modelling wave transformation over coral reefs is XBeach (Roelvink et al., 2009, 2017). This model is capable of modelling near-shore hydrodynamics and morphology. It was initially developed to model the hurricane impacts on sandy beaches in the United States (McCall et al., 2010). In the meantime, the model is further developed for different kinds of sandy beaches (dissipative and reflective), coral reefs (Quataert et al., 2015; Pearson et al., 2017), wave-vegetation interaction (van Rooijen et al., 2016) and storm impact on gravel beaches (McCall, 2015). The XBeach model contains three modes: the stationary mode, the surf-beat mode (phase-averaged) and the non-hydrostatic mode (phase-resolving). The stationary wave mode only solves the short wave action balance whereas the surf-beat mode solves the short wave action balance and the associated long waves. The non-hydrostatic mode (XBeach-nh) solves the non-linear shallow water equations with the addition of the non-hydrostatic pressure.

A phase-resolving model is preferred when all the non-linear processes should be included

into the wave study (e.g. frequency dispersion and wave interactions). Furthermore, when overwash/runup needs to be determined, a phase-resolving model is preferred since this model makes it possible to simulate both incident and infra-gravity swash. Two types of phase-resolving models are commonly used: boussinesq-type of models (Madsen et al., 1997; Sorensen et al., 1998) and the non-hydrostatic models (Zijlema et al., 2011). The boussinesq-type of models were derived for shallow water and later extended to deeper water. The wave behaviour in deep water is different than shallow water since the wave speed is dependent on the wave length (frequency dispersion), whereas the wave speed is depended on the water depth in shallow water. The accuracy of frequency dispersion in a non-hydrostatic model depends on the number of layers in the vertical (Zijlema et al., 2011), whereas boussinesq-type of models require higher order derivatives terms (Madsen et al., 1991). Therefore, non-hydrostatic models are preferred when modelling deep water waves, because it is much easier to add a vertical layer than to include the higher order terms for a boussinesq-type of model.

The downside of a non-hydrostatic model compared to a phase-averaged model is the computational time. Firstly, a phase-resolving-model requires a finer grid to resolve the short waves compared to a phase-averaged model (which only resolves the wave energy). Secondly, there is no time evolution equation for the non-hydrostatic pressure (incompressible flow assumption). This means that the non-hydrostatic pressure cannot be determined directly, but has to be computed by solving a set of equations. The computational effort required to solve this system of equations is related to the number of grid-cells. Thus, the addition of multiple vertical layers will increase the computational time significantly.

When modelling reef environments, the wave propagation from deep water to a shallow reef flat is important. Most of the coral reefs have a very steep fore shore, where most of the important reef-processes happen (e.g. low frequency wave generation (Péquignet et al., 2009)). Thus, the model boundary must be located in deep water to capture these processes within the model domain. This would imply that a multi-layer non-hydrostatic model is required. For example, the depth-averaged formulated non-hydrostatic model XBeach gives accurate results up to a kh of 1 (Smit et al., 2010), whereas the relative depth in front of a reef can be much deeper. However, for most engineering applications the large computational effort, as a result of the multiple layers, is not desired. Therefore, Smit (2014) developed a reduced two layer non-hydrostatic model (XBeach-nh+), where the second (lower) layer is simplified by assuming a constant non-hydrostatic pressure. This approach improves the dispersive behaviour with limited additional computational time. Apart from the extra layer, the numerical discretizations were adjusted to reduce the discretization error.

XBeach-nh+ has been verified for some simplified cases, but it is never shown how this extra layer will improve the results for more complex environments (e.g. wave transformation over a reef). Moreover, the XBeach-nh+ model was still forced with only a depth-averaged formulation instead of a relation for both layers. In theory, XBeach-nh+ was capable in modelling the wave transformation from deep to shallow water, but the applied boundary conditions

did not represent deep water conditions.

A second challenge for modelling coral reefs is the inclusion of the coral resistance in the model. On the reef flat, a significant part of the wave-energy is dissipated by the coral canopy (Huang et al., 2012). The waves break on the reef crest, which makes the coral resistance the dominant dissipation mechanism on the reef flat (Lowe et al., 2005a).

There are different formulations to include vegetation into a non-hydrostatic model (van Rooijen et al., 2016). However, these vegetation parameters are mainly derived for cylinder shaped geometries, which are representative for most vegetation types (e.g. mangroves). Corals are however complex in shape which makes it not trivial to capture the geometry with such an approach, let alone to relate the canopy parameters to a coral colony. Apart from the shape, it is also known that the flow through a canopy can be significant different than the depth-averaged flow (Luhar et al., 2010; Lowe et al., 2005b). The wave dissipation is caused by the work done by the coral resistance on the canopy flow. Still most vegetation formulations are based on the depth-averaged velocity, which will not always give the correct resistance force.

Therefore, a porous in-canopy model could be a better approach to compute the resistance of the corals. The in-canopy model simulates the flow through the canopy, which can be used to determine the resistance of the corals. By using an equation based on porous media, the corals can be characterized by a porosity, which is easier to determine for corals than other geometrical properties. It is hypothesized that by applying the right porosity, hydrodynamics can be computed correctly without the need for any calibration of the resistance parameters. Next to the calibration, such an approach makes it possible to study the hydrodynamic behaviour for different types of corals. For example, it could help in the design of an artificial reef, where the in-canopy model can be used to estimate wave dissipation. Moreover an in-canopy model could be used to describe transport rates of suspended quantities (e.g. sediment or nutrients) since the near-bed velocity is more representative than the depth averaged velocity to determine the bed shear stress.

1.3 Objectives and research questions

Within this thesis the reduced two layer model will be used to model reef environments and a porous in-canopy model is included to model the coral resistance. This gives the following objective,

To show the applicability of a reduced two layer non-hydrostatic model for reef environments with a coral covered reef flat.

This objective is divided into two parts (hydrodynamic and in-canopy model), which can be separately accomplished. These two sub-objectives are formulated as,

- To show the accuracy of XBeach-nh+.

CHAPTER 1. INTRODUCTION

- Implement and validate the porous in-canopy model to simulate the coral resistance.

Before the accuracy of XBeach-nh+ could be verified, the boundary conditions needed to be adjusted for two layers. Therefore, a boundary conditions for two layers was implemented with addition of the wave interactions of the sum components. Subsequently, XBeach-nh+ can be used to model a reef environments where the resistance is modelled with the in-canopy model.

Based on these sub-objective the research questions were formulated. Two research questions related to the first sub-objective were formulated as,

How accurate can a reduced two layer non-hydrostatic model predict the bulk wave statistics for both a plane beach and reef environment?

and secondly,

How does the second reduced layer affects the accuracy compared to an one-layer model?

The third research question is related to the second sub-objective. This research question is formulated as,

What is the effect of a porous in-canopy model on the prediction of the coral resistance?

1.4 Thesis outline and approach

This thesis can be divided into three parts. In Figure 1.2, these parts and the corresponding chapters are visualized. Chapter 3 and 4 are about the hydrodynamics which is related to the first sub-objective. Chapter 5 and 6 describe the in-canopy model which covers the second sub-objective. The last part combines both objectives in a simulation of a field case (chapter 7).

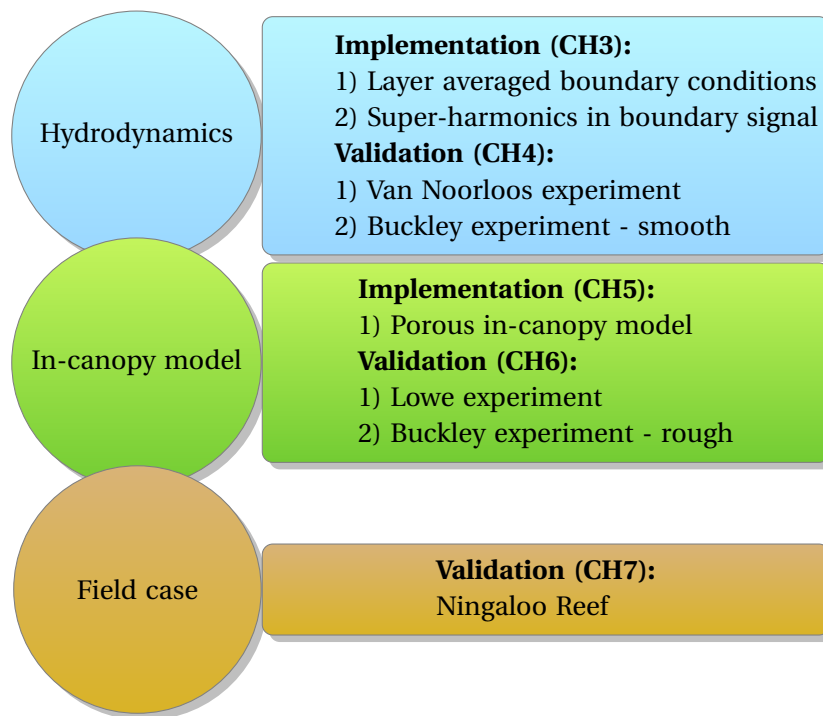


Figure 1.2: Overview of thesis content.

Background information is given in chapter 2 followed by a description of XBeach-nh+ in chapter 3. The formulation, implemented boundary condition and the dispersive behaviour are given in this chapter, which lead to the applicability of XBeach-nh+. The hydrodynamic validation is given in chapter 4 for both bichromatic waves over a plane beach and random waves over a fringing reef. The in-canopy model derived for this thesis is described in chapter 5. Subsequently the validation of the in-canopy model is given in chapter 6. For this validation, both the in-canopy velocity and the effects on the hydrodynamics were validated. Experiments of flow through a canopy were used as validation for the in-canopy velocity. The effects of the hydrodynamics were verified by a lab-test of a fringing reef with roughness elements. The last chapter shows the applicability of XBeach-nh+ to model the hydrodynamics at a case study of Ningaloo Reef (Australia). Both a large bottom gradient and a coral covered reef flat are present at this location, which makes this location a good final validation test. The implemented boundary conditions, formulation of XBeach-nh+ and in-canopy model are discussed in chapter 8. At last answers to the research questions are given in chapter 9 including some recommendations for future research.

Furthermore, the appendices show additional results and calibration results for the Buckley, Noorloos and Ningaloo Reef simulations (appendix A, B and D). The effects of an adjusted bed level when using the in-canopy model is show in appendix C. The used skill scores are described in appendix F. At last, appendix G gives an description of the non-hydrostatic model XBeach.

2

Background

An overview of the given literature about reef-hydrodynamics and canopy-flow is given within this chapter. Section 2.1 and 2.2 describes the reef definitions and reef hydrodynamics. The effects of vegetation on the hydrodynamics is described in section 2.3. Section 2.4 describes the theory of in-canopy flow..

2.1 The definition of coral reefs

Darwin (1836) was the first who studied the formation of an atoll reef. During his voyage on the Beagle he suggested that there may be three stages in the formation of atoll islands. Today, these three stages are still used to classify the different reefs. The theory starts with an extinct volcanic island. When the ocean floor subsides, a fringing reef develops around the island. The coral reef is directly located on the coastline or is separated by a small lagoon. When subsidence continues, the lagoon becomes wider and deeper which is commonly referred to as a barrier reef. Finally, the island sinks below sea level and the reef becomes an atoll. Within the atoll island an open lagoon arises. These developments also hold for a reef along a continental shelf (e.g. Ningaloo Reef and Great Barrier Reef) except that the formation stops after the barrier reef.

Most coral reefs are distinguished from normal sandy beaches due to their very large bottom slope in front of the reef (fore reef). The fore reef stops at the reef crest, which is the highest point of the reef and the location where most of the waves break. After this point the bathymetry continuous almost horizontally towards the coast (the reef flat). Due to the large wave impact on the wave crest, mostly coralline algae and sea grasses grow at the reef crest

and corals grow at the less energetic reef flat (Cassata and Collins, 2008). In Figure 2.1 the different definitions are shown for a reef environment.

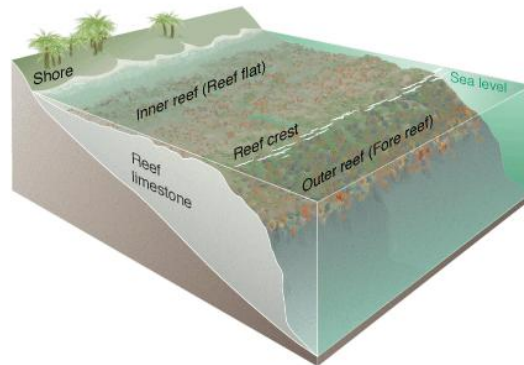


Figure 2.1: A visualisation of the coral reef definitions used throughout this this. Source: Field (2002).

2.2 Reef hydrodynamics

The hydrodynamics at a reef are different to that of a sandy beach due to the large bottom slope in front of a reef. Therefore, most of the waves break at the reef crest offshore of the beach. On the more sheltered reef flat the low frequency waves (LF-waves) are dominant. The steep bottom gradient results in a narrow breaking zone, which gives a large radiation stress gradient at the breaking point. This radiation stress gradient acts as a horizontal force on the water column, which is compensated by a gradient in the water level. This means that the water level (setup) over the reef is higher than mean sea level. Moreover, this narrow breaking zone will vary with respect to the wave groups as breaking is depended on the ratio between the wave height and the water depth. A breaking wave causes a loss of momentum, which is compensated by a water level gradient (similar to the described wave-setup). When the location of the breakpoint is oscillating, due to the wave groups, LF-waves are generated (Péquignet et al., 2009). The generated LF-waves at the reef crest are both onshore and offshore directed. As most of these LF waves do not break, they will be the dominant waves at the reef flat (Figure 2.2). This is a completely different mechanism than for a plane beach where bound long waves are the dominant LF waves (Longuet-Higgins and Stewart, 1962).

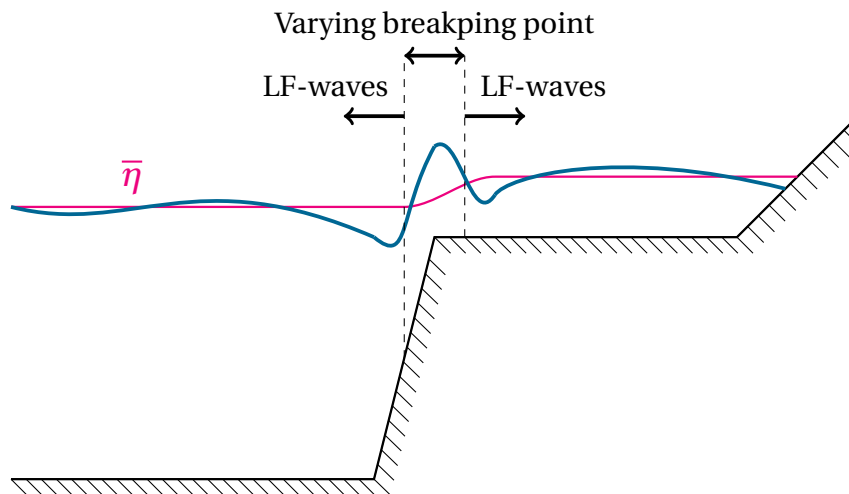


Figure 2.2: Schematization of the reef hydrodynamics. The generation of low frequency waves (LF waves) and setup ($\bar{\eta}$) is shown for a reef environment.

Apart from wave breaking, a part of the wave energy is dissipated by the roughness of the bed. Especially reef flats, which can be completely covered with corals, can significantly increase the roughness (Lowe et al., 2005a). By measuring the energy fluxes over a reef to estimate the dissipation rates, Huang et al. (2012) found that the dissipation at the fore reef is an order of magnitude larger than at the reef flat (Figure 2.3). This implies that wave breaking dissipates most of the wave energy. However, when the water depth is relatively shallow compared to the coral height, bottom friction becomes more important. Especially during low tide, bottom friction can dissipate up to 30% of the total dissipation (Figure 2.3).

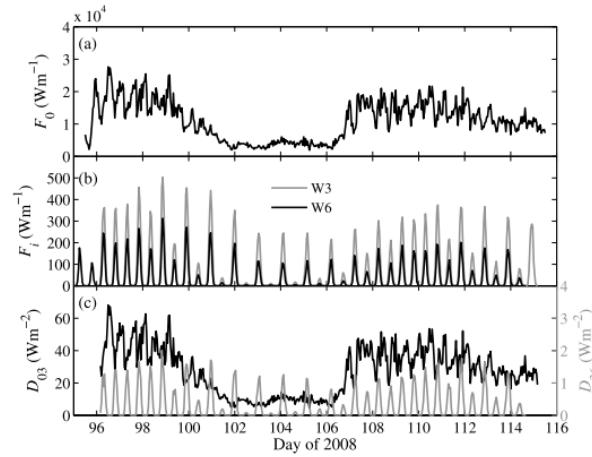


Figure 2.3: The dissipation at the Lady Elliot Islands from the study by Huang et al. (2012). The upper panel (a) shows the energy flux on the ocean (location W_0). The second panel (b) shows the energy flux inside the lagoon for two locations (W_3 and W_6). W_3 is located at the fore reef and W_6 is located in the lagoon. The third panel (c) shows the energy dissipation between location W_0 and W_3 (Fore reef D_{03}) and the dissipation between location W_3 and W_6 (lagoon D_{36}). Source: Huang et al. (2012).

2.3 Effect vegetation on hydrodynamics

This thesis is about the effect of corals on the hydrodynamics. However, in this section the effects of vegetation on the hydrodynamics are explained. The key difference between corals and vegetation is the 3-dimensional structure of corals and that the corals are static instead of swaying with the flow (e.g. seaweed). This means that the described relations in this section also holds for corals.

When waves propagate through a vegetation, the energy of the waves is reduced. For linear waves (without wave interactions) the energy balance for a given frequency component is given by,

$$\frac{\partial P}{\partial x} = -\epsilon_b - \epsilon_f - \epsilon_{veg} \quad (2.1)$$

Where P is the energy flux ($P = c_g E$), ϵ_b the dissipation by wave breaking and ϵ_f the wave dissipation by the bottom friction and ϵ_{veg} the dissipation by the vegetation. The dissipation of the vegetation is a result of the work done by the vegetation on the water column (Mendez and Losada, 2004). The depth-averaged and time integrated work done by the vegetation is described by,

$$\epsilon_{veg} = \overline{\int_{-h}^{-h+h_c} \vec{F} \vec{u} dz} \quad (2.2)$$

Where ϵ_{veg} is the dissipation by the vegetation and \vec{F} the force acting on the vegetation and

CHAPTER 2. BACKGROUND

\vec{u} the velocity vector. This force can be simplified by neglecting the vertical terms (shallow water) which leads to,

$$\epsilon_{veg} = \int_{-h}^{-h+h_c} F_x u dz \quad (2.3)$$

Where F_x is the horizontal force acting on the vegetation. This force is depended on both the geometry of the vegetation and the fluid motion. When neglecting plant swaying, which is valid for corals, a Morison-type equation describes this force. This force is a combination of both the drag and the inertia force and for cylinders it is given as (Morison et al., 1950),

$$F_x(t) = \pi/4 \rho C_M D^2 \frac{du(t)}{dt} + 1/2 \rho C_d u(t)|u(t)| \quad (2.4)$$

Where C_M is the inertia coefficient, C_d the drag coefficient and D the diameter of the cylinder. Note that the velocity u is the velocity through the canopy, which can be different than the undisturbed orbital velocity of the waves. The drag force is a result of the contraction and acceleration of the fluid particles. Due to contraction in front of the cylinder and the acceleration behind the cylinder, there is a pressure difference over the cylinder which is described by the drag force. The inertia force is the result of the acceleration of the flow field around the object.

Besides wave damping, the setup is also influenced by the vegetation (Dean and Bender, 2006). Van Rooijen et al. (2016) described the different mechanisms which affect the mean water level. These mechanisms were described for vegetation, but can also be applied for corals. The mean water level (or setup) can be derived by a wave-averaged momentum equation,

$$\rho g h \frac{\partial \bar{\eta}}{\partial x} + \frac{\partial S_{xx}}{\partial x} + \bar{\tau}_b + \bar{F}_{veg} = 0 \quad (2.5)$$

where the bar denotes the time averaged quantity. This equation shows that the gradient in radiation stress is related to the setup. Within the surf-zone the radiation stress decreases significantly due to wave breaking. These radiation stresses represent an onshore directed wave-force on the water column. This wave-force is balanced by a water level gradient. Thus, a reduction of the wave energy (caused by the vegetation) will decrease the radiation stress gradient in the surf-zone. This lower radiation stress gradient, caused by the vegetation, will reduce the setup.

Secondly, the mean vegetation force will also influence the setup. Due to undertow the mean near bed velocity is offshore directed (linear waves), which implies that the mean vegetation force is onshore directed. To balance this force a setup is required, which increases the setup when vegetation is present. The same principle holds for emergent vegetation and non-linear waves, but under these conditions the vegetation will reduce the setup. The mean depth-averaged velocity for skewed waves is onshore directed, which will result in an offshore directed vegetation force (set-down). Due to the different water depth between the crest and the trough, the vegetation force for emergent vegetation is not constant during

a wave period. This will also result in a mean offshore directed vegetation force (set-down). Thus, the effect of vegetation on the setup is not straightforward and depended on different processes.

2.4 In-canopy flow

The flow through a canopy can be significantly different from the free stream velocity. This in-canopy flow is studied for both air flow through urban roughness (Coceal and Belcher, 2004) and water flow through vegetation (Finnigan, 2000; Ghisalberti, 2002; Lowe et al., 2005b). In most of these studies a simple canopy geometry is used to parametrize the processes. Britter and Hanna (2003) introduce the lambda parameters to describe the canopy for urban areas,

$$\lambda_f = \frac{A_f}{A_T} \quad (2.6)$$

$$\lambda_p = \frac{A_p}{A_T} \quad (2.7)$$

With λ_f as the dimensional frontal area, λ_p the dimensional plan area, A_f the frontal area, A_p plan area and A_T the underlying surface area (area per element). These parameters are derived for urban structures, but are also applied for flow through vegetated canopies. The λ_f is mainly related to the drag force because the surface of the canopy is facing the flow, whereas λ_p is mainly related to the inertia of the flow. For vegetation, these lambda parameters are mostly expressed in term of plant diameter and height.

Nepf and Vivoni (2000) showed that unidirectional flow within a canopy can be divided into three categories according to the ratio of canopy height to the water depth: the unconfined canopy, the submerged canopy and the emergent canopy (Figure 2.4). In the unconfined case, the flow within the canopy is mainly driven by the turbulent shear stress, whereas the pressure is the dominant force within the emergent canopy. In the submerged case, both terms are equally important and none of the terms can be neglected.

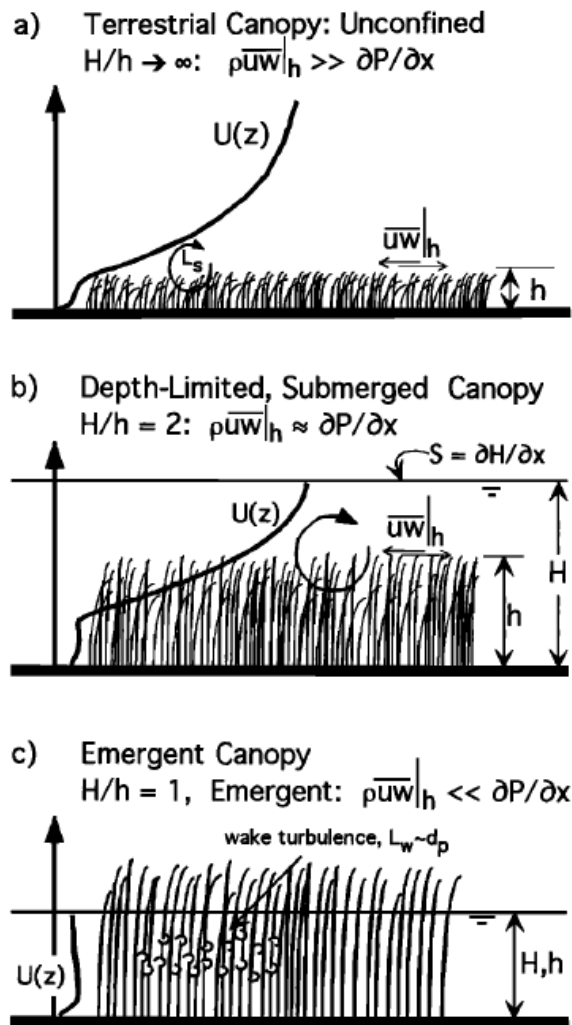


Figure 2.4: Velocity profiles for three depth ratio (canopy height over water depth) derived from (Nepf and Vivoni, 2000). Panel a) show the unconfined case where shear stress control the flow in the canopy. In panel b) the submerged case is shown where both the pressure and shear stress are important. The last panel c) shows the emergent case where the pressure is the dominant force for the canopy flow.

For oscillating flow the description is much more complex. Instead of the shear stress, the pressure becomes the important forcing of the in-canopy velocity (Figure 2.5). In Lowe et al. (2005a) it is concluded that oscillating flow will always generate higher in-canopy flow when compared to unidirectional flow. To show this behaviour, Lowe et al. (2005a) derived a theo-

retically in-canopy model for the canopy-averaged canopy flow,

$$\frac{\partial \bar{U}_c}{\partial t} = -\frac{1}{\rho} \frac{\partial P}{\partial x} + \frac{|U_\infty| U_\infty}{L_s} - \frac{|\bar{U}_c| \bar{U}_c}{L_d} - \frac{C_M \lambda_p}{(1 - \lambda_p)} \frac{\partial \bar{U}_c}{\partial t} \quad (2.8)$$

Where L_d is the canopy drag length scale and L_s the canopy shear length scale,

$$L_d = \frac{2h_c(1 - \lambda_p)}{C_d \lambda_f} \quad (2.9)$$

$$L_s = \frac{2h_c}{C_f} \quad (2.10)$$

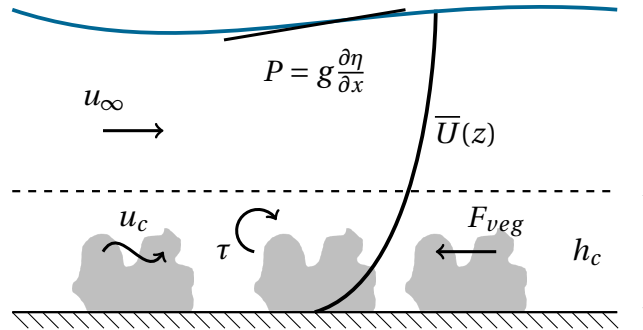


Figure 2.5: Systematization of the canopy flow. The different terms which affect the in-canopy flow are shown (Pressure P , shear stress τ and resistance F_{veg}).

Thus, the in-canopy velocity is determined by a balance between the forcing (pressure and shear stress) and the resistance (drag and inertia). To show the contribution of each term, Lowe et al. (2005a) derived a scaled in-canopy equation. When the equation of the free stream velocity is subtracted from the in-canopy equation and the variables are normalized the relative magnitude of each term can be determined (Lowe et al., 2005a),

$$\frac{\partial(U_c^* - U_\infty^*)}{\partial t^*} = \left(\frac{A_\infty^{rms}}{L_s}\right) |U_\infty^*| U_\infty^* - \left(\frac{A_\infty^{rms}}{L_d}\right) |U_c^*| U_c^* - \frac{C_m \lambda_p}{(1 - \lambda_p)} \frac{\partial U_c^*}{\partial t^*} \quad (2.11)$$

Where $U_c^* = \bar{U}_c / U_\infty^{rms}$, $U_\infty^* = \bar{U}_\infty / U_\infty^{rms}$, $t^* = \omega t$ and $A_\infty^{rms} = U_\infty^{rms} / \omega$.

The degree to which the in-canopy flow is enhanced is mainly depended on three parameters: the drag length scale (L_d), the shear length scale (L_s) and the orbital excursion length (A_∞^{rms}). According to these parameters the flow can be divided into three regimes: canopy independent, inertia dominated and the unidirectional limit. The ratio between the in-canopy

CHAPTER 2. BACKGROUND

velocity and the free stream velocity (attenuation parameter) is used to distinguish between these regimes,

$$\alpha = \frac{\overline{U}_c^{rms}}{U_\infty^{rms}} \quad (2.12)$$

When both the canopy density ($\lambda_p \ll 1$) and the orbital excursion length ($A_\infty^{rms} \ll 1$) are relative small, the right hand side can of equation 2.11 can be neglected. This means that the in-canopy flow is completely given by potential flow (canopy independent regime) and that the attenuation parameter (α) is one.

For the case where the excursion length is much smaller than both the drag length scale and the shear length scale, but the inertia term is not negligible, the canopy flow is inertia dominant. In this case α is given by,

$$\alpha = \frac{1 - \lambda_p}{1 + (C_M - 1)\lambda_p} \quad (2.13)$$

Thus, the attenuation parameter is a function of the density of canopy. In the limit of relative sparse canopies, α goes to one and the in-canopy flow is not affected by the canopy elements. On the other hand a larger density will result in an enhanced canopy flow.

The last regime represent unidirectional flow, where all the acceleration terms can be neglected ($T = \infty$). Then, the in-canopy velocity is determined by a force balance between the shear stress and the drag force. Under these conditions the α is given as,

$$\alpha = \sqrt{\frac{L_d}{L_s}} \quad (2.14)$$

These regimes are plotted in Figure 2.6 as a function of the excursion length. This Figures show the too limits of the attenuation parameter. For inertia dominated regime the α reaches a maximum and for the unidirectional limit the attenuation parameter reaches a minimum. Thus, this figure shows that oscillating flow always enhances the in-canopy velocity compared to unidirectional flow. Mostly, the canopy flow for oscillating flow is not described with one particular regime, but determine by a balance of all terms (general flow). There is no analytical solution for this regime and the in-canopy equation has to be solved numerical.

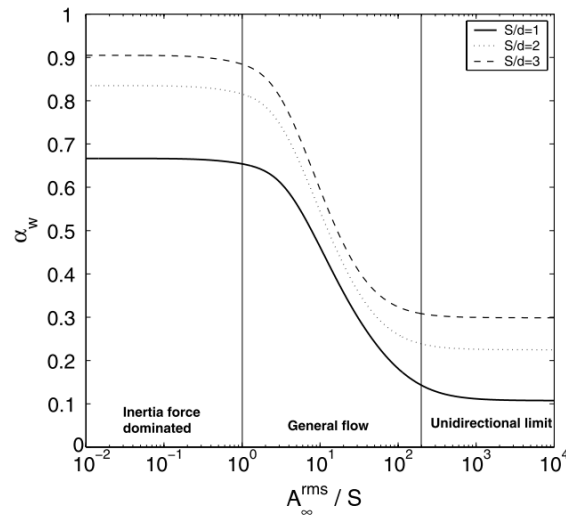


Figure 2.6: Canopy attenuation parameter for different conditions. On the x-axis the excursion length divided by the canopy element distance (S). the Y-axis represent the attenuation parameter. The three lines represent the regimes of three tested geometries. Source: Lowe et al. (2005a)

Next to equation 2.8, Lowe et al. (2008) derived a porous in-canopy model to compute the in-canopy flow for a porous media (e.g. coral species). The turbulent porous media theory of Gu and Wang (1991) was used to describe the porous in-canopy flow. This in-canopy model is used in this thesis and it is shown in Chapter 5. The key differences between equation 2.8 and porous in-canopy model is the addition of a laminar resistance term, a different drag term and neglecting the shear stress term in the porous model (which is added for completeness).

3

XBeach-nh+

Within this chapter the formulation of XBeach-nh+ is given (section 3.2). The improved dispersive behavior is shown in section 3.3. Subsequently, the implemented layer-averaged boundary condition is described in section 3.4 and the inclusion of the wave interactions at the boundary is described in section 3.5. Section 3.6 and 3.7 show the effects of respectively the layer-averaged boundary condition and the second order wave interactions. Finally, the applicability of XBeach-nh+ is given in section 3.8.

3.1 Introduction

A depth-averaged non-hydrostatic model is not applicable when deep water waves are modelled, because the behaviour of deep water waves is different than for shallow water waves. The wave celerity for deep water waves depends on the wave-length instead of the water depth for shallow water waves. This dependence on the wave length, called frequency dispersion, can be captured to a certain extend with a depth-averaged formulation (Zijlema et al., 2011). To improve the dispersive behaviour of a non-hydrostatic model additional vertical layers must be included. However, this will increase the computational time significantly, because the computation of the non-hydrostatic pressure is a time consuming process. Therefore, a reduced two layer model was derived (Cui et al., 2014), which improves the dispersive behaviour for less extra computational cost. Smit (2014) implemented this formulation within XBeach (called XBeach-nh+).

Due to the reduced two layer approach the number of pressure unknowns is reduced by half compared to a full two layer model. This has a large effect on the computational time, where a simpler system of equation has to be solved. The optimal computational effort for such a system of equations is given as $n \log n$, where n is the dimension of the solved matrix (Saad, 2003). Thus, this assumption will reduce the computational time by at least a half, but even more for a large number of grid cells (2-dimensional simulations).

As a consequence of a better dispersive behaviour, the boundary of the domain can be located in deeper water and secondly the higher wave components are better resolved. Due to the large bottom gradient at the fore reef, a boundary in deep water is necessary when modelling coral reefs.

However, the boundary condition for XBeach-nh+ was still based on a depth averaged formulation. In this thesis a boundary condition including second order wave interaction is given for two computational layers. Without the proper boundary conditions, the model results can be wrongly computed. The following two issues can arise due to the boundary condition (Madsen and Sørensen, 1993):

- Mismatch between the vertical velocity profile of the waves and the imposed boundary condition. This will result in a standing wave (evanescence modes) at the boundary.
- Boundary condition based on first order wave theory will generate spurious wave at the frequencies of the bound harmonics. These spurious waves are not bound to the primary waves and can propagate freely though the domain.

Therefore, a layer averaged boundary condition was formulated to reduce the mismatch between the boundary and the model domain (reduction of the evanescence modes). Second order wave interactions were included to diminish the spurious waves. The sub-harmonics were already included in the boundary conditions, but the formulation was adjusted within this thesis. Both the interaction coefficient and phase description were adjusted, which will lead to better results in 2D and in deeper water. Furthermore, the super-harmonics were added to the boundary signal.

3.2 Formulation

The formulation of XBeach-nh+ is almost the same as the formulation of XBeach-nh with the addition of the equations for the reduced layer. However, the computational of XBeach-nh+ was implemented as a completely new subroutine. When the keyword *qh3d* is set the reduced two layer model is used for the computation. Besides of the two layers, the numerical scheme's are also slightly different in XBeach-nh+.

Within this section the derivation of the governing equation is shown. The Euler equations are used as starting point, where the horizontal momentum equation is given as,

$$\frac{\partial u}{\partial t} + \frac{\partial uu}{\partial x} + \frac{\partial wu}{\partial z} = -\frac{1}{\rho} \frac{\partial (p + p_{nh})}{\partial x} + \frac{\partial \tau}{\partial z} \quad (3.1)$$

the vertical momentum equation is given as,

$$\frac{\partial w}{\partial t} + \frac{\partial uw}{\partial x} + \frac{\partial ww}{\partial z} = -\frac{1}{\rho} \frac{\partial(p_{nh})}{\partial z} \quad (3.2)$$

Continuity of mass requires the following equation,

$$\frac{\partial u}{\partial x} + \frac{\partial w}{\partial z} = 0 \quad (3.3)$$

To determine the free surface, the global continuity equation is necessary which is given as,

$$\frac{\partial \xi}{\partial t} + \frac{\partial}{\partial x} \int_{-d}^{\xi} u dz = 0 \quad (3.4)$$

Where $p = \rho g(\xi - z)$ is the hydrostatic pressure and p_{nh} the non-hydrostatic pressure. These equations are bound by a constant pressure at the free surface and the kinematic boundary conditions,

$$w = \frac{\partial \xi}{\partial t} + u \frac{\partial \xi}{\partial x} \quad (z = \xi) \quad (3.5)$$

$$w = -u \frac{\partial d}{\partial x} \quad (z = -d) \quad (3.6)$$

To obtain the equations for a two-layer model, the water depth is divided into two layers, where the layer heights are given as $\Delta z_1 = \alpha h$ and $\Delta z_2 = (1 - \alpha)h$. The α represents the layer distribution within the domain. This gives the following definitions for the layer interfaces: $z = [-d(x), -d(x) + \alpha h, \xi]$. In Figure 3.1 this formulation is shown with the location of the variables. According to this formulation the layer averaged horizontal velocities are given by

$$u_j(x, t) = \frac{1}{\Delta z_j} \int_{z_{j-1}}^{z_j} u dz \quad (3.7)$$

Furthermore, the normalized non-hydrostatic pressure, q , is given as p_{nh}/ρ . Then, by integrating over the layer the following horizontal momentum equation is derived (assuming $\int_{z_{j-1}}^{z_j} u^2 \approx \Delta z_j u_j^2$),

$$\frac{\partial \Delta z_j u_j}{\partial t} + g \Delta z_j \frac{\partial \xi}{\partial x} + \frac{\partial \Delta z_j u_j u_j}{\partial x} + \bar{u}_j \omega_j - \bar{u}_{j-1} \omega_{j-1} + \frac{\partial}{\partial x} \left(\Delta z_j \frac{q_j + q_{j-1}}{2} \right) - q_j \frac{\partial z_j}{\partial x} + q_{j-1} \frac{\partial z_{j-1}}{\partial x} - \tau_j + \tau_{j-1} \quad (3.8)$$

where \bar{u}_j is the velocity at the layer faces and $\omega_j = \bar{\omega}_j - \partial_t z_j - \bar{u}_j \partial_x z_j$. The non-hydrostatic pressure (q) and vertical velocity (\bar{w}_j) are located at the layer interfaces. Secondly, the vertical momentum equation integrated over a layer is given by,

$$\frac{\Delta z_j w_j}{\partial t} + \omega_j \bar{w}_j - \omega_{j-1} \bar{w}_{j-1} + \frac{\partial(\Delta z_j u_j w_j)}{\partial x} + q_j - q_{j-1} = 0 \quad (3.9)$$

Lastly, the integrated continuity equation holds,

$$\frac{\partial}{\partial x} (\Delta z_j u_j) + \bar{w}_j - \bar{w}_{j-1} - \bar{u}_j \frac{\partial z_j}{\partial x} + \bar{u}_{j-1} \frac{\partial z_{j-1}}{\partial x} = 0 \quad (3.10)$$

There is no time evolving equation for the non-hydrostatic pressure, which means that a system of equations has to be solved to determine the non-hydrostatic pressure (Poisson equation). To solve this system of equations, in particular for 2DV simulations, is a computational expensive task. Therefore, the system will be simplified which require to transform the two layers into a depth averaged velocity (U) and velocity difference (Δu) according to,

$$\begin{bmatrix} u_1 \\ u_2 \end{bmatrix} = \begin{bmatrix} 1 & 1-\alpha \\ 1 & -\alpha \end{bmatrix} \begin{bmatrix} U \\ \Delta u \end{bmatrix}; \quad \begin{bmatrix} U \\ \Delta u \end{bmatrix} = \begin{bmatrix} 1 & 1-\alpha \\ 1 & -1 \end{bmatrix} \begin{bmatrix} u_1 \\ u_2 \end{bmatrix} \quad (3.11)$$

This is a different definition than presented in Cui et al. (2014), where the difference in momentum was used. The difference in velocity was preferred for this application, because it goes to zero for the hydrostatic limit. Secondly, the non-hydrostatic pressure at the bottom is given as the non-hydrostatic pressure between the layers q_1 plus a Δq . For relative shallow water, it can be assumed that Δq is zero ($\Delta q/q \ll 1$). In this way all the term with $q + \Delta q$ can be approximated as q . This also means that \bar{w}_1 can be neglected. It is also assumed that Δu is much smaller than U , which made it possible to neglect the term with Δu^2 . Then, the evolution equation for U can be obtained by summation of equation 3.8 for $\Delta z_1 u_1$ and $\Delta z_2 u_2$,

$$\frac{\partial(hU)}{\partial t} + gh \frac{\partial \xi}{\partial x} + \frac{\partial}{\partial x} (hU^2) + \frac{\partial}{\partial x} \left(\frac{1+\alpha}{2} hq + \frac{1}{2} \alpha \Delta q \right) - (q + \Delta q) \frac{\partial d}{\partial x} = \tau_0 \quad (3.12)$$

Similar by subtracting equation 3.8 for $\Delta z_1 u_1$ divided by α from equation 3.8 for $\Delta z_2 u_2$ divided by $(1-\alpha)$, the evolution equation for Δu can be derived,

$$\frac{\partial h \Delta u}{\partial t} + \frac{\partial h \Delta u U}{\partial x} + \frac{\omega_1 \bar{u}_1}{\alpha(1-\alpha)} + \frac{\partial}{\partial x} \left(\frac{hq}{2} \right) + \frac{hq}{2-2\alpha} \frac{\partial \alpha}{\partial x} - \frac{q}{1-\alpha} \frac{\partial \xi}{\partial x} = -\frac{\tau_0}{\alpha} + \frac{\tau_1}{\alpha(1-\alpha)} \quad (3.13)$$

Where τ_1 can be described as $2\nu \Delta u/h$. The vertical momentum equation for w_2 is derived when the relations for U , Δu , q and Δq were substituted into equation 3.9,

$$\frac{\partial h w_2}{\partial t} - \frac{\omega_1 \bar{w}_1}{\alpha} + \frac{\partial}{\partial x} (hU w_2 + \alpha 2h \Delta u w_1) - \frac{q}{(1-\alpha)} = 0 \quad (3.14)$$

At least the continuity equation can be expressed in term of these variables. To derive the continuity equation for the upper layer addition of, twice equation 3.10 for $j = 1$ to equation 3.10 for $j = 2$ and using the following relation $w_1 = (\bar{w}_0 + \bar{w}_1)/2$ gives,

$$\frac{\partial}{\partial x} [(1+\alpha)hU + (1-\alpha)h\alpha\Delta u] + 2w_2 - \bar{u}_2 \frac{\partial \xi}{\partial x} - \bar{u}_1 \frac{\partial z_1}{\partial x} = 0 \quad (3.15)$$

These equations can be used to solve U , ξ , w_2 and Δu and are independent of w_1 and Δq . It is even possible to compute \bar{w}_1 when a second continuity equation is used. To derive the second continuity equation for the lower layer, equation 3.10 is added to two times the kinematic bottom condition,

$$\frac{\partial}{\partial x} [hU + (1 - \alpha)h\Delta u] + \frac{2w_1}{\alpha} - \frac{\bar{u}_1}{\alpha} \frac{\partial z_1}{\partial x} + \frac{\bar{u}_0}{\alpha} \frac{\partial d}{\partial x} = 0 \quad (3.16)$$

These formulations are used to compute the additional variables used in XBeach-nh+.

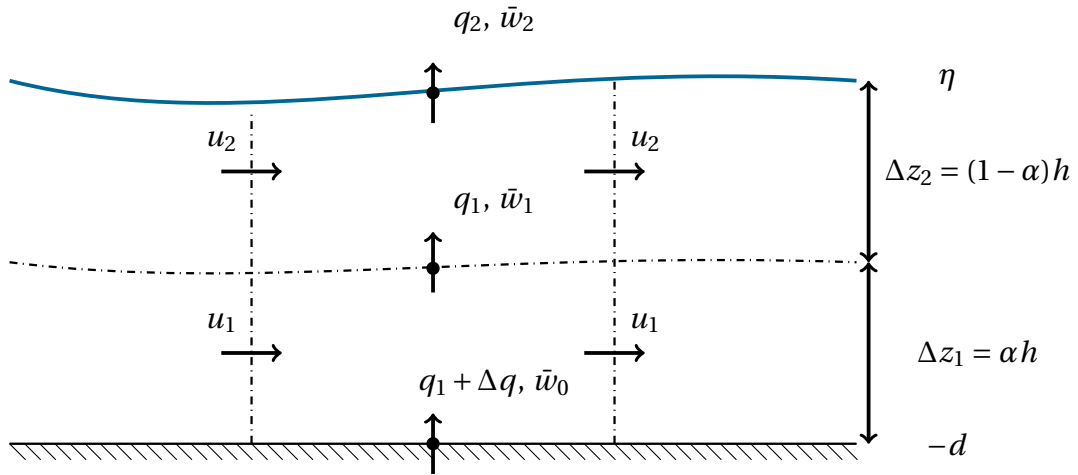


Figure 3.1: Grid representation in XBeach-nh+.

3.3 Dispersive behavior

To verify the dispersive behaviour, linear waves in a standing basin were modelled. For linear waves the model results can be compared to the analytical solution of linear wave theory. Multiple runs of a linear standing wave were used to show the accuracy of the dispersion relation. By varying the basin length (L), the dispersion relation can be verified for different values of kh . A cosine was set as initial condition in the closed basin with a length of

$$L_{basin} = 1/2L \quad (3.17)$$

Where L is the wave length. The following initial condition was applied,

$$\eta = a \cos(kx) \quad (3.18)$$

Where η is the surface elevation, a the amplitude and k the wave number ($k = 2\pi/L$). For every simulation the wave period was determined by computing the zero up-crossing period. From this period and the known wavelength the celerity was determined.

A amplitude (a) of 0.001 m and a water depth of 2 meter were used. These parameters result in an amplitude-wavelength ratio smaller than 0.0001 and an amplitude water depth ratio smaller than 0.0001. Within these limits linear wave theory is valid. The computational grid is discretized with 100 point and a grid size of 0.1 m.

The exact solution for the wave celerity derived by linear wave theory is given as,

$$c = \sqrt{g/k \tanh kh} \quad (3.19)$$

By neglecting the non-linear terms and linearising the equation of the reduced two layer model, the dispersion relation for this system can be derived as (Cui et al., 2014),

$$c = \sqrt{gh \frac{4 + (\alpha - 2\alpha^2 + \alpha^3)(kh)^2}{4 + (1 + 2\alpha - 3\alpha^2)(kh)^2}} \quad (3.20)$$

In a similar way the dispersion relation for a depth averaged model can be derived (Cui et al., 2014),

$$c = \sqrt{gh \frac{1}{1 + 1/4(kh)^2}} \quad (3.21)$$

According to linear wave theory the group velocity is given by,

$$c_g = \frac{\partial k}{\partial \omega} \quad (3.22)$$

Due to the varying basin length (instead of the water), the group velocity could be computed, because both the wave-number and the radial frequencies changed for every simulation. This made it possible to determine the approximated of the derivative as,

$$c_g = \frac{\Delta k}{\Delta \omega} \quad (3.23)$$

Both nh and nh^+ were used to computed the solution. The results of these simulation is shown in Figure 3.2. The figure shows the accuracy of the group velocity (c_g), wave celerity (c), the radial frequency (ω) and the relative error with linear wave theory.

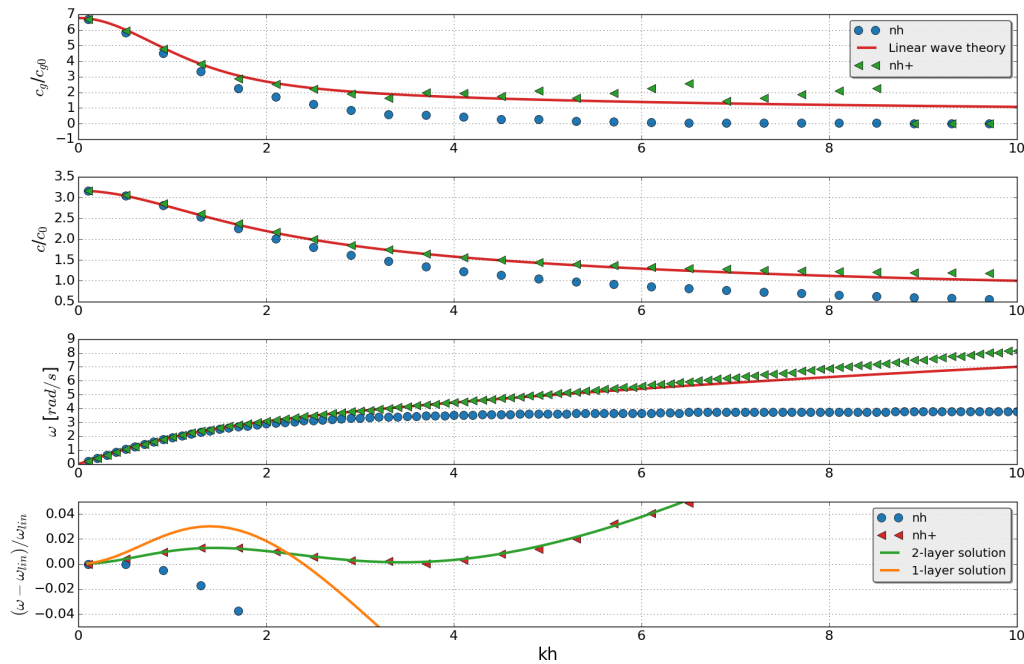


Figure 3.2: The dispersive behaviour for both nh and nh+ compared to linear wave theory. The upper panel shows the results for the normalized group velocity. The second panel shows the results for the wave celerity (normalized by the shallow water wave celerity). The third panel the radial frequency, where the output for all simulation is shown (In the other panel the output is only marker every 4 point for visibility). The last panel shows the relative error of the radial frequency compared to linear wave theory. In the last panel the linearized of the 1 and 2 layer model are shown.

This figure shows a significant improved dispersive behaviour of XBeach-nh+ compared to XBeach-nh. XBeach-nh+ gives an relative error of 2% for a kh of 5, whereas Xbeach-nh gives the same error for a kh of 1. Moreover, the results shows that XBeach-nh gives a slightly worse result than the linearised solution. This could be a result of discretization errors, which are not present in the new formulation of XBeach-nh+.

3.4 Layer averaged boundary condition

In the current XBeach formulation only the depth averaged velocity (U) was imposed at the boundary and the Δu was set to zero. However, in deep water the Δu will become non-zero and should be imposed as well. Thus, besides of a U also a value for the Δu should be forced at the boundary.

The U and Δu can be computed from to the layer averaged velocities according to,

$$U = u_1 + (1 - \alpha)u_2 \quad (3.24)$$

$$\Delta u = u_1 - u_2 \quad (3.25)$$

Where u_1 and u_2 are the layer averaged velocities. These velocities are derived from linear wave theory as,

$$\begin{aligned} u_i &= \frac{\int_{z_1}^{z_2} \omega a \frac{\cosh(k(z+h))}{\sinh(kh)} \cos(\omega t) dz}{z_2 - z_1} = \frac{\omega a}{\sinh(kh)(z_2 - z_1)} \left[\frac{1}{k} \sinh(k(z+h)) \right]_{z=z_1}^{z=z_2} \\ &= \frac{\omega a}{\sinh(kh)(kz_2 - z_1)} (\sinh(k(z_2 + h)) - \sinh(k(z_1 + h))) \end{aligned} \quad (3.26)$$

Where z_1 and z_2 are the the z-locations of respectively the bottom and the top of the layer. When using the depth-averaged mode (XBeach-nh) the depth averaged velocity at the boundary is based on a continuity relation,

$$U = \frac{\omega}{kh} \eta \quad (3.27)$$

In Figure 3.3 the velocities of both approaches (depth and layer-averaged) are shown for a single harmonic in deep water ($kh = 2.5$). A shallow water wave (grey dashed line) is added as reference. For the deep water wave there is a clear difference between the two layer-averaged velocities. Furthermore, the depth averaged velocity (U) is almost the same for both the layer and depth-averaged approach (Note that there is slight difference between the mean and the mean of two mean values). Thus, the choice between XBeach-nh+ or XBeach-nh will not result in a significant different signal of the depth averaged velocity.

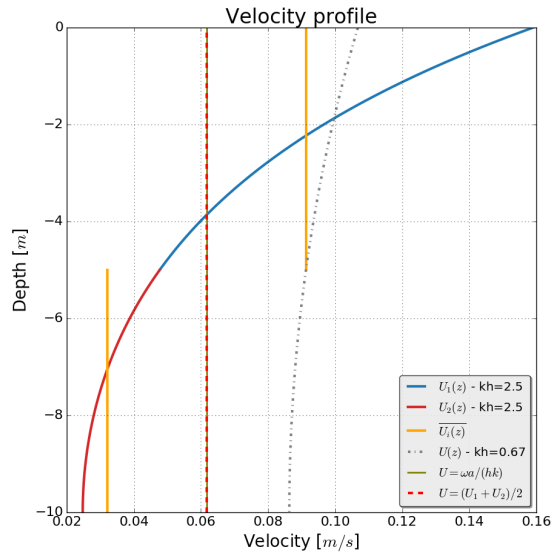


Figure 3.3: Velocity profile according to linear wave theory based on a single harmonic ($a = 0.1\text{ m}$, $h = 10\text{ m}$ and $f = 0.25\text{ Hz}$). The layer averaged velocities are shown as yellow vertical lines. Furthermore, the depth averaged velocity (blue) and the mean of both layer averaged velocities (red dashed) are shown. The grey line represent a shallow water wave ($f = 0.1\text{ Hz}$).

3.5 Second order wave interaction in the boundary condition

When the model is forced with random waves from a wave-spectrum, the different wave components will interact and force bound waves. A boundary without these bound waves will generate spurious free waves at the frequency of the bound waves with an equal amplitude and opposing phase (Madsen and Sørensen, 1993). This is not desired for two reasons. Firstly, these spurious waves will freely propagate through the domain and can locally influence the wave height. Secondly, these waves will interact with other waves and generate other wave components which does not represent reality.

A boundary conditions including the sub-harmonics was already included in XBeach described in Van Dongeren (2003). Within this thesis the super-harmonics were added, the formulation was formulated for two layers, the formulation of the phase was adjusted and the computation of the interaction coefficient was slightly adapted.

A pair of two primary waves will force a second order bound waves with a sum frequency and difference frequency. The bound waves with a difference frequency are called sub-harmonics and these waves have a radial frequency of $\omega_3 = \omega_1 - \omega_2$. The bound waves with a sum frequency are called super-harmonics and have a radial frequency of $\omega_3 = \omega_1 + \omega_2$. The second order waves are bound to two pair of primary waves, which means that these waves will not follow the dispersion relation. The wave number is given by a vectorial sum

or difference of both primary wave numbers,

$$k_3 = |\vec{k}_1 \pm \vec{k}_2| = \sqrt{k_1^2 + k_2^2 \pm 2k_1 k_2 \cos(\Delta\theta)} \quad (3.28)$$

Where $\Delta\theta$ is the difference in direction between the two primary waves ($\Delta\theta = \theta_1 - \theta_2$). For the super-harmonics the wave numbers should be summed and the sub-harmonics wave number is given by the difference of both wave numbers.

Hasselmann (1962) derived a theory, based on a weakly non-linear wave theory, to determine the amplitude of these bound waves. Therefore, this theory is only valid for small amplitude waves ($a/d \ll 1$). As the boundary is mostly located in deeper water, this is a valid assumption. In Okihiro et al. (1992) this theory is used to derive an expression for the second order energy density of a given wave-spectrum. According to this theory the energy of the super-harmonics is given by,

$$E_3(\omega_3) = 2 \int_{\Delta f}^{\infty} \int_0^{2\pi} \int_0^{2\pi} D(\omega_1, \omega_2, \Delta\theta)^2 E_1(\omega_1, \theta_1) E_2(\omega_2, \theta_2) d\theta_2 d\theta_1 df \quad (3.29)$$

and the energy of the sub-harmonics is given by,

$$E_3(\omega_3) = 2 \int_{\Delta f}^{\infty} \int_0^{2\pi} \int_0^{2\pi} D(\omega_1, -\omega_2, \Delta\theta + \pi)^2 E_1(\omega_1, \theta_1) E_2(\omega_2, \theta_2) d\theta_2 d\theta_1 df \quad (3.30)$$

Where E_1 is the energy density of the first primary wave, E_2 the energy density of the second primary wave and E_3 the energy of the generated bound wave. The interaction coefficient, $D(\omega_1, \omega_2, \Delta\theta)$, is given by,

$$D(\omega_1, \omega_2, \Delta\theta) = -\frac{gk_1 k_2 \cos(\Delta\theta)}{2\omega_1 \omega_2} + \frac{(\omega_1 + \omega_2)^2}{2g} + \frac{\left\{ (\omega_1 + \omega_2) \left[\frac{(\omega_1 \omega_2)^2}{g^2} - k_1 k_2 \cos(\Delta\theta) \right] - 0.5 \left(\frac{\omega_1 k_2^2}{\cosh(k_2 d)} + \frac{\omega_2 k_1^2}{\cosh(k_1 d)} \right) \right\}}{g(\omega_1 + \omega_2)} \quad (3.31)$$

$$\frac{1}{[gk_3 \tanh(k_3 d) - (\omega_1 + \omega_2)^2] (\omega_1 + \omega_2)}$$

The phase of the bound wave is given by the sign of the coefficient. Thus, the sub-harmonics are out of phase with the wave group, except for very large directional spreading and the super-harmonics are always in phase with the two primary waves (stokes waves).

The amplitude of the bound wave for every pair of primary waves can be found with,

$$A_3 = \sqrt{2E_3 df \operatorname{sgn}(D)} \quad (3.32)$$

Where df is the resolution of the primary spectrum and $\operatorname{sgn}(D)$ the sign of the interaction coefficient. Note that the df is different than the difference frequency $f_3 = f_2 - f_1$. The direction of the bound wave can be derived from geometry relations and it is given by,

$$\theta_3 = \arctan\left(\frac{k_2 \sin \theta_2 - k_1 \sin \theta_1}{k_2 \cos \theta_2 - k_1 \cos \theta_1}\right) \quad (3.33)$$

Combing all these wave properties the following wave can be constructed,

$$\eta_3(\vec{x}, t) = A_3 \cos(\vec{k}_3 \vec{x} - \omega_3 t + \phi_3) \quad (3.34)$$

For every par of primary waves, the bound wave is included in the boundary signal. This is illustrated in Figure 3.4. When there are n primary components in the spectrum, $n - 1$ sub-harmonics will be generated and $2n - 1$ super-harmonics will be generated.

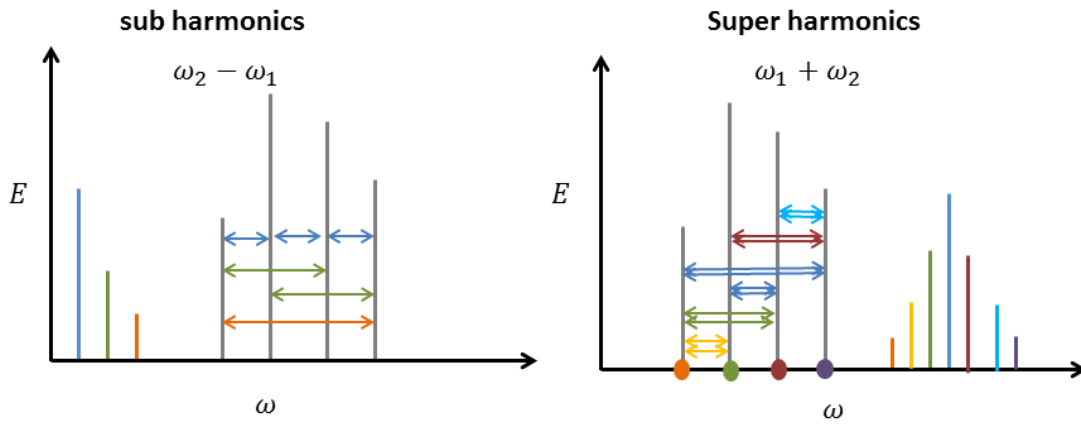


Figure 3.4: Second order wave interaction for a given spectrum. The grey lines represent the primary waves and the coloured lines show the bound waves. The arrows indicate the interaction between two waves. The dots show the self-interaction of the primary waves.

Instead of the surface elevation, the model is forced with the velocity. Therefore, the flux is computed for every component as,

$$\vec{q} = \vec{c}_3 \vec{\eta}_3 = \frac{\omega_3}{k_3} \vec{\eta}_3 \quad (3.35)$$

The depth averaged velocity can be obtained by dividing the flux by the water depth. However, the flux must be divided over two computational layers in XBeach-nh+. The shape of the second order velocity potential is used to divide the velocity over both layers,

$$\Phi = \frac{du}{dx} = A \frac{\cosh(k(z+h))}{\sinh(kh)^4} \quad (3.36)$$

Where A is the amplitude of the velocity potential. Then, the ratio of the flux through a layer and the total flux is derived as,

$$q_1/q = \frac{\sinh k_3(z+h)}{\sinh k_3 h} \quad (3.37)$$

$$q_2/q = 1 - \frac{q_1}{q} = \frac{\sinh k_3(h) - \sinh k_3(z+h)}{\sinh k_3 h} \quad (3.38)$$

Where z is the vertical location of the layer (negative downwards). From this ratio the layer averaged velocities can be computed,

$$u_1 = q_1/q \frac{q}{z} \quad (3.39)$$

$$u_2 = q_2/q \frac{q}{(h+z)} \quad (3.40)$$

Where z is the layer level (negative downwards).

3.6 Effect layer averaged formulation

To show the effect of the boundary condition based on two layers, a simulation of a single harmonic ($f = 0.6$ Hz and $a = 0.01$ m) was modelled for different water depths. When the water depth becomes very small the second order waves becomes more dominant. Therefore, a very small amplitude was used ($a/d < 0.03$) to minimize the second order responds. A large bottom friction ($x > 10m$) was applied to damp all the reflective long waves and a 1/10 sloping profile at the end of the domain was used to dissipate the short waves. At the boundary standing waves (evanescence modes) will arise for deep water conditions. To exclude the evanescence modes in the comparison, the wave height at location $x = 5m$ was compared for all the runs. All simulations were done with XBeach-nh+ for a fair comparison.

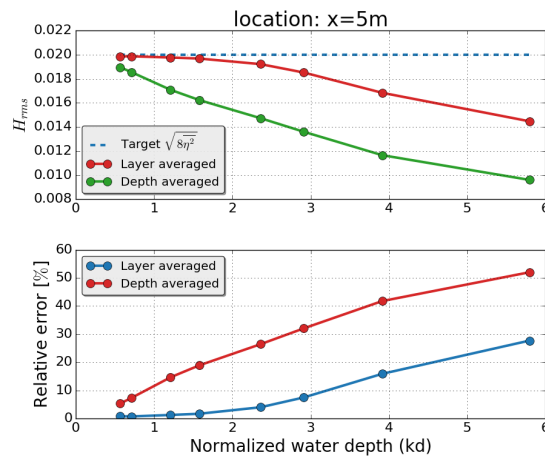


Figure 3.5: The effect of the formulation of the boundary condition for a single harmonic. The upper panel shows the H_{rms} for both formulations at location $x = 10m$. The dashed line represents the target signal (based on linear wave theory) at the boundary. The lower panel shows the relative error with the target signal.

Figure 3.5 shows that in deeper water, the boundary signal deviates from the target signal. For the depth averaged formulation the error is larger than 10% for a relative depth (kh) of 1. When using the layer averaged formulation the same error is made with a relative depth of 3 and an acceptable relative error of 2% is made for a kh less than 2. This deviation is a result of the difference between the behaviour of the reduced two layer system and linear wave theory. For shallow water the two solutions converge. However, when the relative water depth increases, the response is different. Therefore, the amplitude for a given velocity at the boundary deviates from linear wave theory. Note, that these results are specific for XBeach-nh+ and does not hold for XBeach-nh.

For a relative depth of 4 the velocity signals are plotted in Figure 3.6 to show the difference between both boundary conditions. The evenness mode due to mismatch of the boundary signal with the hydrodynamics is visible in the rms signal. It is found that this evenness mode arises by a kd of 1.5 for the depth averaged formulation and it arises by a kh of 3 for the layer averaged formulation. However, these waves are only present near the boundary, which makes it not a large problem.

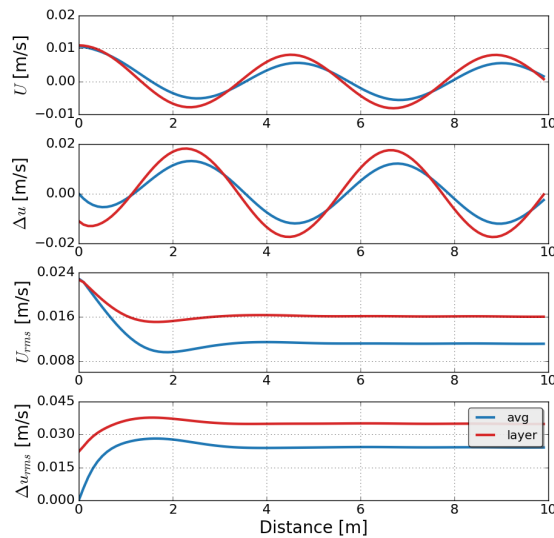


Figure 3.6: The spatial difference between the solution of both boundary signals (avg: depth-averaged formulation and layer: layer-averaged formulation). The upper panel shows the depth averaged velocity U . The second panel shows the Δu . In the last two panels the rms value of both velocities is given.

3.7 Effect second order bound waves

The importance of the second order bound waves is shown in Figure 3.7 for a JONSWAP wave spectrum. The ratio of the bound energy over the initial energy ($H_{rms,bound}/H_{rms,initial}$) was computed for different wave conditions based on the theory described in section 3.5. Both the wave height and the depth were varied, which results in a different steepness ($H/(gT^2)$) and relative depths (kh). The breaking waves ($H_s/d = 0.7$) were removed in the plot although the validity of the interaction coefficient is not valid for more conditions. The left panel shows the effect for the sub-harmonics and the right panel the effect for the super-harmonics.

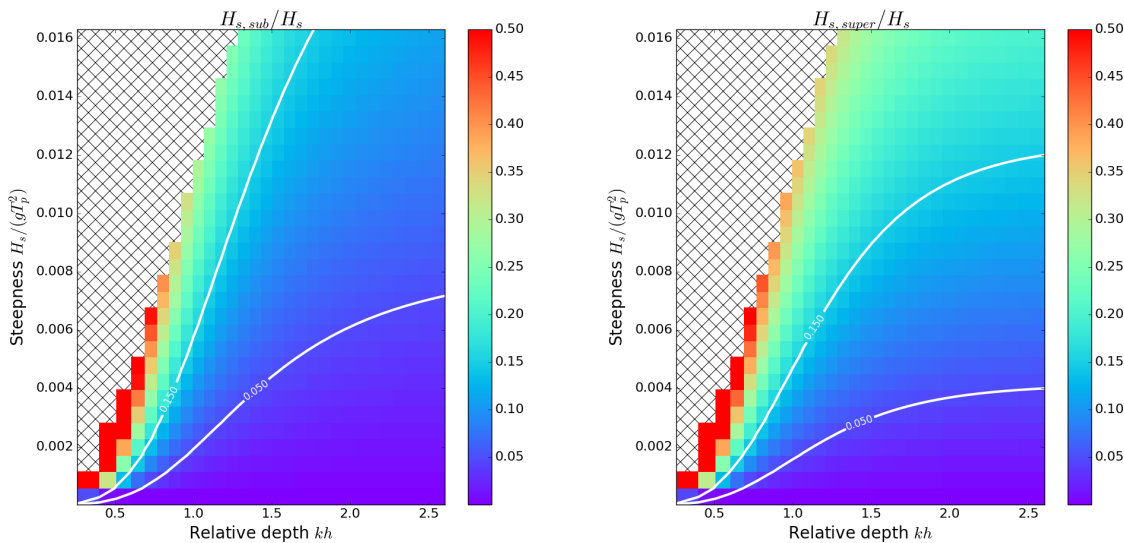


Figure 3.7: The effect of the second order bound waves for different wave conditions. The ratio of the bound wave energy over the initial wave energy is plotted. The left panel shows the sub harmonics and the right panel the super harmonics.

It can be seen that for very shallow water the energy increases significant and becomes more than 50% of the spectrum energy. However, the interaction coefficient is derived with the assumption of weak non linear waves. This implies the boundary condition is only valid for $a/d \ll 1$. Thus, in shallow water this theory is not valid. Therefore, the boundary should not be locate in shallow water. Moreover, it can be seen that there is difference between the sub and super-harmonics. The energy of the super-harmonics is mainly related to the steepness of the waves, whereas the water depth is important for the sub-harmonics. In general the error made when neglecting these waves is small, but for very steep waves or intermediate water depths the inclusion of these waves becomes important.

3.8 Conclusion

Due to the reduced two layer approach, XBeach-nh+ (nh+) can be used in deeper water. The dispersion relation is accurately described for linear waves up to a kh of 5 with nh+, whereas nh gives accurate results up to a kh of 1 (relative error 2%).

XBeach-nh+ will also give a better prediction short waves. The triad interactions are related to the phase mismatch between the bound and free waves (Ohyama T. et al., 1995). Thus, a better prediction of the dispersive behaviour will also have an effect on the energy transfer between the short waves.

Apart from an error in the dispersion relation, there is also a deviation in amplitude when the relative depth increases. The implemented layer-averaged boundary condition gives an accurate result up to kh of 3 (10% relative error). For an increasing kh the solution of the reduced two layer system and linear wave theory diverge. However, the error in the dispersion relation is more restrictive because it affects the hydrodynamics within the domain, whereas the boundary signal could be adjusted for deep water conditions.

XBeach-nh+ gives accurate results for the linear dispersion relation up to a kh of 5 (relative error 2%), but for a kh larger than 2 the free surface amplitude will deviates from linear wave theory (relative error 2%).

Due to the addition of the second order wave interactions at the boundary, the generation of spurious waves will be reduced. When these interactions are not included, the spurious wave energy of the sub-harmonics is $\approx 5\%$ and the wave energy of the super-harmonics is 10% for typical wave conditions ($kh = 1$ and $H_s/gT_p^2 = 0.002$). For more shallow water (sub-harmonics and super harmonics) or steeper waves (super-harmonics), the energy of the spurious waves increases even more. The implemented wave interactions are only valid for small a/d ratios. On the other hand the model cannot resolve the very short waves accurately. Thus, it is not possible to locate boundary in too shallow water ($a/d < 1$) neither in too deep water for the super-harmonics.

4

Validation: hydrodynamics

XBeach-nh+ was validated for two lab-tests. In section 4.2 the energy transfer between the major wave components was verified by a lab-test of biochromatic waves on a plane beach. Subsequently, the bulk wave statistics were validated for a lab-test of a fringing reef in section 4.3. Finally the conclusion are given in section 4.4.

4.1 Introduction

On the reef flat the LF-waves are dominant and therefore it is important to capture the generation of the LF-waves. Both LF-wave generated mechanisms, release of bound waves and break point forcing, were validated. Although breakpoint forcing is the important mechanism for reefs, bound waves were verified as well for completeness. Furthermore, the biochromatic wave experiment is a good test to show the effect of the implemented boundary condition including second order wave interactions.

The Noorloos (2003) experiment was used to show the accuracy of the bound waves generated by the wave groups and the energy transfer between the major wave components. The accuracy of the reef-hydrodynamics were validated with the Buckley et al. (2015) experiment.

4.2 Noorloos experiment

Noorloos (2003) studied bichromatic waves on a plane beach with a flume-experiment. Due to the bichromatic wave group, the bound wave frequencies are known. Thus, these waves can be filtered from the time series. Therefore, this experiment can be used to show the effect of implemented boundary conditions including second order wave interactions. Moreover, this experiment shows the accuracy of the energy transfer between the different wave components.

4.2.1 Model set-up

In the experiment a 40m long flume with a 1/35 sloping beach was used. At 80 locations the water level was measured (frequency of 25Hz). The experimental set-up is shown in Figure 4.1. A piston-type of wave board with reflection compensation was used to generate the primary and second order waves. Eight different biochromatic waves were studied where both the sub-harmonic amplitude (test B1 till B4) and sub-harmonic frequency were varied (test A1 till A4). Test A1, A4 and B4 were modelled as part of this thesis. Their settings are summarized in Table 4.1. In test A1 most of the sub-harmonics were dissipated whereas in test A4 most of the sub-harmonics were reflected. Additionally test B4 is modelled because this test contains the largest amplitude of the bound long wave.

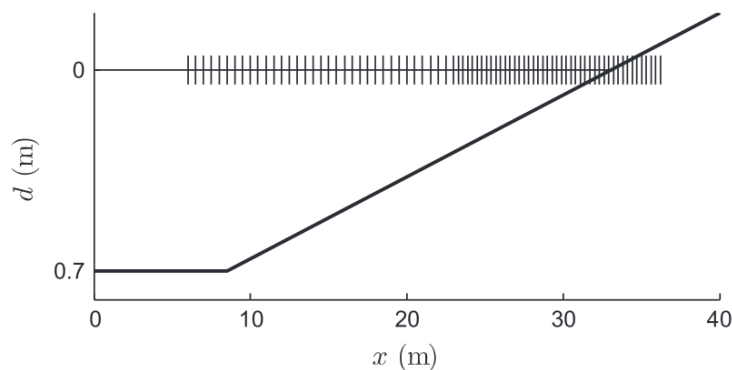


Figure 4.1: Overview of the laboratory step-up used in the Noorloos (2003) experiment. The vertical lines represent the location of the wave gauges.

CHAPTER 4. VALIDATION: HYDRODYNAMICS

Table 4.1: Wave conditions for the three experiments which are modelled within this thesis. f_1 and f_2 are the primary wave frequency, f_b is the bound sub-harmonic and kd the maximum normalized water depth

Test	f_1 [Hz]	f_2 [Hz]	f_b [Hz]	a_1 [m]	a_2 [m]	kd [rad]
A1	0.67	0.48	0.19	0.06	0.012	2.0
A4	0.62	0.53	0.09	0.06	0.012	1.8
B4	0.65	0.50	0.15	0.06	0.036	1.94

The model boundary is located at the first wave gauge ($x = 6m$). A resolution of $0.025m$ was used to discretise the domain. This corresponds with 30 grid points per wave length for the super-harmonics. The threshold above cells are considered wet, was changed to $0.001m$ (keyword eps). It appears that a higher value resulted in too much reflection of the sub-harmonics. At the boundary a weakly reflective boundary condition was used which impose a combination of the incoming and target velocity to prevent reflections.

The formulation as described in section 3.4 was used to generate the boundary time series for both U and Δu when XBeach-nh+ was used. For biochromatic waves the frequency ($f_b = f_1 \pm f_2$) and wave number ($k_b = \sqrt{k_1^2 \pm k_2^2}$) can easily be determined from the primary wave components. The interaction coefficient described in section 3.5 was used to compute the amplitude of the bound waves,

$$a_b = a_1 a_2 D_h \quad (4.1)$$

Where a_b is the bound wave amplitude and a_i the amplitude of the primary waves. The phase of the bound waves is determined by the sign of the interaction coefficient. In section A.1 of the appendix the time-series of these bound waves (sub and super component) is shown. The effects of including these interactions at the boundary, showed that only the addition of the sub-harmonics improve the results (see section 4.2.4). Therefore, all results were computed with only the sub-harmonics included in the boundary signal.

The three tests were modelled with three different XBeach settings: the depth-averaged formulation (nh), the reduced two layer model with $\alpha = 0.33$ (nh+2DV) and the reduced two layer model with $\alpha = 0.0$ (nh+1DV). With the results of these runs it is possible to show the effects of both the improved numerical formulations in nh+ and the effects of the second reduced layer.

4.2.2 Calibration

Both the breaking steepness and the bottom friction were calibrated for test A4, because this test contains the largest reflective sub-harmonic. The breaking steepness is a parameter which initiate breaking by neglecting the non-hydrostatic pressure for cells which have a certain steepness (See appendix G.5). First, the breaking steepness was calibrated based on the

location of the breaking point. Thereafter, the bottom roughness was calibrated. The Manning formula ($c_f = \sqrt{gn^2/h^{1/3}}$) was used as bottom friction formulation, because it depends on the water depth and it is found that friction is enhanced in the surf-zone (Feddersen et al., 2003). All the three XBeach modes were calibrated (nh, nh+1DV and nh+2DV). These results are shown in appendix A.2. To quantify the skill, both the relative bias (rel. bias) and the scatter index (SCI) were computed (See section F of the appendix).

For nh+2DV and nh+1DV a breaking steepness of 0.4 gave the best results, when considering the location of the breaking point. However, nh requires a breaker steepness of 0.3 for an accurate representation of the breaker point. A reason for the lower breaking steepness could be caused by too much damping in nh. Therefore, the wave height is lower at the breaker point, which requires a lower breaking steepness to initiate breaking. The different friction coefficient mostly affects the sub-harmonics, because these waves 'feel' the bottom earlier than the primary waves. When comparing the responds of the sub-harmonics it is seen that nh+2DV needs a $n = 0.01s/m^{1/3}$, nh+1D needs a $n = 0.005s/m^{1/3}$ and nh needs a $n = 0.01s/m^{1/3}$. Apparently, there is too less damping when nh+1D is used compared to nh+2DV. This could be caused by the fact that the bed shear stress is also included in the equation of Δu when using nh+2DV. This means that the bed shear stress is only included in the lower layer (u_1). When the velocity in the lower layer would be slightly smaller than the second layer, the resistance in nh+2DV will also be slightly smaller. This could cause the difference for the friction coefficient.

4.2.3 Results and discussion

The skill scores of the XBeach-nh+ runs for all the individual tests are shown in Table 4.2. Note that these skill scores are not completely representative for the skill as a deviation in the phase has a larger effect on the skill score than a deviation in amplitude. The sub-harmonic wave height was obtained by applying a band filter to the difference frequency including their higher components ($m\Delta f = m(f_1 - f_2)$). In this way the steepening of the sub-harmonics is also included in the signal. In a similar way the wave height of the super-harmonics was determined ($m(f_1 + f_2)$). The filter was applied up to the Nyquist frequency. A tolerance of $0.001Hz$ was used to the filtered frequency. From the filtered spectrum, the low frequency signal is obtained by using an inverse Fourier transformation. The cross shore variation in the wave energy is shown in Figure 4.2 for run A1 and A4. This figure shows the total wave height (H_{rms}), the filtered sub-harmonic wave height ($H_{rms,\Delta f}$) and the filtered super-harmonic wave height (H_{rms,f_1+f_2}). The results of test B4 can be found in the appendix A.3. It chosen to show only test A1 and A4, because these tests represent different sub-harmonic behaviour (reflection and dissipation).

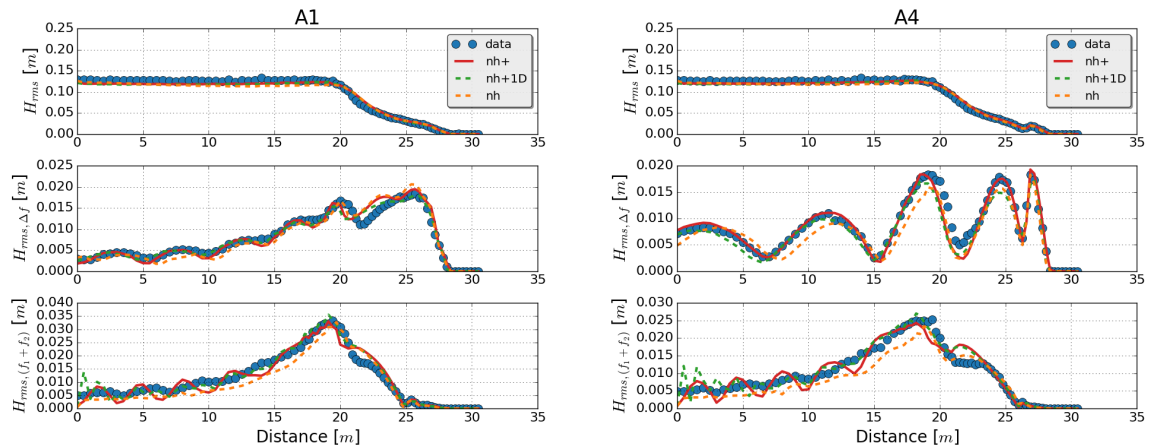


Figure 4.2: The total H_{rms} (upper panel), the filtered sub-harmonic wave height $H_{rms,\Delta f}$ (second panel) and filtered super-harmonic wave height $H_{rms,(f_1+f_2)}$ (third panel). The left figure show the results for test A1 and the right figure shows the results for test A4

It is clearly visible that the sub-harmonics are dissipated in test A1 and reflected in test A4 (standing wave pattern). In general the wave height of the primary waves, the sub-harmonics and the super-harmonics are according to the measurements. Both shoaling and breaking of the super-harmonics and sub-harmonics is represented within the model. Moreover, the reflection of the sub-harmonic (test A4) is accurately simulated. Only experiment B4 is not entirely predicted according to the data. This is a result of the breaking point which is too far onshore. A reason for this difference could be a different type of wave breaking for test B4. The amplitude in test B4 is higher than the other tests, which could require a higher breaking steepness.

When comparing the results of nh and nh+, it is shown that there is a significant improvement when using nh+. The effect of the second reduced layer is less significant when the skill scores of nh+1DV and nh+2DV are compared. Thus, the adapted numerical formulations mostly contribute to a better accuracy. There is too much damping in nh, which result in a decreasing wave height for the region $0 < x < 20m$, whereas the wave height stays constant in nh+. This is a result of the improved numerical formulations in nh+ which have less numerical damping. Due to the relative large kh , it was expected that the second layer would improve the results. Only, for the super-harmonics the additional layer has an effect. Due the large relative depth of the super-harmonics ($kh > 2$), these waves are less accurate predicted with a depth-averaged formulation. Nh always under-predict the super-harmonic wave heights. Comparing nh+1DV and nh+2DV, it can be seen that there arise a spurious wave in nh+1DV at the frequency of the super-harmonics. There is a oscillating with the same frequency as the super-harmonics, but with a smaller wave length. Thus, this is a free wave which follows the dispersion relation ($k_f = k_{dispersion}(f_1 + f_2)$) instead of the bound wave number ($k_b = k_1 + k_2$). The accuracy of the super-harmonics is mainly important for

the accuracy of the breaking point. These super-harmonics lead to a steeper primary waves, which is necessary to initiate breaking. Thus, the lower super-harmonic wave height in nh could also cause (besides of too much wave damping) the lower breaking steepness when using nh. In general nh+1DV gives also a good prediction of the wave hydrodynamics. The first primary wave will propagate with a $\approx 2\%$ slower wave celerity than the physical wave speed, which does not have a large impact on the wave hydrodynamics (e.g. generation sub-harmonic).

The additional computational time within nh+2DV was less than 5% for all tests. Thus, solving the extra equations has a very limited effect on the total computational time.

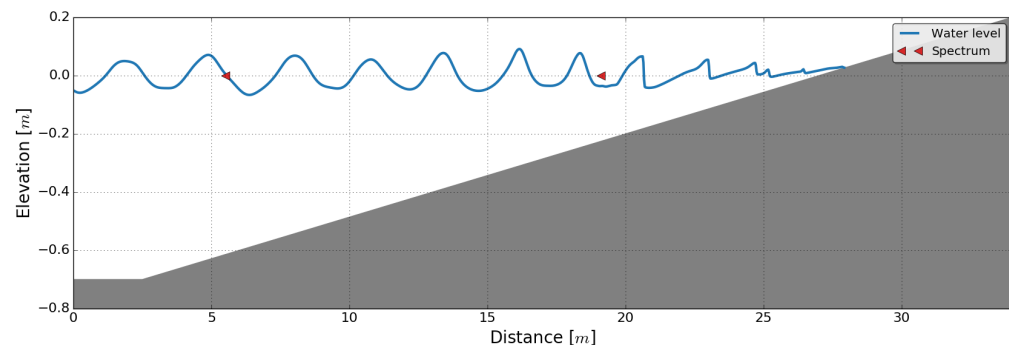
Table 4.2: The skill scores for the different runs of the Noorloos experiment. The results are shown for nh, nh+1DV and nh+2DV. The total skill score was computed for all the observation points for each individual test (A1, A4 and B4).

Run	H_{rms}		$H_{rms,l\Delta f}$	
	SCI	Rel. bias	SCI	Rel. bias
nh+2DV				
A1	0.08	-0.032	0.15	0.011
A4	0.06	-0.020	0.16	-0.032
B4	0.09	-0.015	0.13	-0.071
total	0.09	-0.015	0.13	-0.071
nh+1DV				
A1	0.08	-0.044	0.12	-0.012
A4	0.06	-0.032	0.20	-0.132
B4	0.08	-0.021	0.11	-0.059
total	0.08	-0.021	0.11	-0.059
nh				
A1	0.10	-0.054	0.17	0.001
A4	0.07	-0.039	0.24	-0.162
B4	0.09	-0.025	0.20	-0.133
total	0.09	-0.025	0.20	-0.133

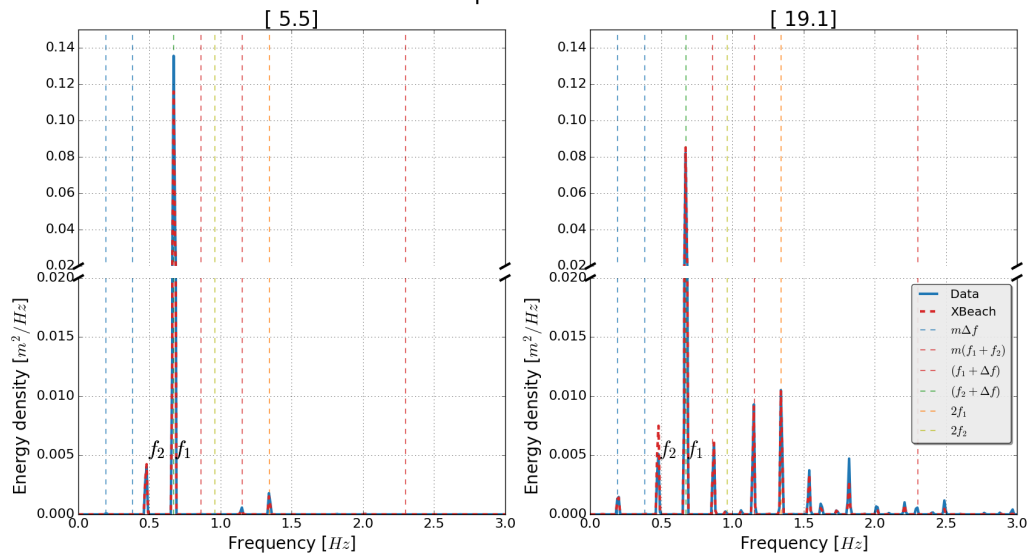
To show the accuracy of the energy transfer between the wave components, the energy density spectrum is plotted in Figure 4.3. The energy density spectrum is plotted for two locations for both test A1 and A4. The axis are divided into two parts to distinguish between the primary and the second order waves. The dashed lines show the sub-harmonic, super-harmonics and other triad interactions. It can be seen that these second order waves becomes more dominant in shallow water when location $5.5m$ is compared to location $19.1m$. From $x > 20$ the waves become much more asymmetrical due to these higher components. Expect for the extreme high components ($f > 1.5Hz$), the energy transfer is predicted reasonable well. The energy transfer is related to the phase mismatch between the free and

CHAPTER 4. VALIDATION: HYDRODYNAMICS

bound wave components (Ohyama T. et al., 1995). Thus, an error in the dispersion relation will affect the energy transfer of these short waves.



Experiment A1



Experiment A4

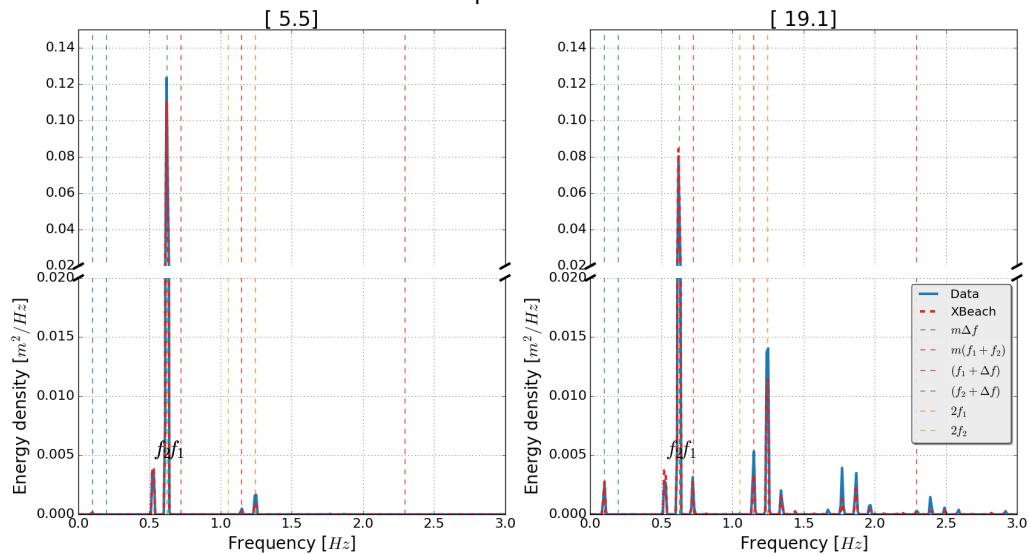


Figure 4.3: Energy density spectrum of two tests of the Noorloos experiment. The upper panel shows the locations of the spectrum with the surface elevation of test A1. The wave interactions are shown as vertical dashed lines. These results were computed with nh+2DV

Both the filtered sub-harmonic and the total water level elevation time series are shown in Figure 4.4. Only, the sub-harmonic is shown, because the sub-harmonic (or bound long waves) are important for most coastal applications (e.g. resonance and dune-erosion). This figure clearly shows the shoaling and steepening of the sub-harmonics. Compared to the measured signal, $nh+2DV$ gives a good prediction of these sub-harmonics. This implies that XBeach captures the generation of bound long waves, which are the dominant source of LF-waves for most plane sloping beaches. These result are shown for a zero centred signal. The prediction for the setup is not shown, because there was much scatter in the measurements.

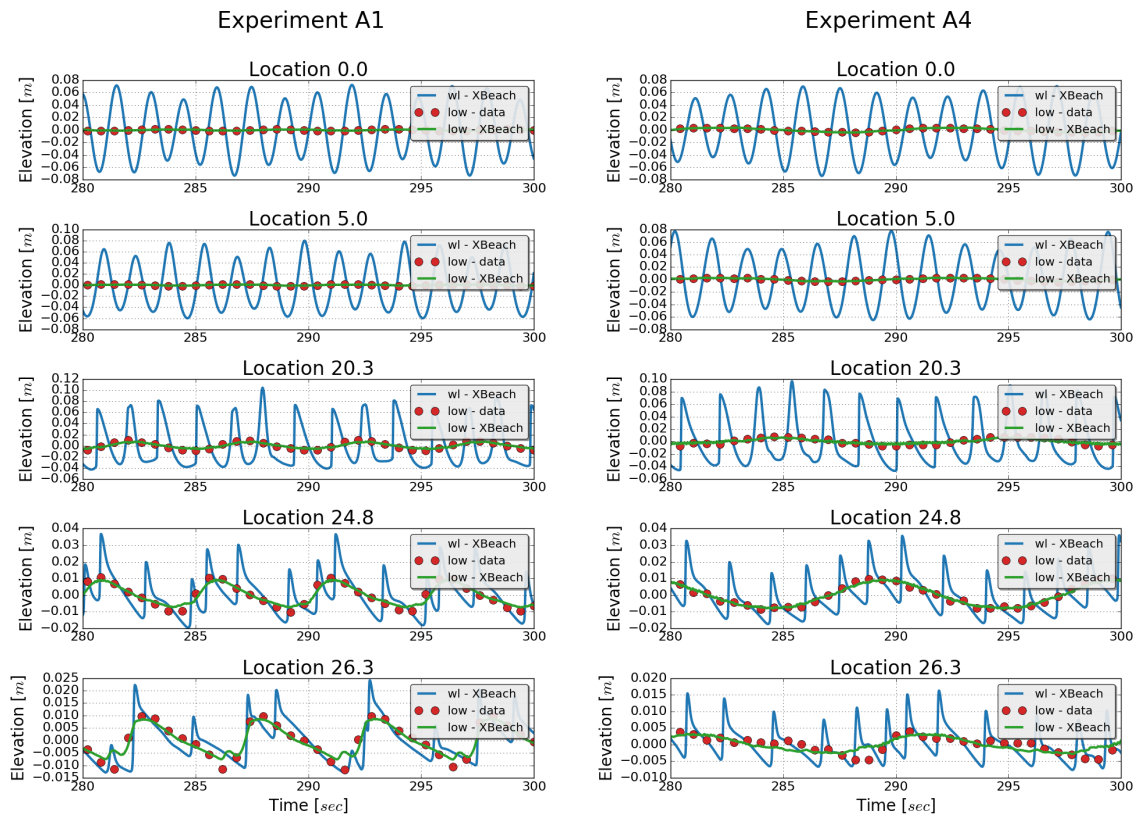


Figure 4.4: Time series for different locations of experiment A1 and A4. The filtered sub-harmonic, total signal and the measured low frequency signal are shown. These results were computed with $nh+2DV$

4.2.4 Sensitivity of the second order wave interaction at the boundary

In Figure 4.5 the effect of the wave interactions at the boundary is shown for both test A1 and A4. The inclusion of the sub-harmonics clearly improves the results. On the other hand, the inclusion of the super-harmonic does not improve the results. An explanation could be that

the relative depth of the super-harmonic ($kh = 3.7$) is too large to resolve accurately within the model. If this is the case the super harmonics can only be used for a boundary conditions in relative shallow water where the kh value of the super-harmonic is not too high.

The suppresses of the long spurious waves, caused by the wrong sub-harmonics at the boundary, is more important than the short spurious waves, because the long waves can propagate much further into the domain. Mostly these long waves don't break and, therefore, could cause more problems (e.g. resonance).

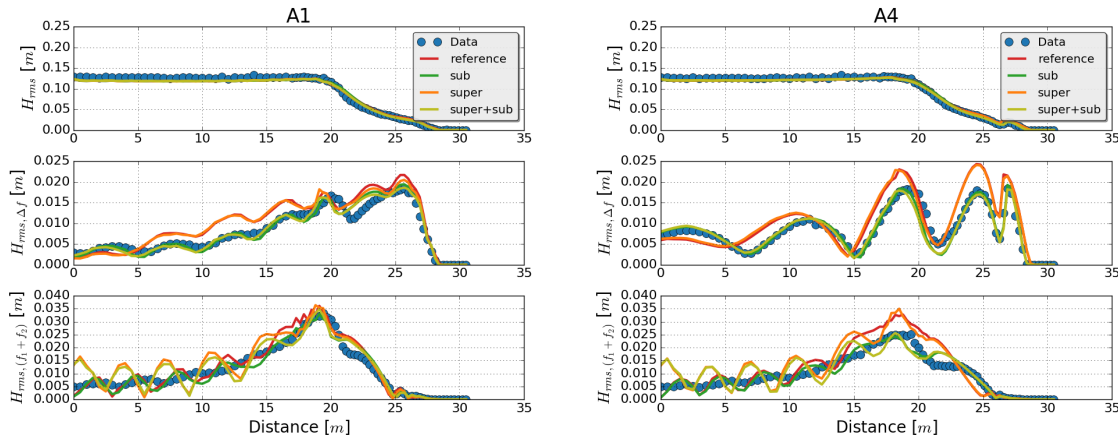


Figure 4.5: Comparison of the runs with different boundary conditions. The following boundary conditions were modelled: only primary waves (reference), including sub-harmonics (sub), including super-harmonics (super) and including both super and sub-harmonics (super+sub). The left figure shows the test A1 and the right panel test A4. The upper panel shows the total wave height. The second panel the sub harmonic and the third panel the super harmonic.

4.3 Buckley experiment

The hydrodynamics at a fringing reef are different than that for a plane beach. Due to the steep fore reef, waves will break in a narrow breaking zone at the reef crest. Therefore, break-point forcing is the dominant mechanism of LF-waves. To validate the reef hydrodynamics, an experiment of a fringing reef was modelled (Buckley et al., 2015).

4.3.1 Model set-up

In the experiment a 55m long flume was used to measure the wave propagation over a fringing reef. The profile consist of a 1 : 5 reef slope, a 14m long reef flat and a 1 : 12 sloping beach. The scale is 1 : 36 which makes this profile comparable to real coral reefs (Figure 4.6). To account for the finite volume of water in the wave-flume, the bed level is corrected within XBeach. Due to the setup on the reef the water depth at the boundary is slightly shallower than the still water depth in the wave-flume. There exist a boundary formulation for wave flumes in XBeach, but this formulation is not valid for short waves and therefore not applied.

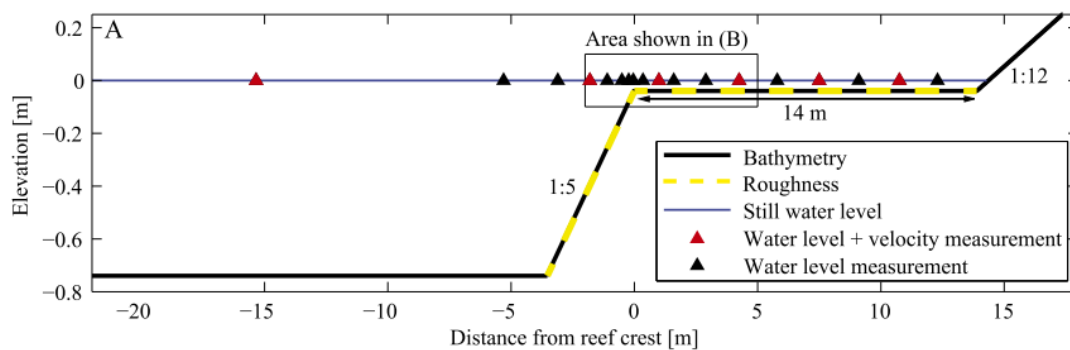


Figure 4.6: Experimental set-up of the Buckley et al. (2015) experiment. The represented field scale is 36 times larger. Source: Buckley et al. (2015)

A spatial varying grid was used to optimize the computational effort. The grid resolution is based on 80 grid points per wave length (period of 2s). In appendix B.2 the effects of different resolutions are shown. Furthermore, the effect of the layer distribution was verified. In appendix B.3 the results for different α values are shown, but it appears that the default value of 0.33 gives the best result.

The model boundary is located at the first measurement location. During the experiments irregular waves from a TMA spectrum were generated at the boundary. 16 different wave conditions were studied. From these 16 runs, five tests were modelled with XBeach, where both the water level and the wave height was varied. In Table 4.3 the settings for these tests are shown. The simulation time was set to 2500s (500s spin-up), which is the same as the

measured period (2000s). These five tests were modelled with both nh+2DV and nh+1DV to show the effect of the additional reduced layer in nh+2DV.

To compare different simulations the scatter index and the relative bias were used. However, due to the forcing of random waves, the accuracy of the skill score is related to time series period. The achieved accuracy depends on the number of waves in the signal. Thus, the accuracy of the LF-waves can be less accurate computed than the total wave height. To get an indication of the accuracy for a measured signal of 2000s, different runs of 2000s were compared to a run of 6000s (assuming that the wave statistics does not change much for this run). In appendix B.1 these results are shown. From these results the following uncertainties were found in the measurements: SCI of 0.01 and rel. bias of 0.01 for the total wave height, SCI of 0.04 and rel. bias of 0.02 for the LF-waves and SCI of 0.02 and rel. bias of 0.02 for the setup. When the skill scores are compared these values give an indication of the accuracy of the measurements.

Table 4.3: Model set-up for the different runs. The reef depth ($h_{0,r}$) represents the still water depth at the reef and the kh is computed for the peak period

test	H_{rms} [m]	T_p [sec]	$h_{0,r}$ [m]	kh of T_p [rad]
1	0.03	2.26	0.04	0.85
2	0.06	2.26	0.04	0.85
4	0.12	2.26	0.04	0.85
9	0.06	2.26	0.00	0.82
12	0.06	2.26	0.09	0.89

4.3.2 Calibration

Both the friction coefficient and the breaking steepness were calibrated for run 4. This runs was used for the calibration as it is forced with the largest wave height. Both nh+1DV and nh+2DV were calibrated. First, the breaking steepness was calibrated based on the location of the breaking point. Secondly, the bottom friction was calibrated based on the LF-wave energy. The results for the calibration are shown in appendix B.2.

For nh+2DV a breaking steepness of 0.8 and a manning coefficient of $0.005 \text{ s/m}^{1/3}$ gave the best results and a breaking steepness of 1.2 with a manning coefficient of $0.005 \text{ s/m}^{1/3}$ gave the best result for nh+1DV. The choice of breaking steepness does not have a large effect on the result. This implies that the breaking point will not vary much when the breaking steepness is varied. The waves will shoal very quickly, which gives almost the same location of the breaking point for different breaking steepness. The influence of the bottom friction is more important. Especially, the LF-waves are affected by the bottom friction.

4.3.3 Results and discussion

Figure 4.8 gives an overview of all the runs. The colors indicate the tests and the symbols the output location. The LF-wave heights were obtained by integrating the spectrum between the frequencies: 0.02 and 0.2 Hz and the short waves by integrating between 0.2 Hz and the Nyquist frequency. Both the result with nh+2DV (upper panel) and nh+1DV (lower panel) were shown. It can be seen that this additional layer improves the results. Especially, the setup and LF-waves benefit when a second reduced layer is applied. The skill scores of the individual runs with nh+2DV are shown in Table 4.4.

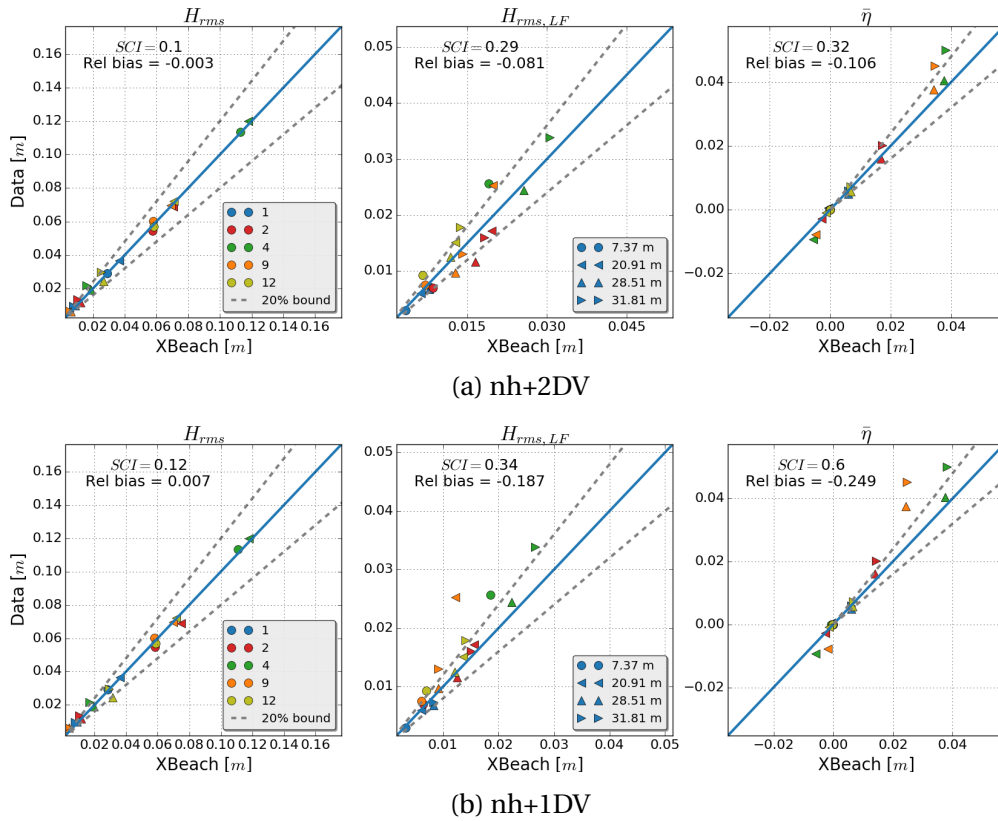


Figure 4.7: XBeach plotted against the data for the total wave height (left), LF-wave height (middle) and the setup (right). The five different test are plotted in different colors and the locations are indicated with a different symbol. These results are both plotted for nh+2DV (upper panel) and nh+1DV (lower panel).

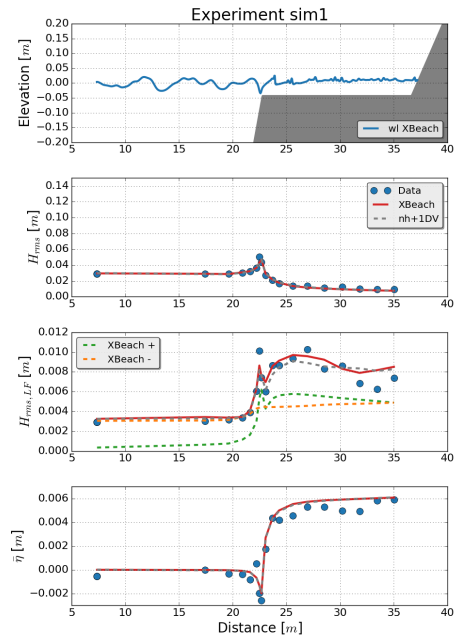
The cross shore variability of the bulk wave statistics are shown in Figure 4.8. Note that run 2 is shown twice for comparison. For every test, the wave height (H_{rms}), the LF-wave height ($H_{rms,LF}$) and the setup ($\bar{\eta}$) are plotted. To distinguish between the incoming (dashed green) and outgoing (dashed orange) LF-waves, the Guza et al. (1985) method was applied. The

reference water level is set to the mean offshore water level (measured at the second wave gauge). The results of nh+2DV are shown with red lines and the results of nh+1DV are shown with grey dashed lines.

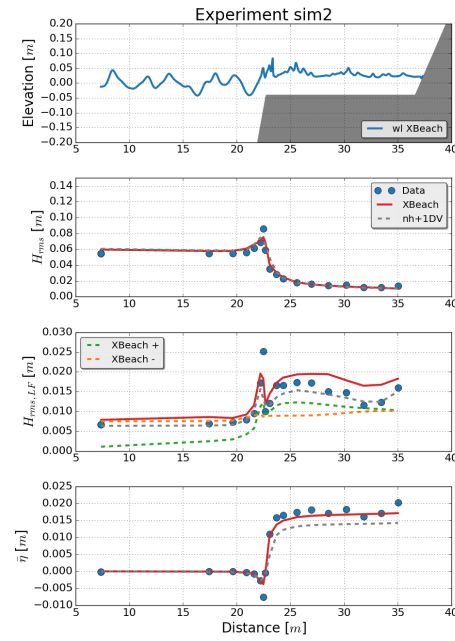
In general nh+2DV gives a good prediction of the reef hydrodynamics. Both generation of LF-waves and the water level gradient at the reef crest is similar to the measurements. Only for the larger wave height and larger reef depth, there is a discrepancy in LF-wave energy between the model and measurements. Most of the scatter is present in the setup, which is also found for other non-hydrostatic models (Yao et al., 2012; Skotner and Apelt). Mostly the missing roller energy is given as explanation for the underestimation of the setup, which would suggest that the error increases for larger wave heights. This could be the reasons why there is an underestimation of the setup and the LF-waves for run 4 (largest wave height). There is not a clear reason why there is an underestimation of the setup for test 9, but it will be a result of the approximation of wave breaking. For this particular test the decrease in wave energy is not that steep as given in the measurements, which results in a lower setup. Comparing the result for nh+1DV and nh+2DV, it is shown that the results improve for two tests (test 2 and 9). Both the LF-wave height and the setup are better modelled with nh+2DV for these tests. This means that the breaking point is better captured with nh+2DV for these test, which can also be seen in the cross shore variability of the wave height. Nh+1DV gives a less steep drop in wave energy at the breaking point than nh+2DV. It is not known why only these two tests give a better result when using the additional reduced layer. The relative depth of the peak period is lower than 1 for all tests. This means that frequency dispersion is accurate modelled for the waves around the peak period. Apparently, the additional of an extra layer (and vertical velocity) improves the breaking mechanism for test 2 and 9.

Table 4.4: The computed skill score for the different test of the Buckley experiment

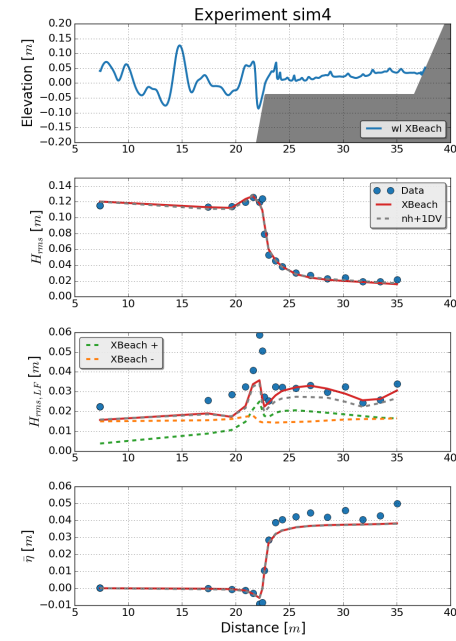
Run	H_{rms}		$H_{rms,LF}$		$\bar{\eta}$	
	SCI	rel. bias	SCI	rel. bias	SCI	rel. bias
1	0.1	-0.025	0.12	0.05	0.29	0.19
2	0.11	0.035	0.23	0.13	0.17	-0.05
4	0.08	-0.005	0.28	-0.18	0.24	-0.13
9	0.07	-0.032	0.13	-0.013	0.16	-0.054
12	0.10	0.005	0.21	-0.19	0.32	0.16



(a) $H_{rms} = 0.03m$



(b) $H_{rms} = 0.06m$



(c) $H_{rms} = 0.09m$

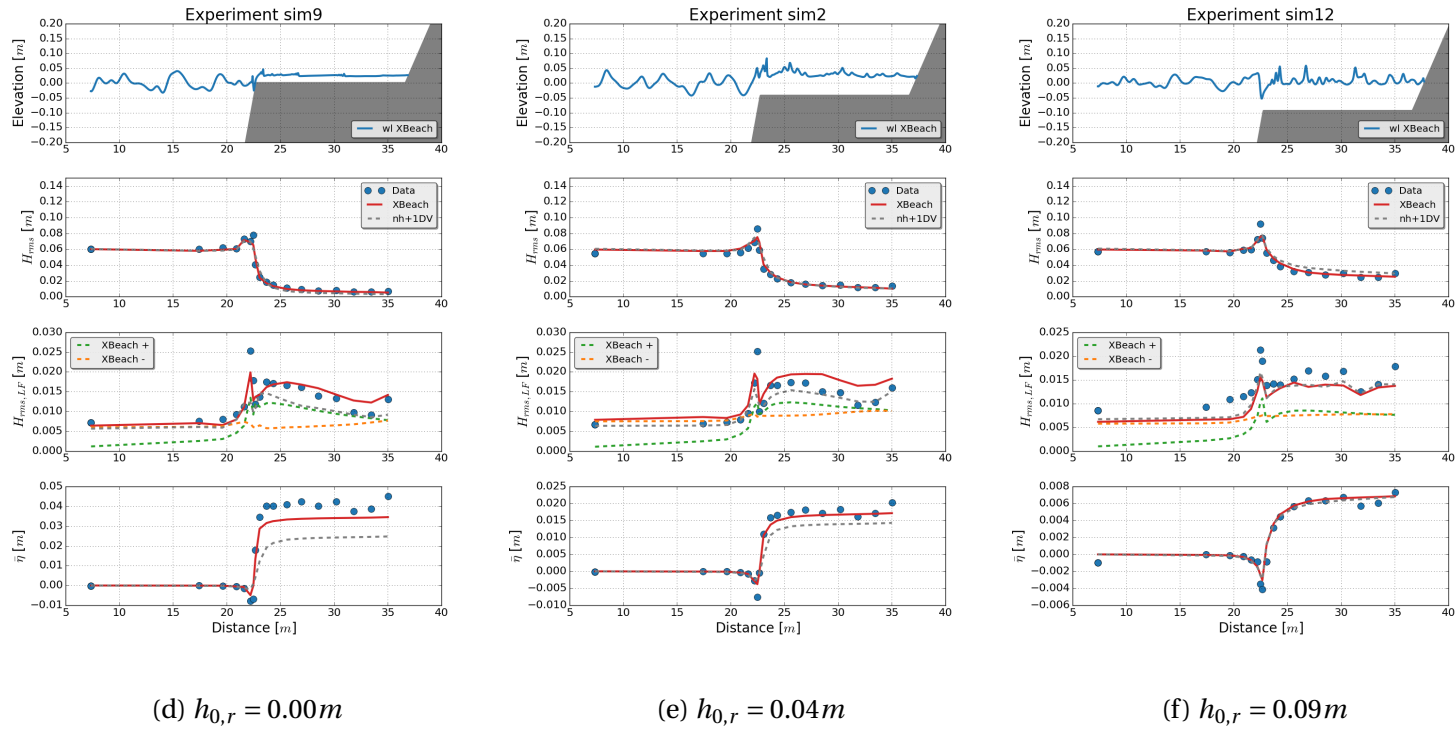


Figure 4.8: The results for test 1, 2, 4, 9 and 12. For every test the upper panels show the model domain, the second panel the rms-wave height, the third panel the LF rms-wave height and the last panel the mean water level. The red line is computed with nh+2DV and the grey dashed line with nh+1DV. The data is shown with blue dots. Furthermore, the LF-waves were filtered for outgoing (dashed orange) and ingoing waves (dashed green).

4.4 Conclusion

Two lab experiments were used to show the accuracy of XBeach-nh+ (nh+). Both bichromatic waves over a plane beach (Noorloos experiment) and random waves over a fringing reef were modelled (Buckley experiment).

The Noorloos experiment showed that nh+ is capable in modelling the energy transfer between the important wave components. Both tests of a dissipative and a reflective sub-harmonic were accurately modelled. The steepening of the sub-harmonic shows that the generation of higher components (of the sub-harmonic) is captured in the model. A total relative bias of -0.0015 and a SCI of 0.09 were found for the total wave height and a relative bias of -0.071 and a SCI of 0.13 were found for the sub-harmonic.

Nh+ is capable in modelling the energy transfer between the major wave components which causes both generation of bound long waves (LF-waves) and steeping of the primary waves.

Comparing the different models, it was shown that the reduced two layer model (nh+) gives better results. Although the large relative depth ($kh = 2$), this is mainly due to better numerical formulation, whereas the second reduced layer does not have a large impact for this particular case.

The inclusion of the sub-harmonics at the boundary has a large effects on the results by suppresses the spurious waves. However, the inclusion of the super-harmonics does not improve the result for this particular test. This could be due to a too large relative depth of the super-harmonics which cannot be resolved in the model. Therefore, it is only advised to use this boundary condition for a spectrum with relative short wave period.

A flume test of a fringing reef was used to show the accuracy of nh+ for a reef environment. Compared to the measurements, nh+ is capable in modelling the bulk wave statistics (rel. bias of -0.003 for the H_{rms} and a rel. bias of -0.081 for the LF-waves). Most of the uncertainty is present in the setup (rel. bias of -0.106). In general the LF-waves, generated by breakpoint-forcing, are captured for different wave conditions. Both the tests with a varied mean water level and wave height were represented with the model. When nh+2DV is compared to nh+1DV, it was shown that there is only a difference for two tests. Thus, the addition of the reduced second layer results in a robust prediction of the hydrodynamics, whereas nh+1DV does not represent all the wave conditions.

Nh+ is capable in modelling the reef hydrodynamics accurately for different wave conditions

5

In-canopy flow model

Within this chapter the formulation of the porous in-canopy flow model is given. Both the governing equation (section 5.1 and 5.2) and the numerical implementation (section 5.4) are explained in this chapter. An overview of the computational approach is shown in 5.5

5.1 Conceptual model

The porous in-canopy model is included as a sub-grid model in XBeach. This means that the domain of the in-canopy model falls within the flow grid-cell and subsequently that the in-canopy model is forced with the depth averaged quantities (Figure 5.1).

Such an approach has the advantage that it requires less computational effort to compute the in-canopy velocity and that it makes the model less vulnerable to instabilities. When the canopy layer would be added below the flow grid-cell, the vertical fluxes between the cells must be included. This would require a second equation (continuity equation) to solve the in-canopy flow. Secondly, this also requires that the forcing of the in-canopy cell must be computed, which increases the computational time.

Secondly, by applying a sub-grid approach, the in-canopy model can be used for corals which become emergent or cover a large part of the water depth. When the canopy layer would be formulated below the flow grid-cell, it could lead to an unwanted layer distribution. For example, emergent corals would result in a canopy layer which covers the total water depth and a second layer with thickness of zero. This would increase the complexity of the model and requires that the forcing of the canopy layer must be independent of the second flow grid-cell. With the sub-grid approach the forcing can always be computed from

the depth averaged flow grid-cell even for emergent vegetation.

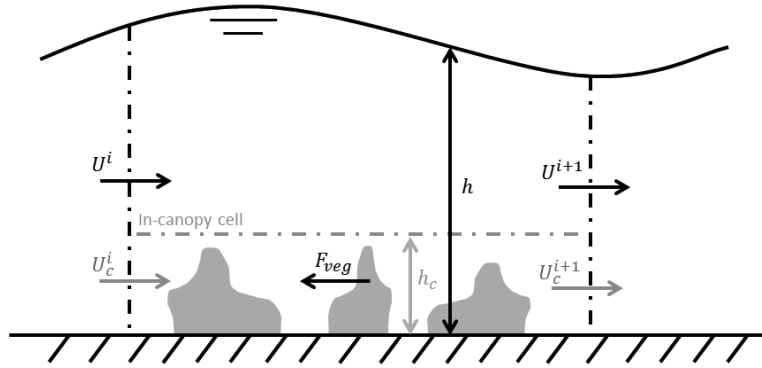


Figure 5.1: Schematic representation of the in-canopy model (grey) within the XBeach model (black). The U is the depth averaged velocity, U_c the in-canopy velocity, h_c the canopy height, h the water depth and F_{veg} the canopy-induced force.

5.2 Governing equation

The equation of the in-canopy flow is derived from porous flow theory. In Sollitt et al. (1872) a pore averaged momentum balance for a porous media is given as (neglecting advection),

$$\frac{\partial \vec{U}}{\partial t} = -\frac{1}{\rho} \nabla(P) + \vec{R} \quad (5.1)$$

Where \vec{U} is the velocity averaged over the pores, P the corresponding pressure and \vec{R} the resistance. The formulation is implemented in 2D, but for simplicity the formulation is shown for the u-direction. The same approach is followed to obtain the equation for the v-direction. The resistance forces were derived from steady and unsteady relationships. For the steady relationship the following formulation is used (Ward, 1964; Gu and Wang, 1991),

$$R_{steady} = \frac{\mu}{K_p} \epsilon U + \beta U |U| \quad (5.2)$$

Where μ is the viscosity, K_p the intrinsic permeability, β an empirical coefficient and ϵ the porosity. The first term describes the laminar resistance (low Reynolds number) and the second term the turbulent resistance (high Reynolds number). Note that the β -coefficient is not dimensionless and does not represent the drag coefficient.

The unsteady stress relationship is given by an additional term which represents the inertia of the flow. This inertia force is given as the product of the displacement of the fluid mass, inertia coefficient (C_M) and the acceleration of the fluid particles,

$$R_{inertia} = \frac{1-\epsilon}{\epsilon} C_M \frac{\partial U}{\partial t} \quad (5.3)$$

CHAPTER 5. IN-CANOPY FLOW MODEL

In Lowe et al. (2008) this equation is rewritten to an equation for the in-canopy velocity in terms of λ_p ($\lambda_p = 1 - \epsilon$). Furthermore, Lowe et al. (2008) suggested to include a canopy averaged shear stress term. For short waves this shear stress is negligible, but for long period-waves this terms can become more important. This canopy averaged shear stress is given by,

$$\frac{1}{h_c} \frac{\partial \tau}{\partial z} = \frac{1}{2} C_f \frac{|U_\infty| U_\infty}{h_c} \quad (5.4)$$

Where C_f is a friction coefficient, h_c the canopy height and U_∞ the free stream velocity. However, it is argued that this shear stress term could be rewritten for a sub-grid formulations as,

$$\frac{1}{h_c} \frac{\partial \tau}{\partial z} = \frac{1}{2} C_f \frac{|U_\infty - U_c| (U_\infty - U_c)}{h_c} \quad (5.5)$$

Instead of the free stream velocity the velocity-difference between the canopy and the depth averaged velocity was used. This formulation will be more representative than using a depth averaged velocity as shear stress term.

Thus, for a complete description of the in-canopy flow the following momentum equation is used (Lowe et al., 2008),

$$\underbrace{\frac{dU_c}{dt}}_{\text{Local acceleration}} = \underbrace{-g \frac{\partial \eta}{dx}}_{\text{Pressure gradient}} - \underbrace{\frac{\mu(1-\lambda_p)}{K_p} U_c}_{\text{Laminair resisting force}} - \underbrace{\beta U_c |U_c|}_{\text{Drag}} - \underbrace{\frac{C_m \lambda_p}{1-\lambda_p} \frac{dU_c}{dt}}_{\text{Inertia force}} + \underbrace{\frac{|U_\infty - U_c| U_\infty - U_c}{2h_c / C_f}}_{\text{Shear stress}} \quad (5.6)$$

with the following variables,

- U_c : In-canopy velocity [m/s]
- U_∞ : Free stream velocity [m/s]
- λ_p : Dimensional plan area ($1 - \epsilon$) [-]
- K_p : Permeability [m^2]
- C_M : Inertia force coefficient [-]
- μ : Kinematic viscosity [m^2/s]
- h_c : Canopy height [m]
- β : β -coefficient [m^{-1}]
- C_f : Empirical friction coefficient [-]
- η : Surface elevation [m]
- g : Gravitational acceleration [m/s^2]

The in-canopy velocity is used to determine the canopy-induced force on the depth-averaged flow computation. From the in-canopy velocity U_c the canopy-induced force is computed as,

$$F_{veg} = -\rho h_c \left[\beta |U_c| U_c + \frac{\mu(1-\lambda_p)}{K_p} U_c + \frac{C_m \lambda_p}{1-\lambda_p} \frac{dU_c}{dt} \right] \quad (5.7)$$

This force is included in the depth-averaged horizontal momentum equation,

$$\frac{\partial u}{\partial t} + u \frac{\partial u}{\partial x} = -g \frac{\partial \eta}{\partial x} - \frac{\partial \bar{q}}{\partial x} + \frac{F_{veg}}{\rho h} + \frac{\tau_b}{\rho h} + S \quad (5.8)$$

where S represents the source terms. When using XBeach-nh+ this means that the resistance force has a contribution in both layers. Theoretically, it could easily be divided over the two layers. For example, the canopy-induced force difference could be included in the equation for Δu ($\Delta F = F\alpha h - F(1 - \alpha)h$). However, the in-canopy model is derived for shallow water conditions, which implies that both layers give the same velocity. Therefore, the canopy-induced force is only implemented in the equation for U .

The corals will not only affect the flow by a resistance term, but it will also affect the flow area. Therefore, it is argued to apply a bed correction to the grid cells with corals. This formulation is described and verified in appendix C. However, it appears that this bed correction does not improve the results. Therefore, all the in-canopy simulations in thesis are shown without the bed correction.

To summarize the following assumptions were made to derive the in-canopy model,

- The advection terms were ignored in the in-canopy model.
- The velocity does not change within the canopy ($kh_c \ll 1$).
- The depth averaged velocity and hydrostatic pressure were used as forcing ($kh \ll 1$).
- The vertical canopy velocity are ignored.

It is argued that the shallow water assumption is not a large issue, because most of the corals grow on the shallow reef flat. Secondly, the corals which grow in deeper water will not have a large affect on the hydrodynamics, because the effects of the bottom is less important for the waves. These shallow water conditions also suggest that the vertical canopy velocity can be neglected, because the horizontal velocity is much larger than the vertical velocities. Due to the fact that the resistance is mostly much larger than advection terms, advection is mostly neglected for porous media flows (Sollitt et al., 1872).

5.3 Canopy parameters

The in-canopy model introduces multiple new parameters related to the canopy properties. However, these parameters are not always known and more importantly not easily to determine. Therefore, this section describes the parameter space of these canopy parameters based on known relationships or found values in literature.

To estimate the β -coefficient (and K_p) for a porous media the "modified Ergun equations" can be applied. These relations are given by (Macdonald et al., 1979),

$$K_p = \frac{D_{eq}^2 (1 - \lambda_p)^3}{a_0 \lambda_p^2} \quad (5.9)$$

$$\beta = \frac{b_0 \lambda_p^3}{D_{eq}(1 - \lambda_p)} \quad (5.10)$$

where D_{eq} is a characteristic length scale defined as the equivalent mean sphere diameter (6 times the volume-area ratio). Macdonald et al. (1979) showed that these relations give a reasonable result for experiments of different materials like spheres, cylinders, granular filters and fibrous mats. Both the a_0 and b_0 describe the shape of the object, which is depended on the porous media. However, within this thesis the empirical constants were set to the same values as used in Lowe et al. (2008), which is an a_0 of 180 and a b_0 of 1.8. It was shown in Lowe et al. (2008) that these values represent the β -coefficient within 50% for all the experiments. The sensitivity analyses in this thesis showed that an uncertainty of 50% in the drag force will result in a 5% error for the in-canopy velocity. When the geometry is better described with the lambda parameters the following formulation could be used to determine the β -coefficient (Coceal and Belcher, 2004),

$$\beta = \frac{\lambda_f C_d}{\lambda_p 2h_c} \quad (5.11)$$

Where C_d is the dimensional drag coefficient. In Lowe et al. (2008) the β -coefficient was measured for flow through coral species in a wave flume, which gave a β of 4 to 27 m^{-1} for different experiments. Using equation 5.11 a similar range is found for a varied λ_f (0.5-1.5), varied canopy height (0.1-0.3 m) and constant C_d of 1.

Within this thesis the laminar resistance terms does not have any influence and therefore the K_p is not further elaborated. Only for very fine porous material, the laminar term becomes important.

Compared to the β -coefficient there is not much known about the inertia coefficient. Van Gent (1995) and Gu and Wang (1991) found a C_M of ≈ 0.5 , whereas Mccorquodale et al. (1978) measured a C_M of 2. Due to the large scatter a value of 1 ± 0.5 is used within this thesis.

The empirical friction coefficient for wave conditions over reefs ranges from 0.01-0.3 for oscillating flows (Lowe et al., 2005b; Nelson, 1996). However, most bed shear stress formulation do not distinguish between the bed shear stress and the canopy-induced forces, which will result in a larger C_f . Thus, Lowe et al. (2005b) suggest a C_f of $O(0.01)$ when considering his experimental results. On the other hand the shear stress formulation was adjusted in XBeach by using the velocity difference between the in-canopy and free stream velocity. This will give a better description of the shear force, but means the found friction coefficient cannot be directly used in this formulation. The adapted shear stress formulation will give a lower shear stress when the same empirical friction coefficient is used ($U^2 > (U - U_c)^2$). It can be derived that the adapted friction coefficient is by,

$$\frac{\tilde{C}_f}{C_f} = \frac{1}{(1 - \alpha)^2} \quad (5.12)$$

Where \tilde{C}_f is the shear stress coefficient for the adapted formulation and α the ratio between the in-canopy velocity and the free stream velocity. Based on this relation, it is argued that a value of $O(0.1)$ should be applied.

5.4 Numerical implementation

Equation 5.6 is discretised using forward differences. The quadratic in-canopy velocity is linearized by staggering the time steps. This is the same approach as used within Lowe et al. (2005b). This results in the following scheme,

$$\frac{U_c^{i+1} - U_c^i}{\Delta t} = -g \left(\frac{\partial \eta}{\partial x} \right)^i - \frac{\mu(1-\lambda_p)}{K_p} U_c^{i+1} - \beta U_c^{i+1} |U_c^i| - \frac{C_M \lambda_p}{1-\lambda_p} \frac{U_c^{i+1} - U_c^i}{\Delta t} + \frac{|U_\infty^i - U_c^i| U_\infty^i - U_c^i}{2h_c / C_f} \quad (5.13)$$

Rearranging results in an equation of the in-canopy velocity for the next time step,

$$U_c^{i+1} = \frac{-g \left(\frac{\partial \eta}{\partial x} \right)^i + \frac{|U_\infty^i - U_c^i| U_\infty^i - U_c^i}{2h_c / C_f} + A U_c^i}{A + \frac{\mu(1-\lambda_p)}{K_p} + \beta |U_c^i|} \quad (5.14)$$

With A is,

$$A = \left(1 + \frac{C_M \lambda_p}{1-\lambda_p} \right) / \Delta t \quad (5.15)$$

This formulation is implemented into XBeach. The horizontal pressure gradient and the free stream velocity are both explicitly formulated. This is necessary because the in-canopy flow must be calculated before the flow computation. The canopy-induced force affects the flow computation which means that the canopy-induced force should be known before the flow computation. The depth averaged velocity is used as estimation of the free stream velocity. When emergent vegetation is modelled, the canopy height is set to the water depth,

$$h_c = \begin{cases} h_c & h_c < h \\ h & h_c > h \end{cases} \quad (5.16)$$

The canopy-induced force is discretized as,

$$F_{veg} = -\rho h_c \left[\beta |U_c^{i+1}| U_c^i + \frac{\mu(1-\lambda_p)}{K_p} U_c^i + \frac{C_M \lambda_p}{1-\lambda_p} \frac{U_c^{i+1} - U_c^i}{\Delta t} \right] \quad (5.17)$$

5.5 Computation chart

An overview of the computation is shown in Figure 5.2. The in-canopy model was implemented in 2D with the option of a spatial varying vegetation-type. For a 2D simulation the same formulation is used for both the u-direction and the v-direction.

CHAPTER 5. IN-CANOPY FLOW MODEL

When the computation starts, the in-canopy module is called every time step. For every cell which is wet and includes corals, the canopy properties (β , ϵ , C_f and h_c) are read from the input file. Then, it is checked whether the corals are submerged or emerged. When emerged the canopy height is bounded by the water depth. Using equation 5.14 the in-canopy velocity is computed. Subsequently, the resistance force is computed based on the in-canopy velocity with equation 5.17. This resistance force is used in the flow computation to include the coral resistance on the mean flow.

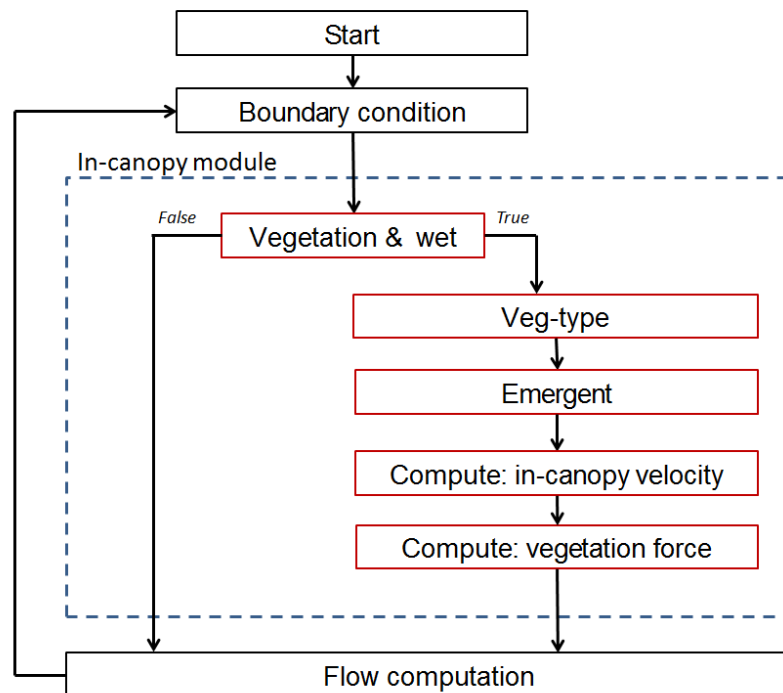


Figure 5.2: Diagram of the in-canopy module. The red boxes are implemented for the in-canopy module

6

Validation: in-canopy flow model

To show the effects of the in-canopy model on the hydrodynamics two different test were used as validation. Firstly, the in-canopy velocity is verified by a lab-test of flow through both cylinders and corals. Subsequently, the effects of the canopy-induced force on the hydrodynamics is shown for a lab-test of a fringing reef with roughness elements.

6.1 Validation: in-canopy flow

Two flume experiments were used to validate the in-canopy velocity. The first experiment is about flow through vertical cylinders (Lowe et al., 2005b) and the second experiment about flow through a coral canopy (Lowe et al., 2008). In the following section Lowe 2005 refers to the first experiment and Lowe 2008 refers to the second experiment.

6.1.1 Model set-up

The flume was represented with a 20m long domain with a grid-spacing of 0.1m. Only the wave conditions at a particular location in the flume were given. Therefore, these conditions were forced at the boundary and the canopy-induced force was set to zero to neglect wave damping. In this way it was possible to validate the in-canopy velocity for the corresponding wave conditions. In the numerical wave-flume the roughness elements were placed over a length of 10m and start 5m from the model boundary. In the experiments both unidirectional and oscillating flow fields were studied. To minimize wave reflection a background current for the oscillating wave experiments was necessary. This background

current was also included in the XBeach simulations for a good representation. However, this means that the anti-reflection compensation could not be used in XBeach. For the oscillating experiments, the model was forced with a time-varying velocity with the addition of the background current. A velocity and water level were imposed at the boundary for the unidirectional experiments.

For the wave experiments the rms-velocity (U_{rms}) was measured at a given water depth and no information about the wave height was given. Therefore, linear wave theory was used to compute the depth averaged velocity related to the measured rms-velocity at the given depth, which is necessary to force the model.

Instead of the in-canopy velocity an attenuation parameter (α) was used as validation parameter. This α represents the ratio of the in-canopy velocity over the free stream velocity (Lowe et al., 2005b),

$$\alpha_w = \frac{U_{c,wave}^{rms}}{U_{\infty,wave}^{rms}} \quad \alpha_c = \frac{U_{c,current}}{U_{\infty,current}} \quad (6.1)$$

Where U_{∞} is the free stream velocity. It was shown in Lowe et al. (2005b) that for an unidirectional case α_c is equal to the second definition ($\lim_{\omega \rightarrow 0} \alpha_w = \alpha_c$). In the experiments particle image tracking technique was used to measure the depth averaged in-canopy velocity and the free stream velocity.

6.1.2 Flume experiment: 1) Lowe 2005

Eight from the 25 experiments of Lowe et al. (2005b) were modelled with XBeach, where both the cylinder spacing (S) and wave period (T) were varied (oscillating runs). The other experiments were not modelled because these experiments require a very large background current, which cannot accurately be modelled with XBeach. The settings of these experiments are shown in Table 6.1.

For every experiment the PIV-velocity measurements were used to compute the canopy parameters. For the unidirectional experiments the C_f was computed from the measured Reynolds stress ($C_f = 2u_*^2 / U_{\infty}^2$). There was no friction coefficient computed for the wave experiments. Therefore, a constant C_f of 0.01 was applied for the wave experiments, which is a similar value as measured for the unidirectional waves. The inertia coefficient was set at 1.5 which is found to give the best results for submerged cylinders (Lowe et al., 2005b). The λ_p ($\lambda_p = 1 - \epsilon$) is related to the cylinder configuration as,

$$\lambda_p = \frac{\pi d^2 / 4}{(S + d)^2} \quad (6.2)$$

Where S is the distance between the cylinders and d the diameter of the cylinder ($= 0.05 m$). The formulation of Coceal (equation 5.11) would probable give the best prediction of the β coefficient, because cylinders can easily be described with both the λ_p and λ_f parameter. However, within this thesis the Ergun relation were preferred because of the porous media

CHAPTER 6. VALIDATION: IN-CANOPY FLOW MODEL

of corals. Thus, even for these tests the modified Ergun relation was applied. To determine the β -coefficient a D_{eq} of $0.075m$ was applied (1.5 times the diameter (Lowe et al., 2008)).

Table 6.1: The parameters for the 6 experiments which are modelled with XBeach. The unidirectional experiments are indicated with a U and the oscillating experiments with a W.

Run	λ_p [-]	k_p [m^2]	β [$1/m$]	C_M [-]	C_f [-]	α [-]
U1: S=5cm	0.20	0.0004	9.4	1.5	0.019	0.12
U7: S=15cm	0.05	0.01	1.4	1.5	0.029	0.33
W2: S=5cm and T=2 sec	0.2	0.0004	9.4	1.5	0.01	0.70
W3: S=5cm and T=3 sec	0.2	0.0004	9.4	1.5	0.01	0.70
W8: S=10cm and T=1 sec	0.08	0.002	2.1	1.5	0.01	92
W9: S=10cm and T=2 sec	0.08	0.002	2.1	1.5	0.01	96
W12: S=15cm and T=2 sec	0.05	0.01	1.4	1.5	0.01	0.96
W13: S=15cm and T=3 sec	0.05	0.01	1.4	1.5	0.01	0.94

6.1.3 Flume experiment: 2) Lowe 2008

The second flume experiment (Lowe et al., 2008) is about flow through a coral specie (Porites compressa). The λ_p of the coral colony was measured and it has an averaged value of $0.22 \pm 0.02m^{-1}$. Similar as in Lowe et al. (2005b) the friction coefficient C_f , the β -coefficient and the C_M parameter were derived from the PIV measurements. Six unidirectional and three waves experiments (period of 2.13 sec) were tested, where the coral arrangements was varied. For two arrangements the in-canopy flow could be measured and these experiments were modelled with XBeach. In Table 6.2 the parameters of these experiments are shown.

Table 6.2: The derived parameters of the flume experiments. For the unidirectional experiment there is no value of the C_M , because this term can be neglected for unidirectional flow. Therefore, a value of 1 is assumed for these conditions. The flume depth is 0.44 m.

Run	h_c [cm]	k_p [m^2]	β [$1/m$]	C_M [-]	C_f [-]	α [-]
U5:	12.3 ± 0.4	$4x10^{-5}$	19 ± 3	1	0.022 ± 0.002	0.07 ± 0.01
U6:	11.9 ± 0.3	$4x10^{-5}$	27 ± 4	1	0.018 ± 0.002	0.06 ± 0.01
W2:	12.3 ± 0.4	$4x10^{-5}$	4 ± 3	0.8 ± 0.3	0.012 ± 0.003	0.82 ± 0.04
W3:	11.9 ± 0.3	$4x10^{-5}$	6 ± 3	1 ± 0.3	0.016 ± 0.004	0.78 ± 0.04

6.1.4 Results and discussion

The results of the two flume experiments are shown in Figure 6.1. The left panel shows the result of Lowe 2008 and the right panel the results of Lowe 2005. The α was computed from the velocity time series at location $x = 10m$. For the unidirectional test the α_c was computed

and the α_w was computed for the oscillating experiments. The different responds in the in-canopy flow for unidirectional and the oscillating flow is clearly visible as a lower α for unidirectional flow. This shows that the in-canopy model captures the behaviour of both currents and wave induced flow fields. Furthermore, the α is reasonable accurate predicted for all conditions. There is a small bias in the α of -0.04 for the cylinder experiments and 0.08 for the coral experiments.

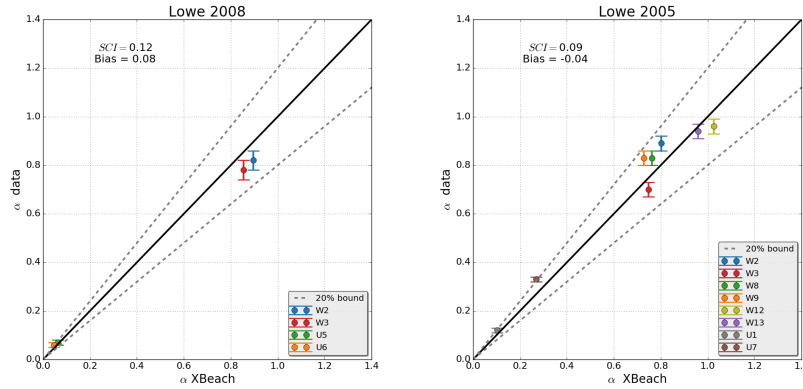


Figure 6.1: The left panel shows the results from the experiment of Lowe in 2008 and the right panel from 2005. In both panels the measured α is plotted against the XBeach results. The dashed line represents the 20% bound. In the left corner the relative bias and the scatter index are given.

A part of the scatter could be caused by the depth-averaged formulation of XBeach. Due to the depth-averaged formulation, the in-canopy model is forced with a depth-averaged velocity and hydrostatic pressure. For shallow water this will not result in an error, but the kh of these experiments ranges from 1 till $1.5rad$. This means that the vertical velocity profile will vary with respect to the depth and that the hydrostatic forcing is not entirely correct. However, there is not a clear relation between the accuracy and the kh of the experiments. The experiments with a longer wave period (W3 and W13) do not give better results. This shows that the depth-averaged formulation of XBeach does not have a large effect on the accuracy.

The assumptions in the choice of the canopy parameters will also introduce a deviation (β , C_M , K_p and C_f). For the experiments of Lowe 2005, the β -coefficient was estimated based on the modified Ergun relation. Equation 5.11 could also be applied, which would give a β -coefficient ranging from 10 to $12.5m^{-1}$ (assuming a C_d of 1), whereas equation 5.10 gives a β -coefficient ranging from 1.4 to $9.4m^{-1}$. Thus, the scatter in the β -coefficient is significant. The sensitivity analyse (Figure 6.2) shows that a 50% deviation in the β -coefficient will result in a 5% deviation of the in-canopy velocity. The same holds for the inertia coefficient, where the uncertainty in the in-canopy velocity is even larger (10%). This shows that there lies

much uncertainty in the canopy parameters.

This could be the reason why, for example, run W12 predicts an α which is larger than 1. This means that the rms-in-canopy velocity is larger than the rms-free stream velocity. Note that this does not necessarily mean that the in-canopy velocity is larger than the free stream velocity, because there is also a background current present in the signal. This is the case for test W12 where the background current is largely damped in the canopy, which gives an in-canopy velocity that is always lower than the free stream velocity.

For the Lowe 2008 experiments all the canopy parameters were measured and assumed to represent the correct values. Only the shear stress coefficient does not entirely represent the measured value due to adapted formulation in XBeach. Assuming that the shear stress does not have much influence, which is a valid assumption for short waves, the scatter is only a result of the assumptions in the in-canopy model. Thus, the skill scores of Lowe 2008 represent the accuracy which can be achieved with the in-canopy model when using the correct parameters. Due to the small number of tests (4) and limited wave conditions, it is hard to give a quantitative validation of the in-canopy model, but these tests suggest that the in-canopy model captures the in-canopy flow through corals.

To show the influence of each term in the canopy model, the different parameters were varied for a progressive wave over a submerged canopy ($a = 0.01\text{ m}$ and $T = 2\text{ sec}$). A vegetation of 0.1 m in a depth of 0.44 m was used for the sensitivity analyse. The four parameters (β , C_f , K_p and C_M) were changed according to the found values in literature (Lowe et al., 2008). Apart from these parameters also the porosity and the wave height were varied. The porosity from three coral species, as described in Reidenbach et al. (2006) were used. The results of these simulations are shown in Figure 6.2. Note that these results are only valid for this particular case of a progressive wave. Unidirectional flow or a different wave period can have a different result.

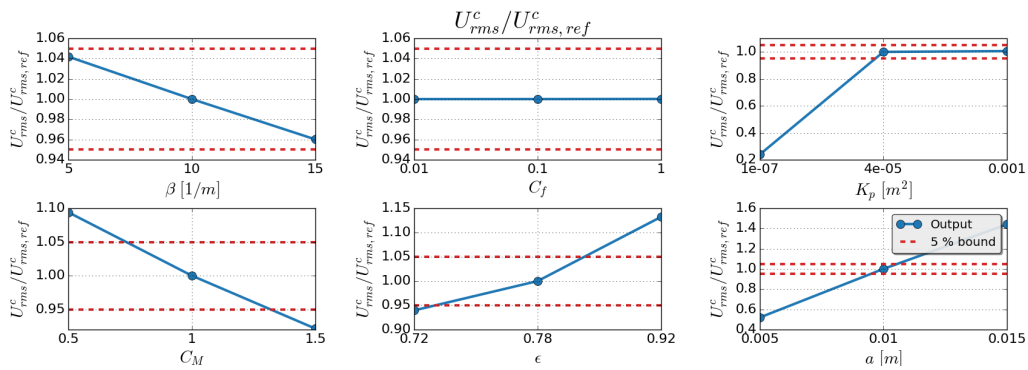


Figure 6.2: Sensitivity analyses where β , C_f , K_p , C_M , p and a were varied. The dashed red line shows the 5% bound of the reference run ($\beta = 10$, $C_f = 0.1$, $K_p = 0.002$, $C_M = 1$, $\epsilon = 0.78$ and wave height of 0.01 m).

The β and C_M parameters have the most impact on the in-canopy velocity, which is expected

for turbulent oscillating flow. Only for very low K_p values the laminar term becomes important, which means that the laminar term can be neglected for flow through a coral canopy. Moreover, it is remarkably that the friction coefficient has zero effect. This could be a result of the relative short waves which were modelled ($kh \approx 0.7$ and $A_\infty^{rms} = 0.005$). This means that the in-canopy flow is inertia dominated and makes the pressure much more important than the shear stress term. Moreover, the in-canopy velocity is not much lower than the depth averaged velocity for this particular test. Thus, the contribution of the shear stress is almost negligible.

A varying β -coefficient will result in a 5% deviation of the in-canopy velocity. This deviation is even larger for the C_M , where a deviation of 10% is found. Thus, without the right parameters an error of about 10% is present in the in-canopy velocity. In general the wave height has the largest contribution to the in-canopy velocity. A 50% larger wave height will result in a 40% larger in-canopy velocity for a progressive wave.

Furthermore, this result shows the influence of the coral colony on the in-canopy velocity. The different porosity found in Reidenbach et al. (2006) show a different responds for in-canopy velocity. Moreover using the modified Ergun relation the β -coefficient would be 15, 9 and 2 m^{-1} for respectively a porosity of 0.71, 0.78 and 0.91. Thus, the in-canopy varies 15% for different corals types. This shows that it is important to compute the in-canopy velocity for corals when the resistance should be determined.

6.2 Validation of the drag force

The experiment of a fringing reef with roughness elements (Buckley et al., 2016) was used to show the effects of the canopy-induced force on the wave hydrodynamics. The same simulation as described in section 4.3 was modeled, but in this section the model results were compared to the rough runs. During these rough runs, cubic elements were placed on the bottom to represent the corals.

6.2.1 Model set-up and calibration

The same model set-up as for the smooth runs was used. Thus, a breaking steepness of 0.8 was applied and the resolution was set to 80 points per wave length. For a good comparison, all the experiments were modelled with three different runs: (1) a run including the in-canopy model to represent the resistance, (2) a run with a calibrated shear stress formulation and (3) a run with an un-calibrated shear stress formulation (reference run).

For the in-canopy model the canopy parameters were determined based on the geometry of the cubes. The λ_p can be computed from the geometry of the cubes. The λ_p is defined as the volume of the cubes divided by the plan area. This results in a λ_p of 0.13 for a cube height of 0.018m and a density of 400m⁻¹. The C_f and the C_M were set to the recommended values which are respectively 0.1 and 1 (see section 5.3). The β -coefficient and K_p were computed with the modified Ergun equations (equation 5.10 and 5.9) which results in a β of 16.5m⁻¹ and a K_p of 0.0001m². The D_{eq} is computed as 6 times the area volume ratio of the roughness cubes. Similar as for the Lowe 2005 experiment, equation 5.11 could be applied, but the modified Ergun relations were preferred as this formulation will also be used in the case of corals. In contrast to the smooth experiments, run 2 was used for the calibration of the Manning coefficient. Experiment 2 is the most representative for all the experiments as the wave height and reef depth are varied with respect to experiment 2. At the region, where the cubes were placed, the friction coefficient was calibrated. For the other locations a Manning coefficient of 0.01s/m^{1/3} was applied. The results of the calibration are shown in appendix D, where it is shown that a Manning coefficient of 0.05s/m^{1/3} gives the best results.

6.2.2 Results and discussion

In Figure 6.3 the bulk wave statistics for the three different runs are shown. This Figure shows the XBeach results plotted against the measurements for the total wave height (H_{rms}), the LF-wave height ($H_{rms,LF}$) and the mean water level ($\bar{\eta}$). The colours indicate the different experiments and the symbols the output locations. The dashed line represents the 20% bounds and the total skill scores of all tests is given in each sub-plot. Before going into details, it can be seen that the roughness elements have a large impact on the LF-waves. These long waves will "feel" the bottom most and without a proper estimation of the resistance the LF-wave height is completely over predicted.

The skill scores of the individual experiments (in-canopy run) are shown in Table 6.3. The cross shore variability of the wave height, LF-wave height and setup are shown in Figure 6.3. The red lines shows the results with the in-canopy model, the dashed grey line shows the results from the reference run and the dotted grey line represents the runs with the calibrated shear stress formulation. The LF-waves are filtered for ingoing (green) and outgoing (orange) waves.

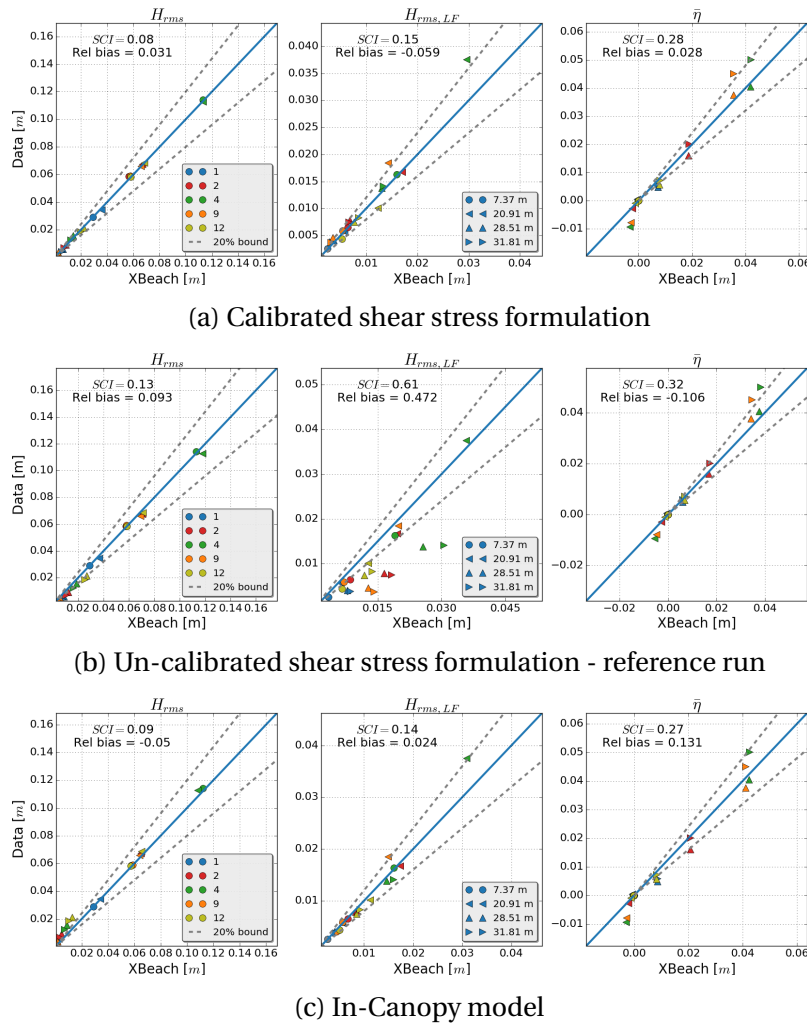


Figure 6.3: XBeach plotted against the data for the three different settings (upper, middle and lower panel). The total wave energy is given in the left panels (H_{rms}), the LF-wave energy in the middle panel ($H_{rms,LF}$) and the setup in the right panel ($\bar{\eta}$). The colors indicate the different experiments and the symbols the locations.

In general the runs with the in-canopy model give very similar results as the measurements. The short waves are slightly under predicted, but the LF-waves are predicted very well. Similar to the smooth experiments, most of the scatter is present in the setup. When considering the absolute deviation in the setup, it can be seen that the error is not larger than $0.005m$. However due to the relative low setup for experiment 1 and 12, this gives a large relative error for these runs.

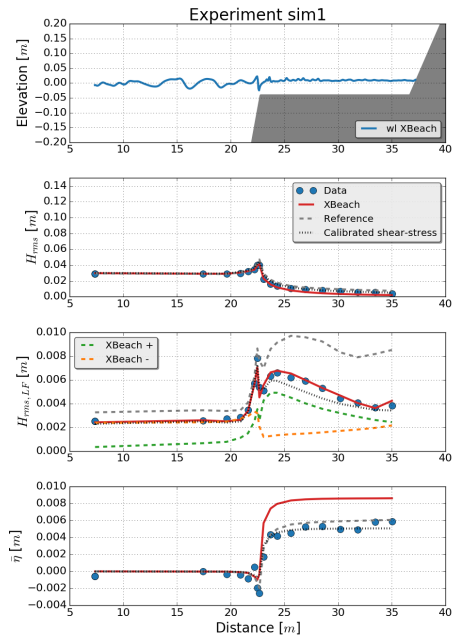
The major problem of this verification is the lack of validation of the in-canopy velocity. The in-canopy velocity can only be implicitly verified by comparing the wave hydrodynamics. This means that only the magnitude of the canopy-induced force can be validated and that nothing can be concluded about the accuracy of the in-canopy velocity. Both the canopy height and porosity are known for these roughness cubes. Thus, only the β -coefficient, friction coefficient and the inertia coefficient had to be estimated. The uncertainty of these parameters will have an effect on the prediction. For example when using equation 5.11 a β of $27m^{-1}$ was found ($C_d = 1$), whereas now a β of $16m^{-1}$ was used. However, the found β -coefficient result in an accurate magnitude of the canopy-induced force, which suggest that the β -coefficient is close to the correct value (assuming that the drag force is the dominant resistance term). To show the effects of these canopy parameters a sensitivity analyse was carried out (see section 6.2.2).

When the runs with the in-canopy model are compared to the runs with the shear stress formulation, it can be seen that there is not a large difference between both formulations. The short waves are slightly better predicted with the shear stress formulation run, whereas the in-canopy runs give a better prediction for the LF-waves. This result gives a contradictory view of the influence of the resistance. It would be expected that for example a larger resistance would reduce both the short waves and the LF waves, but the resistance also affects the generation of LF-waves. This could explain the combination of a lower LF-wave height and a higher short wave height when the calibrated shear stress runs are compared to the in-canopy runs. It has been shown that canopy-induced force is different than the calibrated bed shear stress at the reef crest, which affects the generation of the LF-waves (see section 6.2.2)

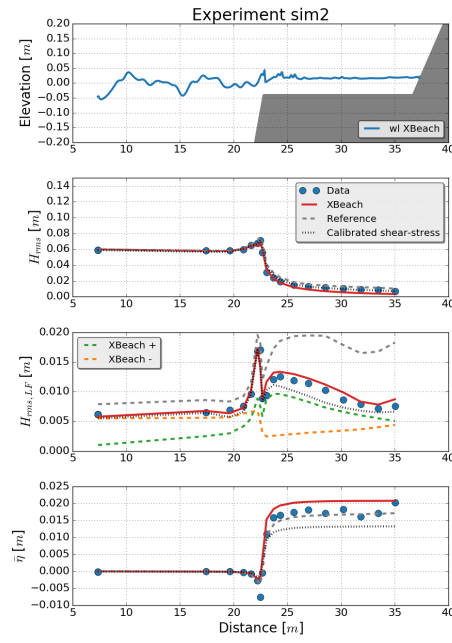
A second difference between the in-canopy model and the calibrated shear stress run, is the higher setup for the in-canopy model runs. The decrease of wave energy at the breaking point is steeper for the in-canopy runs compared to the shear stress formulation runs. Therefore, the setup is always larger predicted with the in-canopy runs. Remarkably, the calibrated shear stress runs gives always a lower setup than the reference shear stress run (with a lower resistance). Thus, the setup is reduced when the bottom friction is increased, but the setup increases compared to the in-canopy run (where the resistance is larger on the reef crest). This means that there is a spatial variability in the canopy-induced force compared to the bed shear stress formulation (see section 6.2.2).

Table 6.3: The errors for the five different experiments.

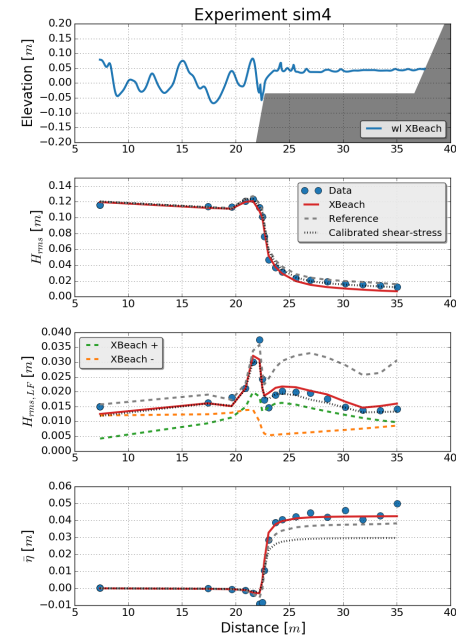
Run	H_{rms}		$H_{rms,LF}$		η	
	SCI	rel. bias	SCI	rel. bias	SCI	rel. bias
sim 1	0.1	-0.061	0.07	0.0	1.16	0.92
sim 2	0.09	-0.048	0.11	0.043	0.34	0.258
sim 4	0.08	-0.037	0.14	0.019	0.19	0.034
sim 9	0.07	-0.032	0.13	-0.01	0.16	0.05
sim 12	0.11	-0.08	0.10	0.068	0.74	0.587



(a) $H_{rms} = 0.03m$



(b) $H_{rms} = 0.06m$



(c) $H_{rms} = 0.09m$

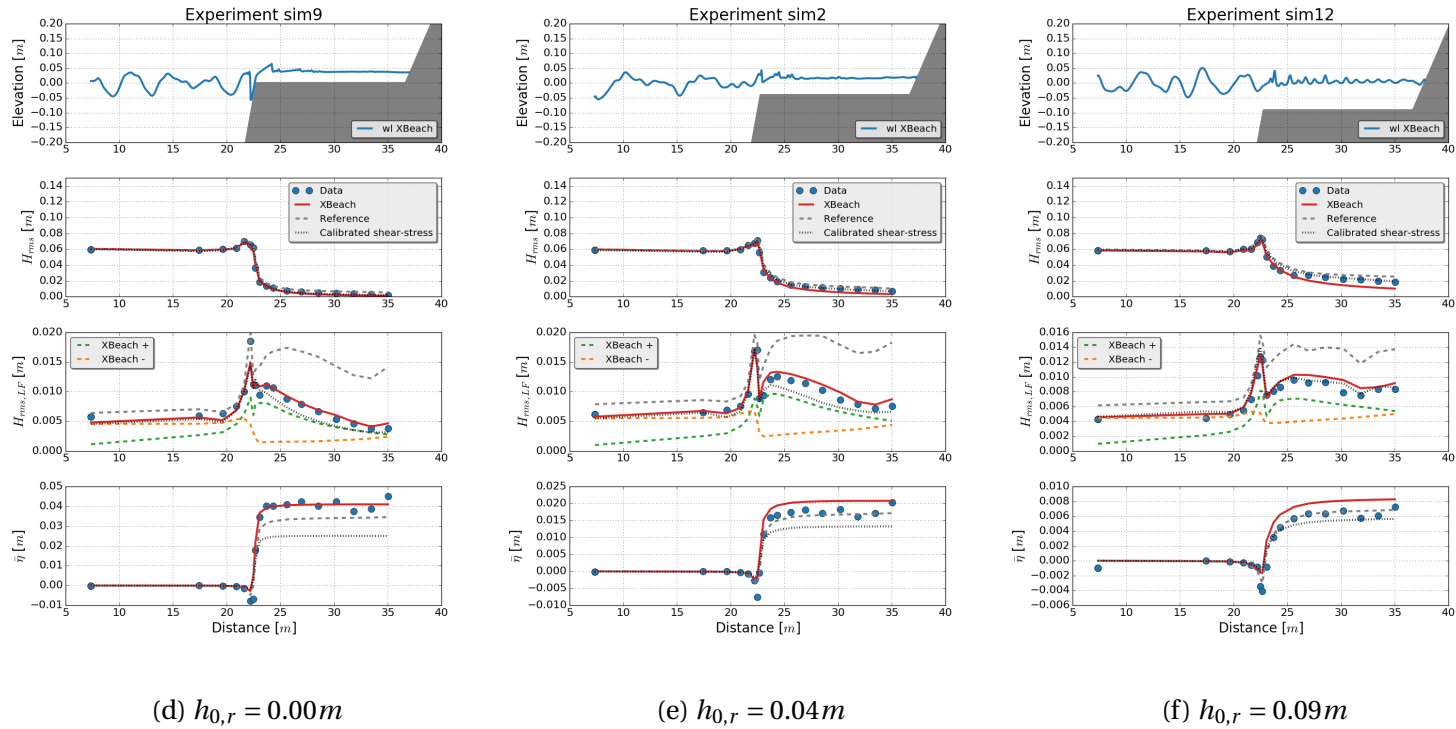


Figure 6.4: The results for run 1, 2, 4, 9 and 12 of the Buckley et al. (2015) experiment. The upper panels show the model set-up, the second panel the rms-wave height, the third panel the low frequency rms-wave height and the last panel the mean water level. The grey dashed lines represents the results of the reference run (without any increased resistance) and the red line the runs with the in-canopy model. In panel three the low frequency waves were filtered for in-going(dashed orange) and outgoing waves (dashed green).

Effect canopy-induced resistance

The resistance will affect both the wave height and the setup. Therefore the mean (related to the setup) and rms (related to the wave height) properties are plotted in Figure 6.5. This figure shows the in-canopy velocity, the depth-averaged velocity and the canopy-induced force for experiment 2. For the other experiments a similar trend is found. The upper panel shows the results of the in-canopy model run and the reference run to get an idea of the effect of the canopy-induced force.

The second panel shows both the in-canopy velocity and the depth averaged velocity. The ratio between these velocities is shown in panel three. It can be seen that this ratio has a spatial variation (both mean and rms-value). This implies that a shear stress formulation times a constant friction coefficient cannot give the same results as the canopy-induced force (apart from the laminar and inertia force). This could be the reason why there is a different behaviour between the calibrated shear stress formulation and the canopy-induced force. However, more importantly is the constrain on the shear stress coefficient (max c_f of 0.1). Due to the dependency of the Manning formula on the water depth, the resistance is enhanced at the wave crest. The water depth can become very shallow at the wave crest due to wave breaking, which causes a large resistance. When the bed shear stress was not limited, it would give a similar result as the canopy-induced force. By computing the bed shear stress from the velocity and water depth signal, a similar value as the canopy-induced was found at the reef crest (both rms and mean value).

In the last panel the canopy-induced force and the calibrated bed shear stress are plotted (both mean and rms). Note that there is also a bed shear stress present in the run with the in-canopy model. This bed shear stress is added to the canopy-induced force for completeness. When both formulations (in-canopy and calibrated bed shear stress) are compared, there is mainly a difference between both formulation at the reef crest (mainly due to the limited bed shear stress).

It can be seen that there is a larger mean resistance (onshore directed) at the reef crest. Thus, apart from the steeper radiation stress gradient, the setup is also enhanced due to this larger canopy-induced force. This force is compensated by a water level gradient at the reef crest, which will result in a water level elevation on the reef flat. Furthermore, these results suggest that the larger resistance at the reef crest leads to the generation of higher LF-waves. The resistance on the reef-flat is comparable between both formulations, which indicates that there is difference between the generation of the LF-waves of both runs.

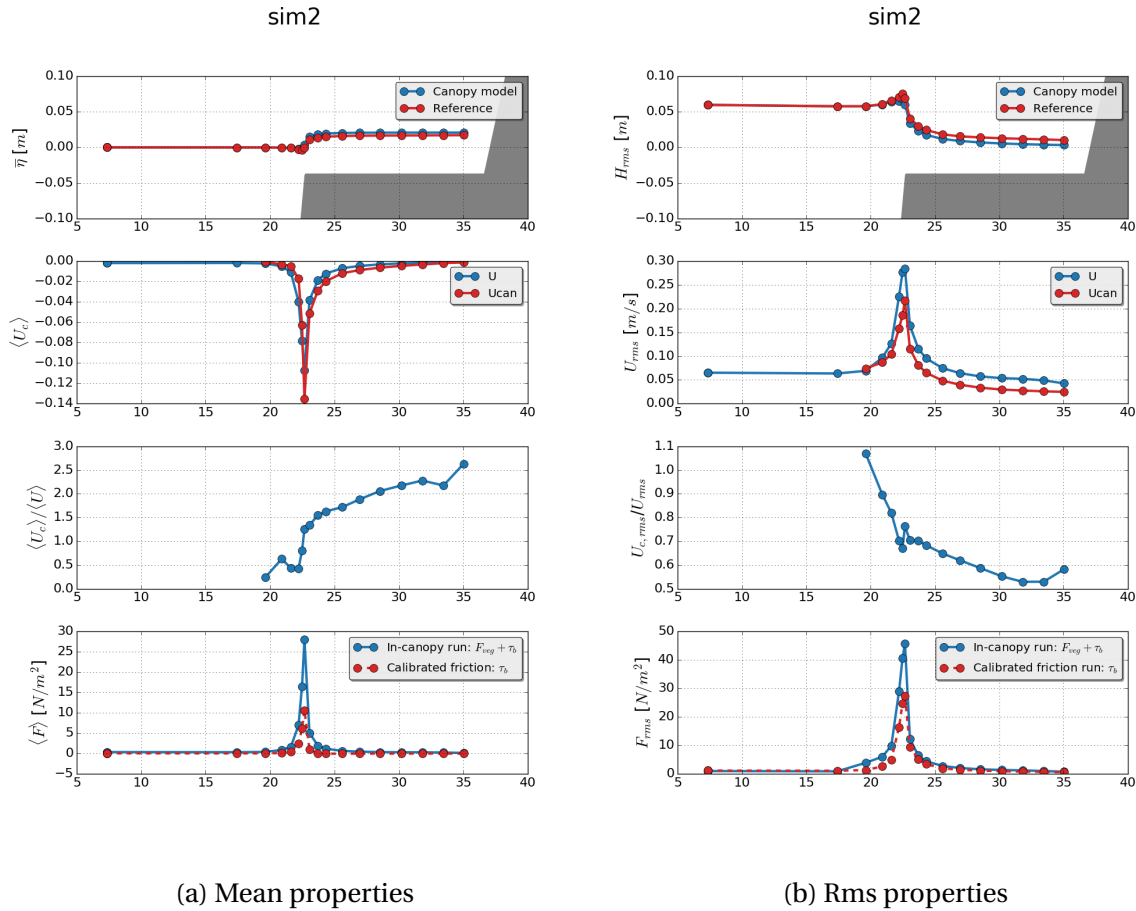


Figure 6.5: The results of the in-canopy model for test 2. The upper panel shows the setup (left) and the wave height (right). The second panel the mean velocities (left) and the rms velocities (right). The ratio of both velocity is given in panel three. The last panel shows the mean vegetation force (left), the mean bed shear stress (run with shear stress formulation)(left), the rms vegetation force (right) and the rms bed shear stress (right). Note that the vegetation starts after $x = 15m$, which means that the in-canopy velocity is zero before $x = 15m$.

Sensitivity of the canopy-parameters

The β , C_M and C_f were varied to show the sensitivity of the canopy parameters on the hydrodynamics. Experiment 2 was used to analyse the sensitivity. These results are shown in Table 6.4. Furthermore Figure 6.6 gives an estimation of the cross shore variability of the different terms. It is an estimation, because the individual canopy terms were not given as outputs of the model, but were computed from the other output variables (U , U_c , $\frac{\partial \eta}{\partial x}$). For example, the inertia force which is dependent on the gradient in the velocity, will not be exactly correct

represented in this figure. This figure gives a general view of the order of magnitudes of the different terms.

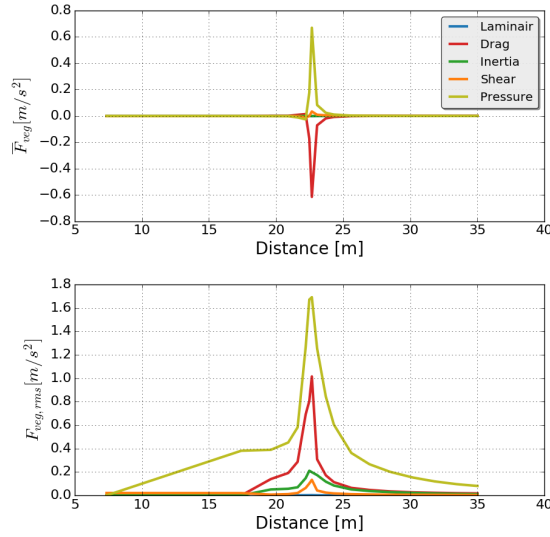


Figure 6.6: Mean and rms value of the different terms in the in-canopy model for the Buckley test 2. The different terms were computed from the output variables U , U_c and $\frac{\partial \eta}{\partial x}$ with a point output of 0.01s.

It can be seen that a smaller β would give a better result for the short waves, but does not improve the LF-waves. It seems that the most optimum value lies between 10 and $16.5 m^{-1}$. This does not necessarily mean that the β -coefficient is too large, but it shows that the magnitude of the canopy-induced force is predicted too large. Figure 6.6 shows that the drag force has the largest contribution on the total canopy-induced force. Thus, when a lower β gives a better result, it can be concluded that the magnitude of the resistance is predicted too large.

The C_M had less influence on the hydrodynamics than the β -coefficient. A varying C_M does not change the skill scores significantly. Thus, the resistance is mainly determined by the drag force, which is also shown in Figure 6.6. It is also remarkable that increasing the resistance does not show a negative bias for the LF-waves (under-prediction). Apparently, the larger resistance results in the generation of larger LF-waves, which also lead to an over-prediction of the LF-waves.

Furthermore, this sensitivity analysis shows that the flow is not completely inertia dominated. The shear stress does also have a contribution. A lower friction coefficient results in an increased skill score. This could be a result of the dominance of the LF-waves on the reef. For these long waves the shear stress can become more dominant compared to the pressure gradient.

At last the sensitivity shows that the estimated canopy parameters were not far from to the optimum values. None of the varied canopy parameters gave a better result. However, due to lack of validation of the in-canopy velocity, it cannot be concluded that the correct parameters were used. For example, a larger β and a lower C_M could give the same canopy-induced force. On the other hand these results suggest that the recommended parameters and formulations are applicable.

Table 6.4: The skill scores for different canopy parameters for test 2.

β	H_{rms}		$H_{rms,LF}$		$\bar{\eta}$	
	SCI	Bias	SCI	Bias	SCI	Bias
10	0.07	-0.018	0.17	0.08	0.31	0.24
16.5	0.09	-0.048	0.11	0.04	0.34	0.26
20	0.09	-0.054	0.21	0.12	0.28	0.21
C_M	H_{rms}		$H_{rms,LF}$		$\bar{\eta}$	
	SCI	Bias	SCI	Bias	SCI	Bias
0.5	0.09	-0.053	0.23	0.14	0.28	0.21
1	0.09	-0.048	0.11	0.04	0.34	0.26
1.5	0.08	-0.027	0.16	0.08	0.32	0.24
C_f	H_{rms}		$H_{rms,LF}$		$\bar{\eta}$	
	SCI	Bias	SCI	Bias	SCI	Bias
0.01	0.09	-0.038	0.24	0.15	0.3	0.23
0.1	0.09	-0.048	0.11	0.04	0.34	0.26

6.3 Conclusion

Both the validation of the in-canopy velocity and the effect on the hydrodynamics are shown in this chapter.

The in-canopy model was used to predict the in-canopy velocity for two lab experiments. Both experiments were predicted reasonable accurate. A relative bias of 0.08 (SCI=0.12) was found for flow through coral species and a relative bias of -0.04 (SCI=0.09) was found for flow through rigid cylinders. Moreover, both the responds of the unidirectional and the oscillating runs were predicted according the data, which shows that the in-canopy captures the behaviour for different flow fields.

The in-canopy model captures both unidirectional and the oscillating flow fields accurately.

The sensitivity analyses showed that the canopy parameter affects the in-canopy velocity by 10% for a short progressive wave. Furthermore, it shows that the in-canopy velocity can be significant different for varying coral colonies, which implies that the in-canopy model is necessary to distinguish between the in-canopy flow for different coral types.

The results of the Buckley test showed the influence of the roughness elements. Without a proper resistance force, the LF-wave height was extremely over predicted. Thus, first of all it can be concluded that a correct representation of the resistance is important.

When the results are compared to the measurements, it can be concluded that the in-canopy model captures the canopy-induced force accurately. The short waves were predicted with a relative bias of -0.05 and a scatter index of 0.09. Almost the same accuracy was found when the LF-waves were compared to the measurements (relative bias of 0.024 and scatter index of 0.14). Most of the scatter was present in the setup, but still XBeach gives a reasonable prediction (relative bias of 0.13 and scatter index of 0.27).

Compared to the calibrated shear stress runs, it can be concluded that the un-calibrated in-canopy runs gives a similar result. By applying the geometry based canopy parameters, it is possible to predict the resistance with the in-canopy model and accurately model the reef-hydrodynamics.

An un-calibrated in-canopy model based on porosity and canopy height gives a competitive result compared to a calibrated shear stress formulation for reef-hydrodynamics.

Moreover, it has been shown that there is mainly a difference between the canopy-induced force and bed shear stress at the reef crest. This means that the difference in the LF-waves and the setup (on the reef flat) between the in-canopy run and calibrated shear stress runs, is a result of a different resistance at the reef crest. Thus, it is important to capture the resistance at the reef crest as it has a large influence on the LF-waves and setup over the reef flat.

Considering the different terms it was shown that drag force has the largest contribution on

the resistance, but a varying C_M the most influence on the result. Furthermore, the flow is not completely inertia dominated and that the shear stress also has a contribution (apart from the pressure).

7

Validation: Ningaloo Reef

This chapter shows the result of a 5 day swell simulation at Ningaloo Reef. Section 7.2 describes how the wave statistics were derived from the measurements. The model set-up is given in section 7.3 and the results are shown in section 7.4. Finally, the conclusion are given in section 7.5.

7.1 Introduction

A three week data campaign at Ningaloo Reef (June 2009) was used as field validation test. Due to the steep fore reef (1 : 20) and the coral covered reef flat, this site is a good validation for XBeach-nh+ with addition of the porous in-canopy model. Moreover, this field application requires a 2-dimensional approach. Therefore, the application of the in-canopy model is shown in 2-dimensions.

7.2 Data Analysis

During the field campaign 10 measurement instruments were deployed for three weeks. The location of the instruments including the measured bathymetry is shown in Figure 7.1. Instrument C2 was collocated with C1 as backup and it is not used within this study. At location C1 the sea surface elevation was measured instead of the pressure for the other locations. From the concave hull (blue dashed line) of the measured bathymetry can be seen that the beach is not everywhere included in survey. Therefore, a constant sloping beach of 1 : 10 is set in the domain.

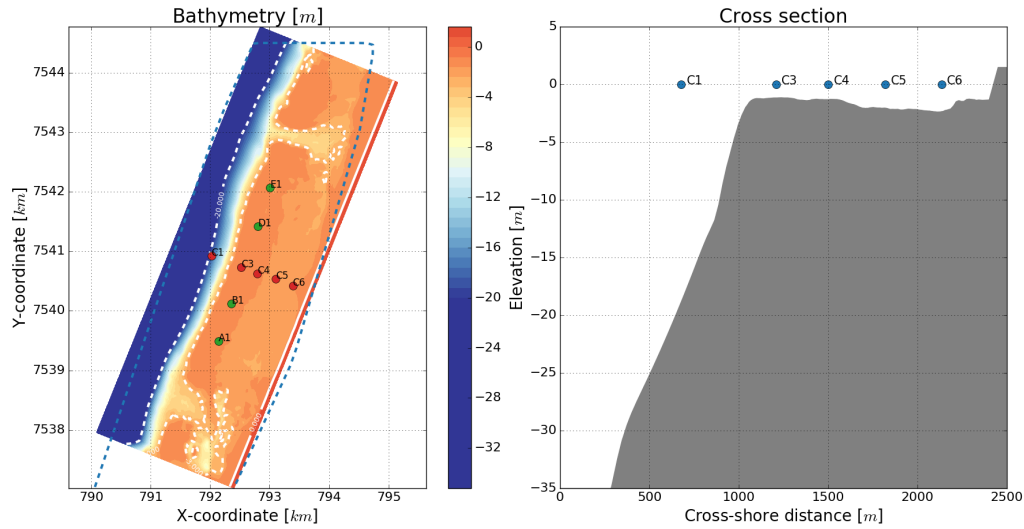


Figure 7.1: The bathymetry and location of the instrument at Ningaloo Reef. This is shown for both a map view and a cross section. The blue dashed line shows the concave hull of the bathymetry survey.

From both the sea surface elevation signal and the pressure signal, an energy density spectrum was computed for every hour. Based on this energy density spectrum the T_p , $H_{rms,LF}$ (30 – 300s) and H_{rms} (5 – 30s) were determined. The wave direction as given in Van Dongeren et al. (2013) was used. The tidal signal is obtained from the (hourly) mean water level at location C1. For the other locations the mean water level cannot directly be obtained, because the setup is included in the measured signal. It was not possible to relate the measured signals to mean sea level, because the bed level is not exactly known at the measurement locations. Therefore, the mean water level signal was corrected with an offset level to obtain the water level relative to mean sea level. To determine this offset level, the water level signal was demeaned to obtain a zero centred signal. The mean water level at location C1 was subtracted from these zero centred signals to obtain a measure of the setup. Then, this water level difference was plotted against the wave power ($H_s T_p^2$) for every hour. A linear line was fitted through these points and the offset was derived from the value at zero wave power similar as described in Van Dongeren et al. (2013). This value was subtracted from the water level signal to obtain the signal relative to mean sea level.

The time series of the offshore wave height (H_s), peak period (T_p), direction and mean water level is shown in Figure 7.2. The wave height time series at the other locations of the cross section are plotted as dashed lines in the upper panel, which shows the large reduction of wave height at the reef crest. Some scatter is present in the peak period due to two peaks in the spectrum (swell event and wind-waves). The energy density spectrum for location C1 is shown in Figure 7.3, where the different swell events are visible. However, the wind-wave

CHAPTER 7. VALIDATION: NINGALOO REEF

peak is almost absent for the modelled periods, which gives a more constant peak period. The two modelled periods are shown as red (calibration) and green (validation) vertical lines. The validation and calibration were based on the measurements at locations C1-5 and A1. The other location did have invalid or a lot of missing measurements and therefore these locations were not used in this study.

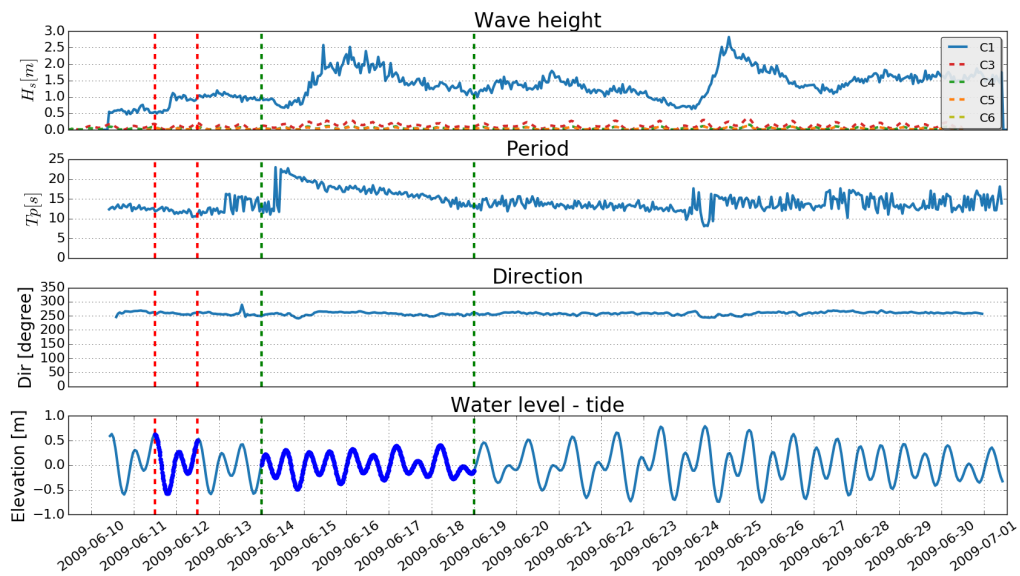


Figure 7.2: The measured data at Ningaloo reef. The upper panel shows the swell waves for a transect (C1, C3, C4, C5 and C6). The second panel shows the peak period for location C1. The third panel shows the direction of the waves (C1), where zero corresponds with waves coming from the North. The last panel shows the tidal signal relative to mean sea level. The red lines represent the calibration period and the green lines the validation period.

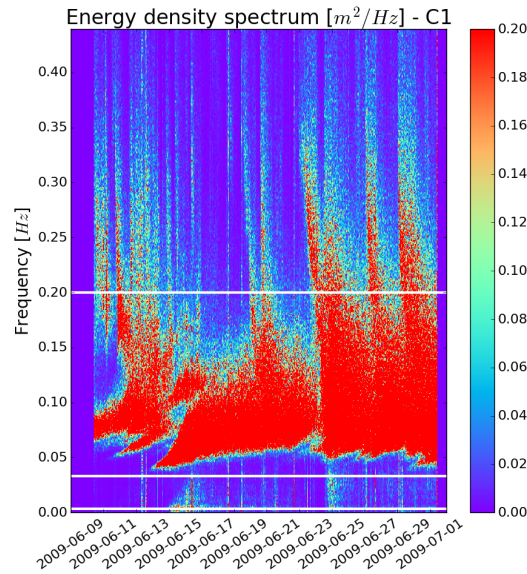


Figure 7.3: The measured energy density spectrum for location C1. The white lines represents the bounds of the frequency which is used to determine the LF-waves and the short waves.

7.3 Model setup

The model is discretised with a 2-dimensional grid. For the cross shore direction a spatial varying grid was used to optimize the performance. The grid resolution was based on 40 points per wave length (For a period of 12s). This resolution is lower than used for the Buckley experiments, but based on the computational effort a lower resolution was preferred. The analyse of the grid resolution for the Buckley experiment showed that 40 point per wave length gave already a reasonable results (appendix B.2). Only the setup and the LF waves were slightly under predicted when using 40 points per wave length. Moreover, due to the varying wave period in the simulation, the resolution is finer for the higher waves where the wave period is much larger. In the y-direction a resolution of 10m was applied. This is a very rough resolution, but it is assumed that the waves on the reef are mostly shore-normal directed. Due to the steep fore reef, refraction is enhanced at the fore reef, which suggest that the waves are shore-normal directed on the reef flat. Furthermore, the alongshore distance was reduced to 3.5km for efficiency reasons. This means that both channels were not included in the domain, which will affect the setup due to the missing return current through these channels (Wyatt et al., 2010a). The influence of both the y-resolution and neglecting the channels is shown in appendix E. These results did not show a large effect on the accuracy for both assumptions. The final domain is shown in Figure 7.4.

At both lateral boundaries cyclic boundary conditions were applied. This means that the

waves which leave the upper boundary will enter at the lower boundary and vice versa. Without these cyclic boundaries, artificial flow and setup arise near the boundary. Cyclic boundary conditions can only be used for uniform coasts, which is not entirely the case here. Therefore, the bed level at both lateral boundaries was interpolated to each other to minimize reflections. Furthermore, the bed level was given a maximum depth of 35m in order to have a kh less than 4 for most of the super-harmonics. The super-harmonics of the shortest forced waves (12s) have a relative depth of 3.9 with a maximum water depth of 35 m. Thus, a majority of the super-harmonics will have a kh which is much lower than 4, which would imply that these super-harmonics can also be forced at the boundary.

The model was forced with an hourly varying JONSWAP spectrum. Combining the wave steepness (≈ 0.001) and the relative depth (≈ 2), approximately $\pm 10\%$ of the wave energy is present in the super-harmonics and $\pm 5\%$ in the sub-harmonics (see figure 3.7). To avoid spurious waves with these energies, both the super and sub-harmonics were included in the boundary signal. In Van Dongeren et al. (2013) it was shown that the directional spreading is almost constant at 20 and, therefore, a constant directional spreading of 20 was applied. The tidal water level was set every 15 minutes to get a smooth tidal signal. Polynomial interpolation was used to obtain the 15 minute tide signal from the hourly signal.

The validation period was modelled twice with a run including the in-canopy model and a run with the calibrated shear stress formulation. For the calibrated shear stress run, the friction coefficient was calibrated and the canopy parameters, necessary for the in-canopy runs, were based on the found corals properties at Ningaloo Reef. A spatially varying canopy or friction coefficient was used to represent the corals.

The friction coefficient was calibrated for the runs with the calibrated shear stress formulation. The breaking steepness was set to the default value of 0.4. It was not possible to accurately model the large drop of wave energy at the reef crest when varying only the breaker steepness. It could be possible that a large part of the wave energy is dissipated by the coral roughness. Furthermore, the location of the breaking point does not change much when varying the breaker steepness (see results the results of the Buckley test). Therefore, it is chosen to use the default breaker steepness. At the locations of the corals (Figure 7.4) the Manning coefficient was calibrated. When the different friction coefficients are compared, a manning of $0.15s/m^{1/3}$ gives the best results considering the short waves (Table 7.1).

Table 7.1: The results of the calibration for Ningaloo reef.

n	H_{rms}		$H_{rms,LF}$		$\bar{\eta}$	
	SCI	Rel. bias	SCI	Rel. bias	SCI	Rel. bias
0.01	0.55	0.339	2.23	2.06	0.93	0.339
0.05	0.58	0.341	0.90	0.71	0.19	0.341
0.1	0.46	0.207	0.35	-0.09	0.01	0.207
0.15	0.43	0.165	0.39	-0.21	-0.21	0.165
0.2	0.42	0.168	0.39	-0.21	-0.21	0.168

7.3.1 In-canopy model

To include the coral canopy in the model two different coral categories were used. It was found that there is a distinguish coral canopy between the reef crest and the reef flat (Wyatt et al., 2010b; Taebi et al., 2011). On the reef flat the bottom was completely covered with tabulate *Acropora* spp. Based on the available underwater photos (Cassata and Collins, 2008) and the geometrical parameters given in Lowe et al. (2005b), the canopy height was set to $0.3m$ and the porosity to 0.8.

There mainly live encrusting coralline algae at the reef crest (due to the large wave impact) and the dominant live in deeper water is the *Acropora* spp. in combination with sponges and sea whips (Cassata and Collins, 2008). Due to the different corals and the limit knowledge about corals in this zone, it is much harder too estimate the canopy parameters. However, it is known that the canopy height must be lower than at the reef flat, due to the wave attack. Thus, a canopy height of $0.2m$ is assumed with a porosity of 0.9.

The back reef/lagoon consists of large sand patches including some branching staghorns (Cassata and Collins, 2008). Due to the limited corals on the lagoon, the in-canopy model was not used in the lagoon.

The canopy on the reef crest is located from a depth of $-15m$ till the reef crest. The canopy on the reef flat is located from the reef crest till a depth of $-1.5m$. These zones are shown in Figure 7.4. In Table 7.2 the properties of these categories are given. The β was determined with equation 5.10 based on the given porosity (D_{eq} was set at 1.5 times the average branch diameter $0.02m$ (Lowe et al., 2008)).

CHAPTER 7. VALIDATION: NINGALOO REEF

Table 7.2: Coral species at Ningaloo reef. The picture of the reef flat is taken at Ningaloo Reef, but the picture of the reef crest is only shown as impression. Source reef flat: Wyatt et al. (2010a). Source reef crest: Credit Rogersjs CC BY-SA 4.0.

Category	Major coral species	β (m^{-1})	ϵ	h_c [m]	C_M	K_p	C_f
Reef flat	Tabulate Acropora spp.	25	0.80	0.3	1	0.0001	0.1
Reef crest	Encrusting coralline algae	10	0.90	0.2	1	0.0001	0.1

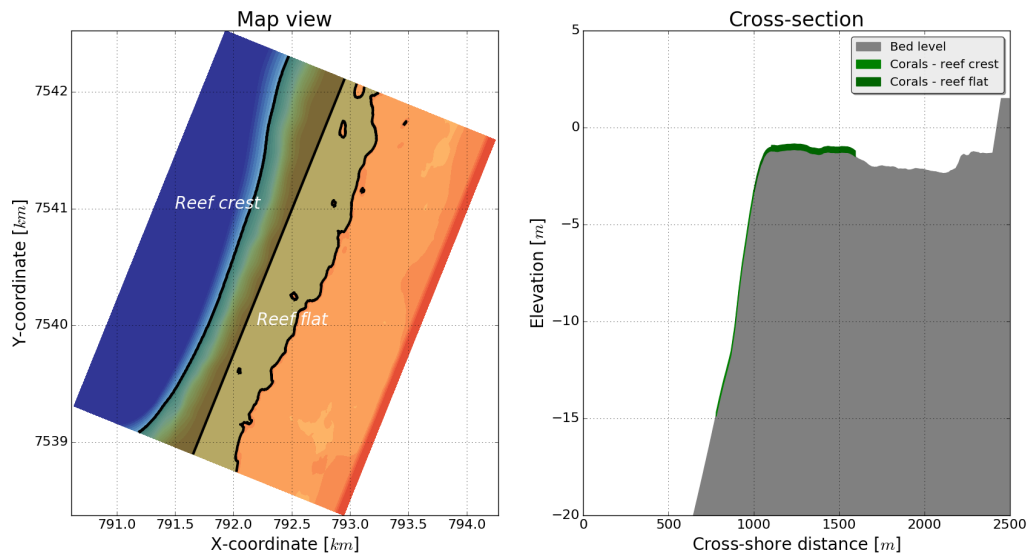
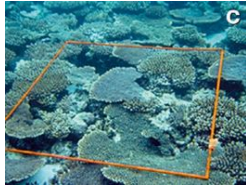
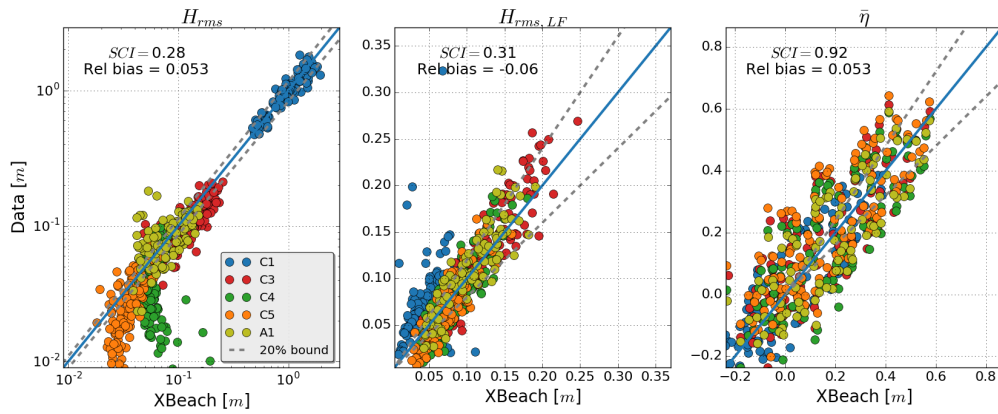


Figure 7.4: Map view of the canopy vegetation.

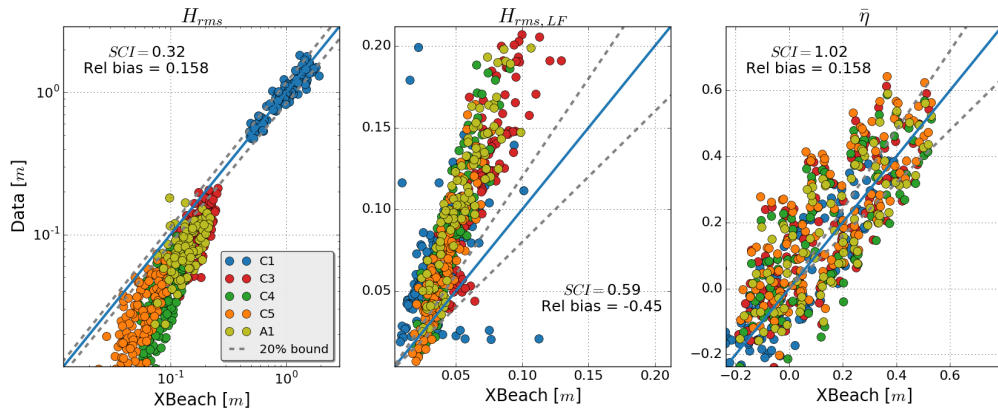
7.4 Results and discussion

An overview of the results for the 5 day swell event is shown Figure 7.5, where both the results with the calibrated shear stress formulation and the in-canopy model are shown. Note that a logarithmic scale is used for the short waves, because of the large differences in wave heights (5 cm lagoon and 1 m offshore).

When the two runs (shear stress formulation and in-canopy model) are compared, a deviation in both the short waves and LF-waves is visible. When considering the shear stress formulation, the short waves on the reef flat are over-predicted, but the LF-waves are under-predicted. The run with the in-canopy model gives a better result for the hydrodynamics. This could be the result of the spatial varying coral canopy in the domain (reef flat and reef crest) or due to a wrongly calibrated shear stress coefficient. It could be possible that the found bed shear stress is only applicable for the shorter waves during the calibration period, but does not represent the resistance of the larger waves at the swell event.



(a) Canopy model



(b) Shear stress formulation

Figure 7.5: XBeach results plotted against the measurements for the short wave height (H_{rms}), LF-wave height ($H_{rms,LF}$) and setup ($\bar{\eta}$).

In this section the results for the run with the in-canopy model are shown. The same figures for the calibrated friction formulation can be found in appendix E.2. In Figure 7.6 the time series of the short and LF-wave heights are plotted. This figures show the time series for five different locations. Note that the measurements of location A1 did not contain values for the whole period.

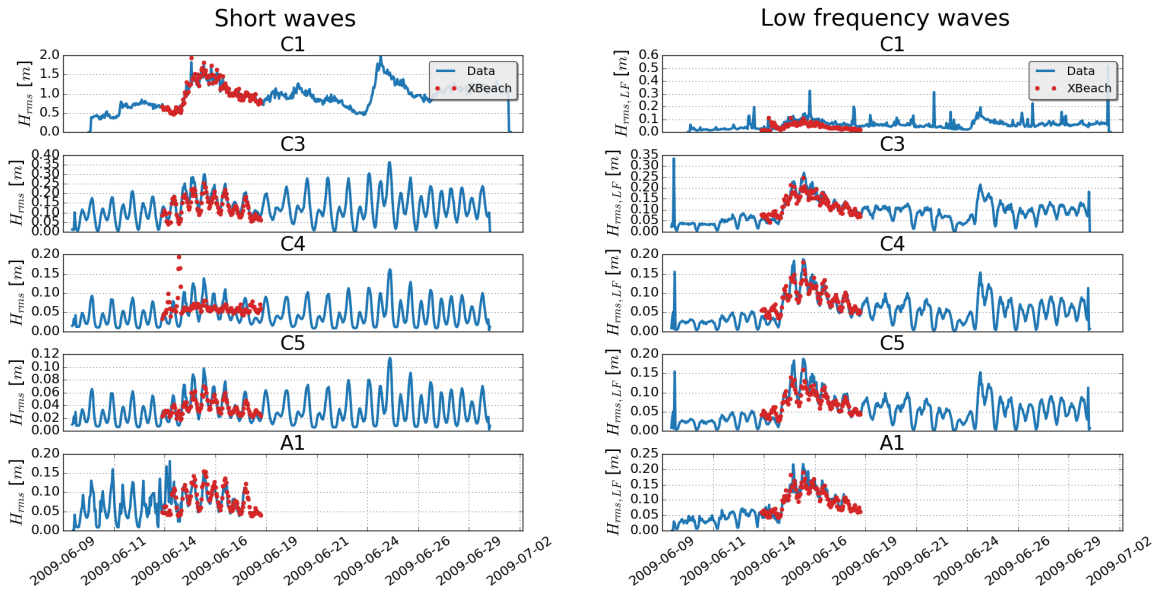


Figure 7.6: The time series of the XBeach results compared to the measurements. The left panel shows the short wave heights (H_{rms}) and the right panel the low frequency waves ($H_{LF,rms}$).

The short waves are reasonably accurately modelled when the results are compared to the measurements. The waves at location C1 were forced at the boundary, which means that location C1 is not representative for the accuracy of the model. The other locations show that both the dissipation of energy at the reef crest and the tidal modulation is captured. It can be seen that there is a deviation for location C4 and C5, where the waves are under-predicted ($\approx 5\text{cm}$). This is probably a result of too much damping on the reef flat (canopy-induced force is too large). Furthermore, there are a few moments where the wave energy is highly overestimated at location C4. This is a result of the transition between the region where the in-canopy model is applied and the region without the in-canopy model (location C4 lies just before this transition). Apparently the transition from the large canopy-induced force to no canopy-induced force generates artificial waves for these moments. Due to the shallow water depth at these moments (low setup and low tide), the canopy-induced force has a large effect on the flow computation during these moments. It is thus important to have a smooth transition between the different types of vegetation/corals to prevent these artificial waves for very shallow water conditions.

The default breaking parameter was applied, which could result in a wrongly modelled breaker zone. However, the results of the Buckley test suggest that the breaker zone is not much affected by the breaking steepness. Assuming that the dissipation by wave breaking is correct, it can be concluded that a significant part of the wave energy at the reef flat is dissipated by the canopy-induced force. Without the canopy-induced force both the short and LF-waves are over-predicted at the reef.

Considering the LF-waves, there is mainly a deviation for location C1. This could be caused by two reasons. Firstly, only the LF-waves generated by the wave interaction were forced at the boundary, but in reality there will also be other (free) LF-waves at the offshore boundary. Secondly, the generation of LF-waves is not modelled correctly. The LF-waves at location C1 are mainly generated at the reef crest (break point forcing), as the amplitude is too large for an incoming bound long waves. Furthermore, the results of the Buckley test showed that the generation of the LF-waves is highly depended on the resistance at the reef crest. Due to the rough estimations of the canopy parameters, it is possible that the resistance on the reef crest is not entirely correct. Although the deviation at location C1, the general trend of the LF-waves is captured. Both the tidal modulation and the increased wave height during the swell event were accurately modelled.

The setup contains most of the scatter. However, it is difficult to compare the setup with the measurements, because there is also a large uncertainty in the measurements. When considering the time series of the setup (Figure 7.7) the general trend is well represented. There is not a large bias (0.053), which shows that the model does not gives a wrongly behaviour. Furthermore, neglecting the channels could have an impact on the result, but it seems that the uncertainty of the data is larger than the error caused by neglecting the channels when the results of different domain size were compared (appendix E).

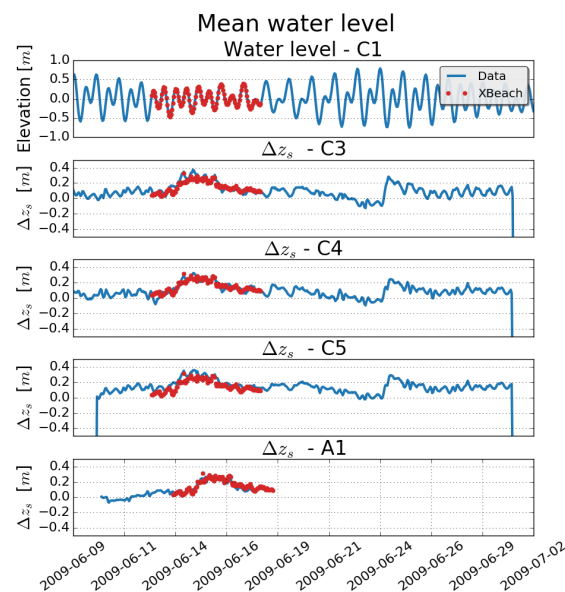


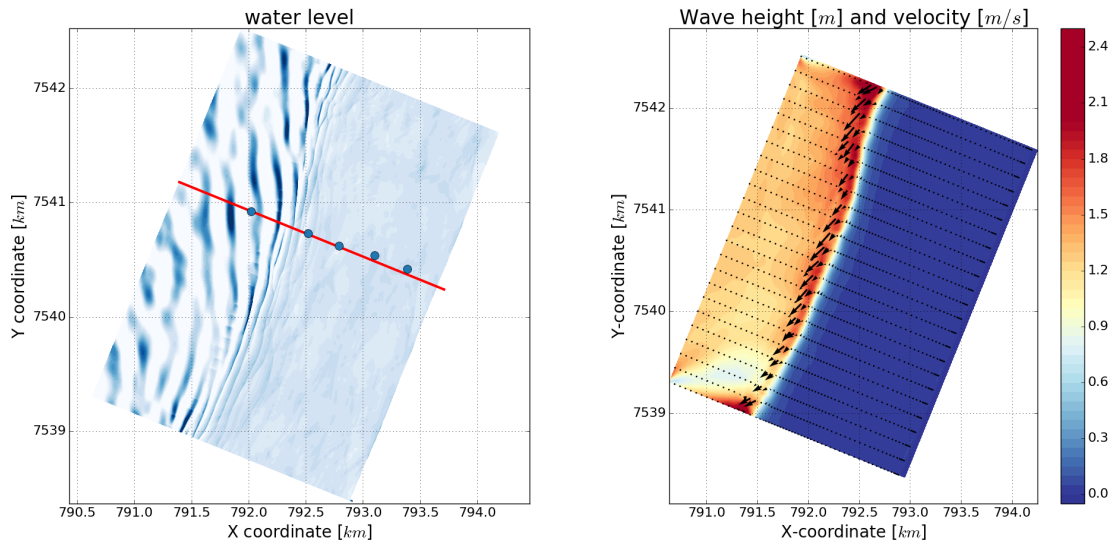
Figure 7.7: The time series of the XBeach results and the measurements of the mean water level (C1) and the setup (C-3-5)

For two moments in time the cross shore variability of the short waves, LF-waves and the setup is shown in Figure 7.8. The upper sub-figure shows the map-view of the domain with the location of the cross section and the measured locations. The lower sub-figure shows the

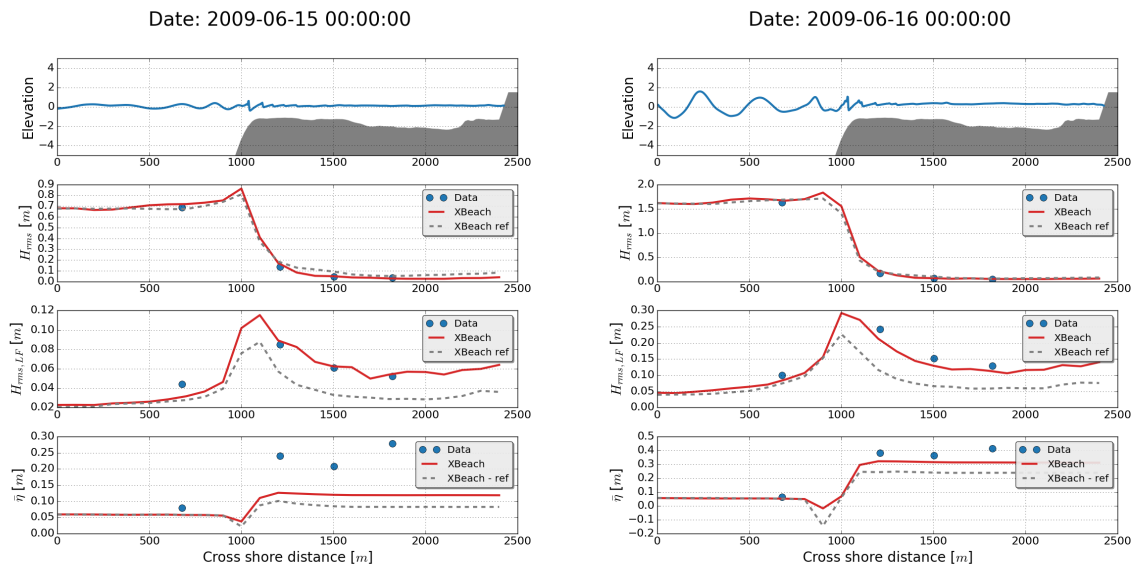
H_{rms} (second panel), $H_{rms,LF}$ (third panel) and the $\bar{\eta}$ (third panel). The red line represents the in-canopy run and the dashed gray line the result of the calibrated shear stress run.

Considering the spatial variability of the wave height, two remarkable results are visible. Firstly, there is a shadow zone in the wave height, caused by the waves coming from the south-west corner. Thus, the forcing in the lower south-west corner is not correct. This will not have a large effect on the results, as the validation locations are not affected by this shadow zone. Secondly, there is a very large long-shore current in front of the breaker zone. It is not entirely known why there is such a large current in front of the reef. This could be caused by the rapid increase of the wave height due to shoaling on the steep fore reef. This increase in radiation stress ($S_{xy} = nE$) could result in a long-shore current in the opposite direction of the long-shore wave component ($\frac{\partial nE}{\partial x} = \tau_y$).

The results of the cross section show that the general behaviour is consistent with the measurement. The waves break at the reef crest, where most of the LF-waves are generated. These LF-waves are damped on the reef flat by the coral resistance. Moreover, the breaking waves cause a water level gradient at the reef crest, which result in a setup on the reef flat. Moreover, both the mild and energetic wave condition shows a similar trend as the measurements.



(a) Map view



(b) Cross section

Figure 7.8: The first sub-figure shows an instantaneous water level and the H_{rms} and the velocity (2009-06-16 00:00). The second sub-figure shows the results for the red cross section. The upper panel shows the water level, the second panel the significant wave height, the third panel the significant LF-wave height and the last panel the mean water level. The dashed grey lines represent the result of the calibrated shear stress formulation.

Furthermore, the difference between the in-canopy run and calibrated shear stress run is clearly visible in this figure. For both moments the short waves on the reef flat are less damped when using the calibrated shear stress formulation and secondly the generation of the LF-waves is lower for calibrated shear stress run. To show the difference in resistance between both runs, the resistance of the in-canopy run (F_{veg}) and the calibrated shear stress formulation (τ_b) is shown in Figure 7.9. In this figure the mean and rms values of the resistance are plotted for a cross section. The effect of the two coral types (reef flat and reef crest) are visible as a step in the rms canopy induced force ($x = 1200$). Both on the reef crest and the reef flat the rms-resistance is much larger when using the in-canopy model compared to the bed shear stress. This explains the different results between the in-canopy run and the calibrated shear stress run. Due to the larger canopy-induced force the short waves are more damped with the in-canopy run. There is also a different response in the mean resistance. On the fore shore both runs give an offshore directed resistance, which means that the mean squared velocity is positive (onshore directed). Thus, these waves are much skewed, due to shoaling, which result in a positive mean squared velocity. After the waves break they become more linear and the mean squared velocity is negative (offshore directed), which result in a positive mean resistance. Comparing the canopy model and the calibrated shear stress run, there is mainly a difference at the reef flat, where the mean canopy-induced force is onshore directed and the bed shear stress offshore directed. It is not known what causes this difference, but it could be a result of the larger resistance at the reef flat with the in-canopy model run.

The hydrodynamic results showed that the resistance on the reef flat is too large. This means that the canopy parameters on the reef flat are not completely correct. It is known that the coral density decreases land-wards (Cassata and Collins, 2008), whereas there is a complete covering assumed for the entire reef flat. This will result in a too much damping at the end of the reef flat. Apart from the density, the β -coefficient could be estimated too large. The used value of $25m^{-1}$ is a relative large value compared to the parameter space described in section 5.3. Thus, the uncertainty in the canopy parameters and the locations of the corals will affect the results. However, the general trend is very similar to the measurements. Using a rough estimation of the canopy parameters a reasonable result for the hydrodynamics is predicated.

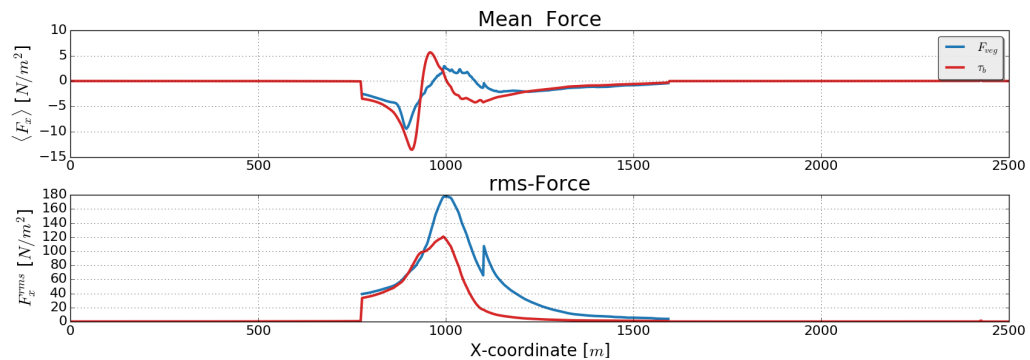


Figure 7.9: The mean (upper panel) and rms values (lower panel) of the F_{veg} and τ_b of respectively the in-canopy runs and the calibrated shear stress run. This cross section located at the same location at the result of Figure 7.8 and computed at 2009-06-16 00:00.

7.5 Conclusion

By modelling the 5 day swell event at Ningaloo reef, the application of both XBeach-nh+ and the in-canopy model was shown in 2D. Although a lot of uncertainty is present in the canopy parameters, the model gives a reasonable prediction of the hydrodynamics. The general trend of the short waves, LF-waves and the setup is captured. Both the tidal modulation (short and LF-waves) and the increased wave height during the swell event for the LF-waves was accurately modelled. There was only a deviation for the short waves at the end of the reef flat, due to a too large canopy-induced force.

A reasonable accurate prediction of the reef hydrodynamics were obtained by using the in-canopy model to estimate the resistance.

Due to the uncertainty in the canopy parameters, the resistance is not entirely correct represented. It turns out that the resistance at the reef flat is over-predicted for the in-canopy model run. Moreover, the results of the calibrated shear stress run show that a calibration does not always lead to the best bed shear stress. In this case the found bed shear stress does not represent the resistance during the higher swell conditions.

Thus, these simulations do not show the accuracy of the representation of the physical processes, but the application and potential of the in-canopy model to a reef environment. When the rough estimations of the canopy parameters could be more accurate described, the results would improve significantly.

8

Discussion

8.1 XBeach-nh+

In this thesis, the reduced two layer model was compared to the one-layer model to show the effects on the hydrodynamics. In Rijnsdorp et al. (2014) the Noorloos experiment was modelled with a fully two layer model (SWASH). When these results are compared to the results of nh+, it appears that there is not a large difference for the bulk wave statistics. Thus, it is assumed that a constant non-hydrostatic pressure near the bottom does not deviate much from the real pressure distribution. Considering the non-hydrostatic pressure profile for linear waves given as (Cui et al., 2014),

$$q = \rho h \eta \left(1 - \frac{\cosh k(z+d)}{\cosh kd} \right) \quad (8.1)$$

it can be seen that the non-hydrostatic profile becomes constant near the bottom (see Figure 8.1). This explains why the assumption of a constant non-hydrostatic pressure is valid when the proper layer distribution is applied.

Furthermore, for an increasing kh , the profile becomes more constant near the bottom. Within the reduced two layer model the layer distribution (α) represents the height of this lower layer. Therefore, the accuracy of the model is depended on the layer distribution. The accuracy could be optimized when a spatial varying layer distribution (depended on the kh) would be used. However, most models are forced with random waves, which means that waves with different periods are present in the domain and no single value of α can represent all these waves. Furthermore, the kh cannot always be known beforehand for the whole domain, because the dominant period can vary within the domain. Thus, the simplification of a constant layer distribution is for most applications appropriate.

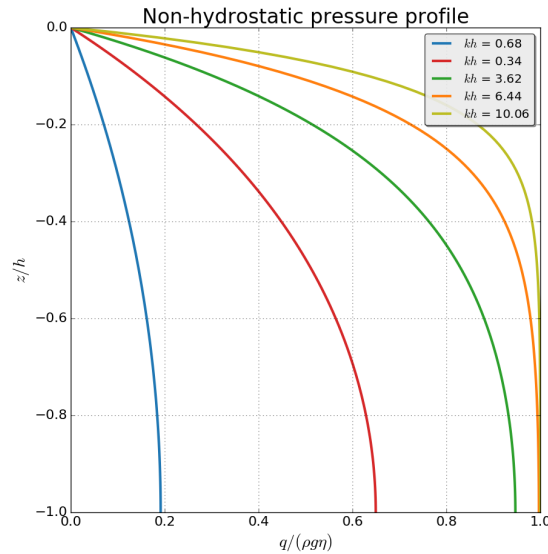


Figure 8.1: Normalized non-hydrostatic pressure profile for different kh values.

8.2 Boundary conditions

It has been shown that the implemented layer averaged boundary condition gives accurate results up to a kh of 2 for linear waves (2% relative error). This is a result of a different behaviour of the model compared to the "real" physics. Linear wave theory was used to describe the boundary signal, but when the kh increases this approach will introduce an error. The forced velocity does not correspond with the amplitude found by linear wave theory. It is possible to derive a solution for the linearised reduced two layer system. A boundary conditions based on these formulations would make this deviation less pronounced.

Alternatively, the velocity magnitude could be adjusted to obtain the correct surface amplitude when modelling deep water waves. This would lead to the wrong velocity in deep water, but the correct water level elevation. For most applications this will not be problem as only the near-shore hydrodynamics are important. This means that nh+ can be used up to a kh of 5 (dispersive behaviour), but that the boundary condition has to be adjusted for a kh larger than 2.

The implementation of the super-harmonics at the boundary did not improve the results for the Noorloos experiment. The large relative depth of the super-harmonics cannot be resolved within the reduced two layer model. This means that the super-harmonics can only be included in relative shallow water. However, in very shallow water the underlying assumptions of the derivation of the interaction coefficient are not valid ($a/d < 1$). Thus, only for limited wave conditions the super-harmonics can be applied, but it is argued that the inclusion of the sub-harmonics is more important than the super-harmonics. The spu-

rious waves which arise when the sub-harmonics are not included could penetrate much further into the domain, because these waves mostly do not break. Most of the spurious super-harmonics (which are less limited) will break at the breaking point as these waves are steeper than the primary waves. Moreover, a disturbed LF-wave signal (caused by the sub-harmonics) is not desired as the LF-waves are relevant for different coastal applications (e.g. erosion and resonance).

8.3 In-canopy model

The in-canopy model was derived for shallow water conditions by assuming a hydrostatic pressure and a constant velocity profile over the water depth. The results of Lowe experiments showed that this assumption did not result in a bias for the tests with a short wave period ($kh = 1.5$), where the forcing is not completely correct. Thus, the constant velocity profile and hydrostatic pressure did not introduce a large error in the in-canopy velocity for these conditions. Moreover, in deep water, where the in-canopy model is invalid, the canopy-induced force becomes very small and it does not have a large effect on the hydrodynamics (see section 6.5).

The addition of the shear stress term in the in-canopy model seems important for reef environments. The shear stress term is especially important for unidirectional flow and can mostly be neglected for oscillating flow. The sensitivity analyse of the individual parameters for a progressive wave (Figure 6.2) shows that shear stress term is not important for short waves. However, due to the LF-waves on the reef flat the shear stress term becomes more important for these longer waves (see Figure 6.6). The corals experience these long waves as a slowly varying current, which makes the shear stress more relevant compared to the pressure. Considering the laminar resistance term, it can safely be neglected. Since the turbulent drag force is much larger than the laminar resistance, the laminar resistance has no influence on any of the results in this thesis.

The choice for a porous in-canopy model with only the porosity as parameter instead of a geometrical based in-canopy model has shown its advantages. The applications within this thesis showed that by a good estimation of the canopy height and porosity, the hydrodynamics can already be accurately predicted. Furthermore, the λ_f is not easy to determine for a coral canopy which is necessary for a geometrical based in-canopy model. The porous in-canopy model will miss some information about the shape of the object (λ_f), which is necessary to accurately describe the drag force. Therefore, this information needs to be included in the formulation of the β -coefficient.

8.4 Validation resistance

The canopy-induced force is only implicitly validated. Only, the hydrodynamics were compared to the measurements, which show the accuracy of the magnitude of the canopy-induced

force. However, due to the lack of information about the in-canopy velocity, the individual terms in the canopy model cannot be properly validated. Only the experiments of Lowe gave insight in the in-canopy velocity. Although these results gave a good prediction, it cannot be verified whether this is also the case for a more complex environments (e.g. breaking waves). For example the inclusion of the vertical velocity could become more important for breaking waves. Thus, the in-canopy velocity at the breaking point is not necessarily correct represented. However the same holds for the bed shear stress, which is commonly used to represent the roughness. Therefore, it is assumed that the canopy-induced force is not completely wrong at the breaking point, because the important resistance term (drag force) has a similar formulation as the bed shear stress. Thus, the canopy-induced force at the breaking point should be treated with caution.

8.5 Estimation canopy parameters

During this thesis the canopy parameters were not always be known and had to be estimated. The sensitivity analyse of a progressive wave showed that varying these parameters influence the in-canopy velocity by 10%. The sensitivity analyse of the Buckley experiment showed that these parameters also have a large effect on the hydrodynamics (influence of ≈ 0.02 on the rel. bias for the short and ≈ 0.04 for the LF-waves).

It has been shown that the most important parameters are the β -coefficient and the inertia coefficient. Due to the fact that the β is largely depended on the porosity, it needs to be estimated with an external formulation. Within this thesis the modified Ergun relation were used to estimate the β -coefficient. Comparing the modified Ergun relation with relation found by Coceal and Belcher (2004) (equation 5.11), it can be shown that there is a lot of uncertainty in these formulations. The roughness cubes of the Buckley experiment can be represented by both formulations, which gave a β of $16m^{-1}$ for the modified Ergun relation and a β of $27m^{-1}$ for the formulation of Coceal. For low λ_p , found for corals (0.01 – 0.2), the modified Ergun relation gives at least a value within the range which was measured by Lowe et al. (2008), whereas the formulation of Coceal also requires a C_d and λ_f . This makes the modified Ergun relations preferred for the applications of corals.

9

Conclusions and recommendations

9.1 Conclusions

In this thesis the application of a reduced two layer non-hydrostatic model with the addition of a porous in-canopy model is presented. Subsequently, the answers to the research questions posted in the introduction are given in this chapter. First, the two research questions about the hydrodynamic part are answered. These research questions were formulated as,

How accurate can a reduced two layer non-hydrostatic model predict the bulk wave statistics for both a plane beach and reef environment?

and secondly,

How does the second reduced layer affects the accuracy compared to an one-layer model?

It has been shown that the reduced two layer model (nh+) has a much better dispersive behaviour than the one-layer model (nh). The dispersion relation can be accurately predicted (relative error of 2%) for linear waves up to a kh of 5, whereas nh gives the same result up to a kh of 1. Not only the dispersive behaviour diverge for a larger kh , but also the surface amplitude deviates from linear wave theory when the kh increases. This means that the forced velocity at the boundary will differ from surface amplitude given by linear wave theory when the kh becomes larger. Thus, nh+ gives accurate results for dispersive behaviour up to a kh of 5, but it requires an adapted velocity amplitude at the boundary when the kh is larger than 2.

The accuracy of nh+ for both a plane beach and a fringing reef were validated with respectively the Noorloos experiments and the Buckley experiments. The extra required time to solve the additional equations for the reduced two layer model was for both test below 5%. Thus, the improved dispersive behaviour does not limit the practical applicability.

Comparing the results of $nh+$ to the measurements of the Noorloos experiments, it can be concluded that the model is capable in modelling the energy transfer between the important wave components. The sub-harmonics (which are a dominant source of LF-waves) were accurately modelled, when the wave interactions of the difference frequencies were included in the boundary signal. Both steepening of the sub-harmonic, which requires energy transfer, and reflection of the sub-harmonics were accurately predicted.

Due to the large relative water depth of the Noorloos experiments ($kh = 2$), it was expected that $nh+$ would give more accurate results than nh as frequency dispersion is better captured with $nh+$. However, it appears that the improvement is mainly a result of the improved numerical formulations. The step from nh to $nh+1DV$ is much larger than from $nh+1DV$ to $nh+2DV$. The relative bias increases from -0.025 (SCI=0.09) to -0.015 (SCI=0.09) for the total wave height and increases from -0.133 (SCI=0.20) to -0.071 (SCI=0.13) for the sub-harmonic wave height when comparing nh and $nh+1DV$. Comparing $nh+1DV$ and $nh+2DV$ there is mainly a difference in the super-harmonics. Thus, a one-layer model can compete with the reduced two-layer model for these experiments.

The five Buckley experiments showed that XBeach- $nh+$ is also capable of modelling a reef environment. The short waves were very accurately predicted (rel. bias of 0.1 and SCI of -0.003). The same holds for the low frequency waves (LF-waves) with a slightly larger error (rel. bias of 0.29 and SCI of -0.081). The generated LF-waves at the reef crest were simulated according to the measurements. Only for the larger wave height and larger reef depth, there is a discrepancy in LF-wave energy between the model and measurements. Most of the uncertainty is present in the setup (rel. bias of 0.32 and SCI of -0.106).

Furthermore, there is a significant difference between $nh+1DV$ and $nh+2DV$ although the relative depth is smaller than 1. Especially, the setup and LF-waves benefit from the additional reduced layer. The relative bias decreases from -0.187 (SCI=0.34) to -0.081 (SCI=0.29) for the LF-waves when using the additional reduced layer. The improvement is mostly visible for two tests, where breaking is better captured when using two layers. Thus, it can be concluded that the reduced two layer model gives a robust prediction, whereas nh is not representative for all wave conditions.

An overview of the skill scores for both the Noorloos and Buckley experiments is given in Table 9.1. Based on these skill scores, the dispersive behaviour and a visual inspections of the results, it can be concluded that $nh+$ is preferred above nh .

In the following part the third research question related to the in-canopy flow will be answered,

What is the effect of a porous in-canopy model on the prediction of the resistance?

The show the effect of the porous in-canopy model on the prediction of the resistance, two validation datasets were used: a lab-test of a fringing reef with roughness elements (Buck-

CHAPTER 9. CONCLUSIONS AND RECOMMENDATIONS

ley experiment) and the data from a field campaign at Ningaloo Reef. Both datasets showed that the coral resistance has a large effect on the dissipation of LF-waves and increased water level (setup) over the reef. Without a proper representation of the coral roughness, the LF-waves were extremely over-predicted. Thus, these datasets showed the importance of including the effects of the corals into a reef study.

The Buckley experiment with roughness elements was used to show the effect of the in-canopy model on the hydrodynamics. It was shown that the in-canopy model gave a good prediction of the bulk wave statistics. Due to lack of information about the in-canopy velocity, it is hard to conclude whether the individual terms in the in-canopy model are predicted accurately. However, the validation of the in-canopy velocity for the experiments of Lowe et al. (2005b, 2008) showed that the in-canopy model represents the individual terms reasonable well for both oscillating and unidirectional flow fields. This does not show that the in-canopy model can be applied for complex environments (e.g. sloping bottom and breaking waves), but it suggest that at least the resistance on the reef flat (i.e. no breaking and almost horizontal bottom) is accurate described.

Similar results were found for the simulation of a 5 day swell event at Ningaloo reef, where the results of the un-calibrated in-canopy model were even better than the run with a calibrated shear stress formulation. Most likely, this difference is not related to the better prediction of the resistance, but due to a wrongly calibrated shear stress coefficient. However, it shows that the in-canopy model gives reasonable results with a rough estimation of the canopy properties (porosity and canopy height). Furthermore, it is argued that with a better formulation of the canopy parameters (e.g. β) for corals, the accuracy will improve significantly. Thus, the 5 day swell event has shown the potency of the in-canopy model to coral covered reefs.

It has been shown that by applying a reasonable estimation of the canopy-parameters, the in-canopy model makes it possible to accurately simulate the hydrodynamics. For engineering purposes this will lead to a reduction in model preparation, since there is no need for a time consuming calibration or expensive data campaign, when the coral porosity and height are known.

Table 9.1: The total skill scores (scatter index and relative bias) for the the experiments carried out in this thesis. Note that there was no setup computed in the Noorloos experiment. Moreover, the energy of the sub-harmonic ($H_{rms,\Delta f}$) was used as validation for the Van Noorloos test, whereas the LF-wave energy was used for the other simulations ($H_{rms,LF}$).

Simulation	H_{rms}		$H_{rms,LF}$ or $H_{rms,\Delta f}$		$\bar{\eta}$	
	SCI	Rel. bias	SCI	Rel. bias	SCI	Rel. bias
Van Noorloos	0.07	-0.0103	0.17	-0.022	-	-
Buckley - smooth	0.1	-0.003	0.29	-0.081	0.32	-0.106
Buckley - rough	0.09	-0.05	0.14	0.024	0.27	0.131
Ningaloo reef	0.28	0.053	0.31	-0.06	0.92	0.053

9.2 Recommendations

This thesis showed the application of XBeach-nh+ with the addition of an in-canopy model to predict the coral resistance. However, during this thesis different challenges were encountered. Based on these challenges the following recommendation were formulated,

1. Reduced two layer model

- (a) **Optimized layer distribution:** The accuracy of the dispersion relation for linear waves is depended on the layer distribution α (see equation 3.20). Within this thesis the α was kept constant at 0.33 for the whole domain. It could be verified what the effect is of a spatial varying α , depended on the depth and peak period. This could increase the applicability range of nh+. Within this thesis it was not possible to test a varying α , because the used validation tests did not include deep water conditions. Measurements of wave propagation from deep to shallow water is necessary to properly validate a spatial varying α and show whether this extend the applicability range of XBeach-nh+.
- (b) **Boundary conditions based on linearised solution:** In this thesis the physical equations (linear wave theory) were used to describe the boundary signal, but the results showed that this does not always result in the correct forced wave. A practical work-around solution would be to manually increase the forced wave height, but this is not always desired. The boundary conditions could also be formulated in terms of the solved equations (reduced two layer system). This would lead to a better result in deeper water. The following formulation could be used to force the model with the linearized solution of the reduced two layer system (?),

$$U^\alpha = \frac{\sigma^\alpha}{kd} \eta^\alpha \quad (9.1)$$

$$\Delta u^\alpha = \frac{\Delta c}{2c} \eta^\alpha \quad (9.2)$$

where U^α , Δu^α and η^α are the amplitudes for the solution of the linearised reduced two layer model, σ^α the radial frequency given by equation 3.20 and Δc is given as,

$$\Delta c = 2 \frac{c^2 - gd}{d(1 + \alpha)} \quad (9.3)$$

Where c is the wave celerity according to the dispersion relation given by equation 3.20. When the η^α is set to the desired wave height, it is possible to compute the boundary velocity signals.

- (c) **Validate for spurious waves:** The inclusion of wave interaction in the boundary conditions has been verified by the Noorloos experiment for the bound waves filtered in the frequency domain. Due to the same frequency of the spurious waves and the bound waves, these waves cannot be distinguished in the frequency domain. For a complete validation of the second order boundary conditions and the second order responds of the model, an analysis in the wave number domain could be performed. In the wave number domain, both the bound ($k_b = k_1 + k_2$) and free spurious waves ($k_f = k_3(\omega_1 + \omega_1)$) can be distinguished. In this way the second order responds of the model can be quantified in terms of suppressed spurious wave energy.

2. In-canopy model

- (a) **Formulation:** The formulation of the porous in-canopy model was based on the derivation of Lowe et al. (2008), but a different formulation is recommended based on the canopy parameters. Firstly, it is hard to estimate the β -coefficient. Therefore, it would be better to include a formulation for β -coefficient depended on the porosity in the in-canopy model. For example a validated Ergun relation for different coral types could be implemented.

Secondly, the shear stress formulation could be formulated as,

$$\frac{\partial \tau}{\partial z} = \mu \frac{U - U_c}{h_c} \quad (9.4)$$

Where μ is a vertical viscosity coefficient. This formulation is more consistent than the used formulation for a shear stresses. Moreover, there is more literature available which describes the shear stress with this formulation, where μ is a turbulent vertical viscosity (Mat).

- (b) **Validation in-canopy velocity:** The in-canopy model is validated indirectly by the bulk wave statistics. Only the experiments of Lowe could be used to show the accuracy of the in-canopy velocity. For a proper validation test, both the hydrodynamics and the velocity must be known. Measurements of the in-canopy velocity

in combination with the wave statistic, would improve the validation significant. Then, it would be possible to validate both the magnitude of the vegetation force and the individual terms in the canopy-induced force. Furthermore, a validation of the in-canopy flow for breaking waves would give more insight in the accuracy of the in-canopy model.

- (c) **Additional validation:** Only the Buckley experiment could be used to show the effects of the canopy induced force in detail. An additional validation for a different roughness element would show the applicability for other roughness elements, where the in-canopy velocity can be different. For example, the lab-test of Yao et al. (2018) would be a good extra validation test for a fringing reef with roughness elements. Different validation tests will also lead to a better understanding of the in-canopy flow and better formulation for the in-canopy flow.
- (d) **In-canopy parameters:** It is rather difficult to estimate the canopy properties. There is not a lot of literature which describes the canopy parameters for corals. Especially, the C_M is hard to predict for a 3-dimensional coral colony. To a lesser extent, this also holds for the β -coefficient, where there exist multiple formulations. However, these formulations contain much scatter. Therefore, it is recommended to study the effects of the drag and inertia force for different types of corals. A better formulation of the β -coefficient and C_M would improve the results of the in-canopy model significantly.

Bibliography

- Britter, R. and Hanna, S. (2003). Flow and dispersion in urban areas. *Annual Review of Fluid Mechanics*, 35(1):469–496.
- Buckley, M. L., Lowe, R. J., Hansen, J. E., and Van Dongeren, A. R. (2015). Dynamics of wave setup over a steeply sloping fringing reef. *Journal of Physical Oceanography*, 45(12):3005–3023.
- Buckley, M. L., Lowe, R. J., Hansen, J. E., and Van Dongeren, A. R. (2016). Wave Setup over a Fringing Reef with Large Bottom Roughness. *Journal of Physical Oceanography*, 46(8):2317–2333.
- Cassata, L. and Collins, L. B. (2008). Coral Reef Communities, Habitats, and Substrates in and near Sanctuary Zones of Ningaloo Marine Park. *Journal of Coastal Research*, 241:139–151.
- Coccal, O. and Belcher, S. E. (2004). A canopy model of mean winds through urban areas. *Quarterly Journal of the Royal Meteorological Society*, 130(599):1349–1372.
- Cui, H., Pietrzak, J., and Stelling, G. (2014). Optimal dispersion with minimized poisson equations for non-hydrostatic free surface flows. *Ocean Modelling*, 81:1–12.
- Darwin, c. (1836). *The Structure and Distribution of Coral Reefs*.
- Dean, R. G. and Bender, C. J. (2006). Static wave setup with emphasis on damping effects by vegetation and bottom friction. *Coastal Engineering*, 53(2):149–156.
- Feddersen, F., Gallagher, E., Guza, R., and Elgar, S. (2003). The drag coefficient, bottom roughness, and wave-breaking in the nearshore. *Coastal Engineering*, 48(3):189–195.
- Ferrario, F., Beck, M. W., Storlazzi, C. D., Micheli, F., Shepard, C. C., and Airolidi, L. (2014). The effectiveness of coral reefs for coastal hazard risk reduction and adaptation. *Nature communications*, 5:3794.

- Field, M. E., C. S. A. . E. K. R. (2002). Us coral reefs; imperiled national treasures.
- Finnigan, J. (2000). Turbulence in Plant Canopies. *Annual Review of Fluid Mechanics*, 32(1):519–571.
- Ghisalberti, M. (2002). Mixing layers and coherent structures in vegetated aquatic flows. *Journal of Geophysical Research*, 107(C2):3011.
- Gu, Z. and Wang, H. (1991). Gravity waves over porous bottoms. *Coastal Engineering*, 15(15 (1991)):497–524.
- Guza, R., Thornton, E., and Holman, R. (1985). Swash on steep and shallow beaches. In *Coastal Engineering 1984*, pages 708–723.
- Hasselmann, K. (1962). On the non-linear energy transfer in a gravity wave spectrum. *Journal of Fluid Mechanics*, 12((4)):481–500.
- Hoegh-Guldberg, O., Mumby, P. J., Hooten, A. J., Steneck, R. S., Greenfield, P., Gomez, E., Harvell, C. D., Sale, P. F., Edwards, A. J., Caldeira, K., Knowlton, N., Eakin, C. M., Iglesias-Prieto, R., Muthiga, N., Bradbury, R. H., Dubi, A., and Hatziolos, M. E. (2007). Coral reefs under rapid climate change and ocean acidification. *Science (New York, N.Y.)*, 318(5857):1737–1742.
- Holding, S., Allen, D. M., Foster, S., Hsieh, A., Larocque, I., Klassen, J., and Van Pelt, S. C. (2016). Groundwater vulnerability on small islands. *Nature Climate Change*, 6(12):1100–1103.
- Huang, Z. C., Lenain, L., Melville, W. K., Middleton, J. H., Reineman, B., Statom, N., and McCabe, R. M. (2012). Dissipation of wave energy and turbulence in a shallow coral reef lagoon. *Journal of Geophysical Research: Oceans*, 117(3):1–18.
- Hughes, T. P., Baird, A. H., Bellwood, D. R., Card, M., Connolly, S. R., Folke, C., Grosberg, R., Hoegh-Guldberg, O., Jackson, J., Kleypas, J., et al. (2003). Climate change, human impacts, and the resilience of coral reefs. *science*, 301(5635):929–933.
- Longuet-Higgins, M. S. and Stewart, R. W. (1962). Radiation stress and mass transport in gravity waves, with application to ‘surf beats’. *Journal of Fluid Mechanics*.
- Lowe, R. J., Falter, J. L., Bandet, M. D., Pawlak, G., Atkinson, M. J., Monismith, S. G., and Koseff, J. R. (2005a). Spectral wave dissipation over a barrier reef. *Journal of Geophysical Research C: Oceans*, 110(4):1–16.
- Lowe, R. J., Koseff, J. R., and Monismith, S. G. (2005b). Oscillatory flow through submerged canopies: 1. Velocity structure. *Journal of Geophysical Research C: Oceans*, 110(10):1–17.

BIBLIOGRAPHY

- Lowe, R. J., Shavit, U., Falter, J. L., Koseff, J. R., and Monismith, S. G. (2008). Modeling flow in coral communities with and without waves: A synthesis of porous media and canopy flow approaches. *Limnology and Oceanography*, 53(6):2668–2680.
- Luhar, M., Coutu, S., Infantes, E., Fox, S., and Nepf, H. (2010). Wave-induced velocities inside a model seagrass bed. *Journal of Geophysical Research: Oceans*, 115(12):1–15.
- Macdonald, I. F., El-Sayed, M. S., Mow, K., and Dullien, F. A. (1979). Flow through Porous Media—the Ergun Equation Revisited. *Industrial and Engineering Chemistry Fundamentals*, 18(3):199–208.
- Madsen, P. and Sørensen, O. (1993). Bound Waves and Triad Interactions in shallow water. *Ocean Engineering*, 20(4):1–25.
- Madsen, P., Sørensen, O., and Schäffer, H. (1997). Surf zone dynamics simulated by a Boussinesq type model. Part I. Model description and cross-shore motion of regular waves. *Coastal Engineering*, 32(4):255–287.
- Madsen, P. A., Murray, R., and Sorensen, O. R. (1991). A new form of Boussinesq equations with improved dispersion characteristics. *Coastal Engineering*, 15:371–388.
- McCall, R. T. (2015). *Process-based modelling of storm impacts on gravel coasts*. PhD thesis, plymouth university.
- McCall, R. T., Van Thiel de Vries, J. S., Plant, N. G., Van Dongeren, A. R., Roelvink, J. A., Thompson, D. M., and Reniers, A. J. (2010). Two-dimensional time dependent hurricane overwash and erosion modeling at Santa Rosa Island. *Coastal Engineering*, 57(7):668–683.
- Mccorquodale, J. A., Hannoura, A.-A. A., and Sam Nasser, M. (1978). Hydraulic conductivity of rockfill. *Journal of Hydraulic Research*, 16(2):123–137.
- Mendez, F. J. and Losada, I. J. (2004). An empirical model to estimate the propagation of random breaking and nonbreaking waves over vegetation fields. *Coastal Engineering*, 51(2):103–118.
- Morison, J., Johnson, J., Schaaf, S., et al. (1950). The force exerted by surface waves on piles. *Journal of Petroleum Technology*, 2(05):149–154.
- Nelson, R. C. (1996). Hydraulic roughness of coral reef platforms. *Applied Ocean Research*, 18(5):265–274.
- Nepf, H. M. and Vivoni, E. R. (2000). Flow structure in depth-limited, vegetated flow. *Journal of Geophysical Research: Oceans*, 105(C12):28547–28557.

-
- Noorloos, J. C. V. (2003). Energy transfer between short wave groups and bound long waves on a plane slope. (June).
- Ohyama T., Kioka, W., and Tada, A. (1995). Applicability of numerical models to nonlinear dispersive waves. *Journal of Coastal Engineering*, 24(94):297–313.
- Okihiro, M., Guza, R. T., and Seymour, R. J. (1992). Bound infragravity waves. *Journal of Geophysical Research : Oceans*, 97(7):11453–11469.
- Pearson, S. G., Storlazzi, C. D., van Dongeren, A. R., Tissier, M. F., and Reniers, A. J. (2017). A Bayesian-Based System to Assess Wave-Driven Flooding Hazards on Coral Reef-Lined Coasts. *Journal of Geophysical Research: Oceans*, pages 99–117.
- Péquignet, A. C. N., Becker, J. M., Merrifield, M. A., and Aucan, J. (2009). Forcing of resonant modes on a fringing reef during tropical storm man-yi. *Geophysical Research Letters*, 36(3).
- Pernetta, J. C. (1992). Impacts of climate change and sea-level rise on small island states: national and international responses. *Global Environmental Change*, 2(1):19–31.
- Quataert, E., Storlazzi, C., Van Rooijen, A., Cheriton, O., and Van Dongeren, A. (2015). The influence of coral reefs and climate change on wave-driven flooding of tropical coastlines. *Geophysical Research Letters*, 42(15):6407–6415.
- Reidenbach, M. A., Koseff, J. R., Monismith, S. G., Steinbuckc, J. V., and Genin, A. (2006). The effects of waves and morphology on mass transfer within branched reef corals. *Limnology and Oceanography*, 51(2):1134–1141.
- Rijnsdorp, D. P., Smit, P. B., and Zijlema, M. (2014). Non-hydrostatic modelling of infragravity waves under laboratory conditions. *Coastal Engineering*, 85:30–42.
- Roberts, C. M., McClean, C. J., Veron, J. E., Hawkins, J. P., Allen, G. R., McAllister, D. E., Mittermeier, C. G., Schueler, F. W., Spalding, M., Wells, F., Vynne, C., and Werner, T. B. (2002). Marine biodiversity hotspots and conservation priorities for tropical reefs. *Science*, 295(5558):1280–1284.
- Roelvink, J., McCall, R., Mehvar, S., Nederhoff, C., and Dastgheib, A. (2017). Improving predictions of swash dynamics in XBeach: The role of groupiness and incident-band runup. *Coastal Engineering*, (February):1–21.
- Roelvink, J., Reniers, A., Dongeren, A. V., Thiel, J. V., Vries, D., McCall, R., and Lescinski, J. (2009). Modelling storm impacts on beaches , dunes and barrier islands. *Coastal Engineering*, 56(11-12):1133–1152.
- Saad, Y. (2003). *Iterative methods for sparse linear systems*, volume 82. siam.

BIBLIOGRAPHY

- Sheppard, C., Dixon, D. J., Gourlay, M., Sheppard, A., and Payet, R. (2005). Coral mortality increases wave energy reaching shores protected by reef flats: Examples from the Seychelles. *Estuarine, Coastal and Shelf Science*, 64(2-3):223–234.
- Skotner, C. and Apelt, C. Application of a Boussinesq model for the computation of breaking waves Part 1: Development and verification., volume = 26 (10), year = 1999. *Ocean Engineering*, pages 905–925.
- Smit, P. (2014). Reduced two layer model [powerpoint slides]. Not published.
- Smit, P., Stelling, G., Roelvink, J., van Thiel de Vries, J., McCall, R., van Dongeren, A., Zwinkels, C., and Jacobs, R. (2010). Xbeach: Non-hydrostatic model. *Report, Delft University of Technology and Deltares, Delft, The Netherlands*.
- Sollitt, C. K., Cross, R. H., and Engineer, C. (1872). Wave transmission through permeable breakwaters. *Coastal Engineering*.
- Sorensen, O. R., Schaffer, H. A., and Madsen, P. A. (1998). Surf zone dynamics simulated by a Boussinesq type model. III. Wave-induced horizontal nearshore circulations. *Coastal Engineering*, 33(2-3):155–176.
- Stelling, G. and Zijlema, M. (2003). An accurate and efficient finite-difference algorithm for non-hydrostatic free-surface flow with application to wave propagation. *International Journal for Numerical Methods in Fluids*, 23(May 2002):1–23.
- Storlazzi, C. D., Elias, E., Field, M. E., and Presto, M. K. (2011). Numerical modeling of the impact of sea-level rise on fringing coral reef hydrodynamics and sediment transport. *Coral Reefs*, 30(SUPPL. 1):83–96.
- Taebi, S., Lowe, R. J., Pattiaratchi, C. B., Ivey, G. N., Symonds, G., and Brinkman, R. (2011). Nearshore circulation in a tropical fringing reef system. *Journal of Geophysical Research: Oceans*, 116(2):1–15.
- van der Westhuysen, A. J. (2010). Modeling of depth-induced wave breaking under finite depth wave growth conditions. *Journal of Geophysical Research: Oceans*, 115(C1).
- Van Dongeren, A. (2003). Numerical modeling of infragravity wave response during DELILAH. *Journal of Geophysical Research*, 108(C9):3288.
- Van Dongeren, A., Lowe, R., Pomeroy, A., Trang, D. M., Roelvink, D., Symonds, G., and Ranasinghe, R. (2013). Numerical modeling of low-frequency wave dynamics over a fringing coral reef. *Coastal Engineering*, 73:178–190.
- Van Gent, M. (1995). Porous flow through rubble-mound material. *Journal of waterway, port, coastal, and ocean engineering*, 121(3):176–181.

- van Rooijen, A., McCall, R., de Vries, J. v. T., van Dongeren, A., Reniers, A., and Roelvink, J. (2016). Modeling the effect of wave-vegetation interaction on wave setup. *Journal of Geophysical Research*, 121:4056–4076.
- Van Rooijen, A., McCall, R., Van Thiel de Vries, J., Van Dongeren, A., Reniers, A., and Roelvink, J. (2016). Modeling the effect of wave-vegetation interaction on wave setup. *Journal of Geophysical Research: Oceans*, 121(6):4341–4359.
- Ward, J. (1964). Turbulent flow in porous media. *Journal of the Hydraulics Division*, 90(5):1–12.
- Wyatt, A. S., Lowe, R. J., Humphries, S., and Waite, A. M. (2010a). Particulate nutrient fluxes over a fringing coral reef: Relevant scales of phytoplankton Production and mechanisms of supply. *Marine Ecology Progress Series*, 405(Hatcher 1997):113–130.
- Wyatt, A. S. J., Waite, A. M., and Humphries, S. (2010b). Variability in isotope discrimination factors in coral reef fishes: Implications for diet and food web reconstruction. *PLoS ONE*, 5(10):15–19.
- Yao, Y., He, F., Tang, Z., and Liu, Z. (2018). A study of tsunami-like solitary wave transformation and run-up over fringing reefs. *Ocean Engineering*, 149(August 2017):142–155.
- Yao, Y., Huang, Z., Monismith, S. G., and Lo, E. Y. M. (2012). 1DH Boussinesq modeling of wave transformation over fringing reefs. *Ocean Engineering*, 47:30–42.
- Zijlema, M., Stelling, G., and Smit, P. (2011). SWASH: An operational public domain code for simulating wave fields and rapidly varied flows in coastal waters. *Coastal Engineering*, 58(10):992–1012.

List of Figures

1.1	Number of people which receive risk protection by reefs	1
1.2	Thesis content	6
2.1	Reef definitions	8
2.2	Reef hydrodynamics	9
2.3	Reef dissipation	10
2.4	Unconfined and submerged canopies	13
2.5	Canopy physics	14
2.6	Canopy regimes	16
3.1	XBeach-nh+ layer definitions	21
3.2	Dispersive behaviour XBeach	23
3.3	XBeach boundary condition profile	25
3.4	Spectrum with wave interactions	27
3.5	Effect layer averaged boundary conditions	28
3.6	Spatial results of both boundary signals (depth- and layer averaged)	29
3.7	Effect wave interactions for a spectrum	30
4.1	Laboratory step-up of the Noorloos experiment	34
4.2	Result A1 and A4 of the Van Noorloos Experiment	37
4.3	Energy density spectrum for test A1 and A4	40
4.4	Time series of test A1 and A4	41
4.5	Wave interaction for the Van Noorloos test	42
4.6	Experimental set-up of they Buckley et al. (2015) experiment	43
4.7	Smooth Buckley results	45
4.8	Buckley results for the smooth runs	48
5.1	Schematic representation of the in-canopy model	52
5.2	Diagram of the in-canopy module	57

6.1	Results of the experiments of Lowe	62
6.2	Sensitivity analyses in-canopy flow	63
6.3	Results of the XBeach runs for the rough Buckley experiment	66
6.4	Result of the Buckley experiment	70
6.5	In-canopy velocity: Buckley rough	72
6.6	In-canopy flow - Buckley rough	73
7.1	Bathymetry at Ningaloo reef	78
7.2	Measured time series at Ningaloo reef	79
7.3	Energy density spectrum Ningaloo reef	80
7.4	Ningaloo map view of the vegetation	83
7.5	Ningaloo error	85
7.6	Time series of the results in Ningaloo	86
7.7	Water level at Ningaloo reef	87
7.8	Cross section and map view of Ningaloo Reef	89
7.9	Resistance at Ningaloo Reef	91
8.1	Non-hydrostatic pressure distribution	94
A.1	Boundary signal including bound waves	114
A.2	Vertical velocity profile Noorloos test A1	115
A.3	Calibration of Van Noorloos experiment	117
A.4	Result B4: cross section	117
A.5	Result B4: energy density spectrum	118
A.6	The time series for run B4.	119
B.1	Grid resolution for the Buckley test	123
C.1	Bed correction	128
C.2	XBeach results, without depth correction, is plotted against the data.	128
D.1	Calibration Buckley rough	130
E.1	Time series of the calibrated friction formulation run	132
E.2	Water level at Ningaloo reef of the calibrated friction formulation run	133
G.1	Xbeach domain definitions.	141
G.2	Xbeach numerical domain.	142

List of Tables

4.1	Noorloos experiment wave conditions	35
4.2	Results for the Noorloos experiment	38
4.3	Model set-up for the Buckley test	44
4.4	Buckley test results	46
6.1	Setting Lowe 2005	61
6.2	Setting lowe 2008	61
6.3	Skill scores Buckley experiment	68
6.4	Skill scores for different canopy parameters	74
7.1	Calibration Ningaloo reef	82
7.2	Coral species at Ningaloo reef	83
9.1	Results thesis	100
A.1	Calibration Van Noorloos test (XBeach-nh+2DV)	115
A.2	Calibration Van Noorloos test (XBeach-nh+1DV)	116
A.3	Calibration Van Noorloos test (XBeach-nh)	116
B.1	Accuracy of the Buckley measurements	121
B.2	Grid resolution of the Buckley test	122
B.3	Calibration Buckley test - XBeach-nh+1DV	124
B.4	Calibration Buckley test - XBeach-nh+2DV	124
B.5	effect α on run 4	125
D.1	Calibration Buckley rough	129
E.1	Grid Ningaloo reef	131

A

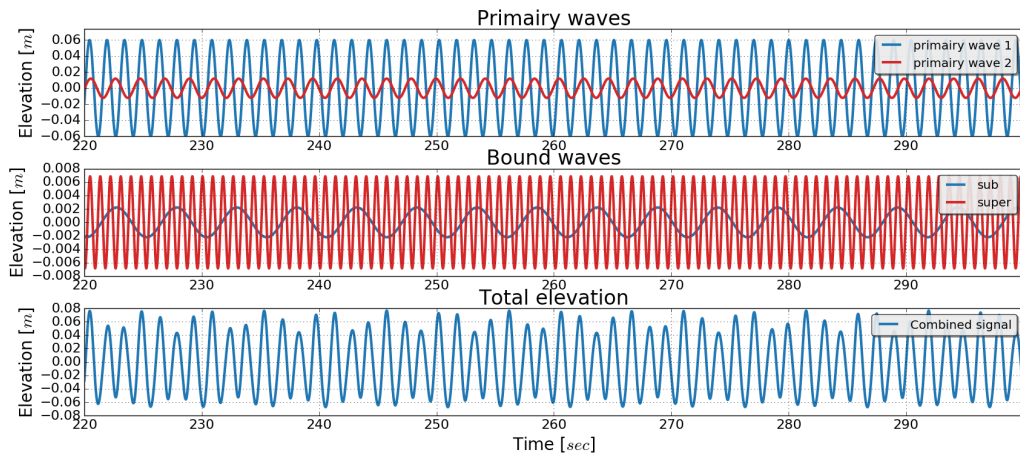
Noorloos Experiment

Within this section some additional results and description is given for the Noorloos experiment.

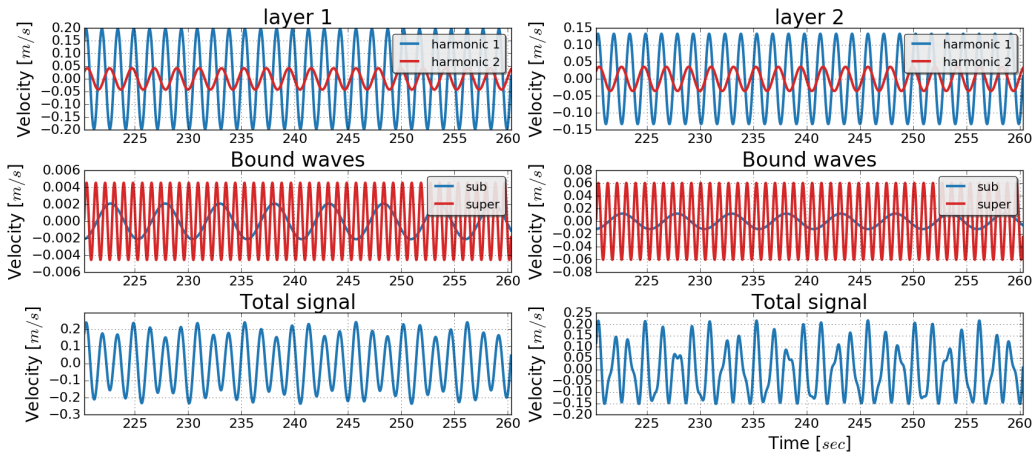
A.1 Second order wave interaction

In Figure A.1 the elevation signal at the boundary including the bound waves is shown (test A1). The upper panel shows the elevation of both primary waves. The super and sub harmonic are shown in the second panel. It can be seen that the sub harmonic is out of phase with the wave group, whereas the super harmonic is in phase with the wave group. The last panel shows the forced combined signal the water level elevation.

Apart from the elevation, the velocity should also be forced at the boundary. The layer averaged velocities are shown in Figure A.1 for both layers. It can be seen that there is a difference between the amplitude of both layers, which is caused by the relative large water depth ($kh = 1.4$). The velocity profile of both primary waves is shown in Figure A.2.



(a) Water level elevation signal



(b) Velocity signal

Figure A.1: Boundary signal including bound waves. The first sub-figure shows the elevation signals. The upper panel shows the elevation of the two primary waves. The second panel shows the corresponding bound waves. The last panel the combined signal is shown which is the forced elevation at the boundary. The second sub-figure shows the velocity signals. The upper panels shows the velocity signal for both layers. the second panel shows the bound velocities and the last panel shows the combined signals.

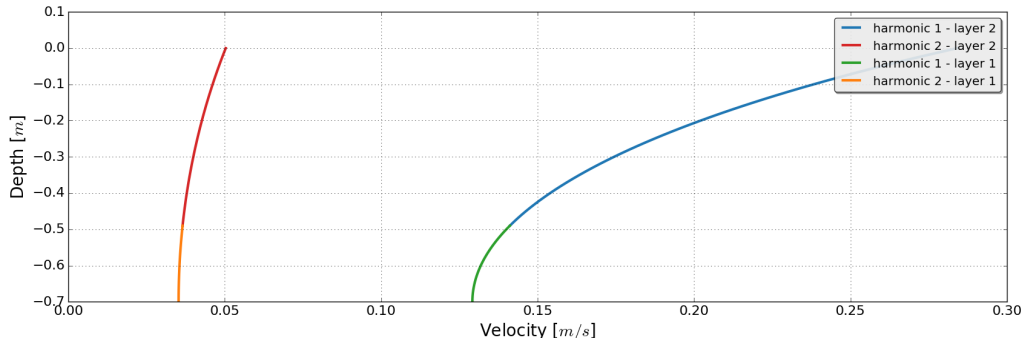


Figure A.2: The vertical velocity profile for the primary waves of test A1.

A.2 Calibration

The three different modes of XBeach non-hydrostatic (nh, nh+1D and nh+) were calibrated. First the breaker steepness was calibrated based on the breakpoint. Thereafter, the bottom friction was calibrated. Mostly, the skill scores for the sub-harmonics were used to calibrate the bottom friction. In Table A.1 the results for the calibration with XBeach-nh+2DV are shown. Table ?? shows the results for the runs with XBeach-nh+1DV and Table A.3 the results for XBeach-nh. These results shown that both runs with XBeach-nh+ give the best results with a breaker steepness of 0.4 and a manning coefficient of $0.01 s/m^{1/3}$. For XBeach-nh a breaker steepness of 0.3 and a manning coefficient of $0.005 s/m^{1/3}$. The effect of this calibration for run XBeach-nh+2DV is shown in Figure A.3, where both the effect of the breaker steepness and the bottom friction is plotted.

Table A.1: The computed skill scores for the different friction coefficients and breaking steepness with XBeach-nh+2DV.

XBeach-nh+2DV breaking steepness	H_{rms}		$H_{rms,\Delta f}$	
	SCI	Rel. bias	SCI	Rel. bias
0.3	0.08	-0.061	0.29	-0.051
0.4	0.05	-0.028	0.19	-0.046
0.5	0.09	0.005	0.14	-0.039
Manning [$s/m^{1/3}$]	SCI	Bias	SCI	Bias
$n = 0.001$	0.05	-0.021	0.3	0.201
$n = 0.005$	0.05	-0.023	0.25	0.11
$n = 0.01$	0.05	-0.028	0.19	-0.045
$n = 0.015$	0.05	-0.031	0.22	-0.142

Table A.2: The computed skill scores for the different friction coefficients and breaking steepness with XBeach-nh+1DV.

XBeach-nh+1DV breaking steepness	H_{rms}		$H_{rms,\Delta f}$	
	SCI	Rel. bias	SCI	Rel. bias
0.3	0.08	-0.064	0.32	0.039
0.4	0.06	-0.025	0.22	0.071
0.5	0.20	0.044	0.32	-0.082
Manning [$s/m^{1/3}$]	SCI	Bias	SCI	Bias
$n = 0.001$	0.06	-0.016	0.48	0.362
$n = 0.005$	0.06	-0.019	0.38	0.255
$n = 0.01$	0.06	-0.025	0.22	0.071
$n = 0.015$	0.06	-0.029	0.17	-0.031
$n = 0.02$	0.07	-0.032	0.22	-0.113

Table A.3: The computed skill scores for the different friction coefficients and breaking steepness with XBeach-nh

XBeach-nh breaking steepness	H_{rms}		$H_{rms,\Delta f}$	
	SCI	Rel. bias	SCI	Rel. bias
0.2	0.19	-0.094	0.35	-0.148
0.3	0.08	-0.024	0.19	-0.148
0.4	0.14	0.014	0.29	-0.137
0.5	0.2	0.044	0.32	-0.082
Manning	SCI	Bias	SCI	Bias
$n = 0.001$	0.08	-0.055	0.48	0.297
$n = 0.005$	0.08	-0.021	0.15	0.001
$n = 0.01$	0.08	-0.024	0.19	-0.148
$n = 0.015$	0.08	-0.026	0.30	-0.237

APPENDIX A. NOORLOOS EXPERIMENT

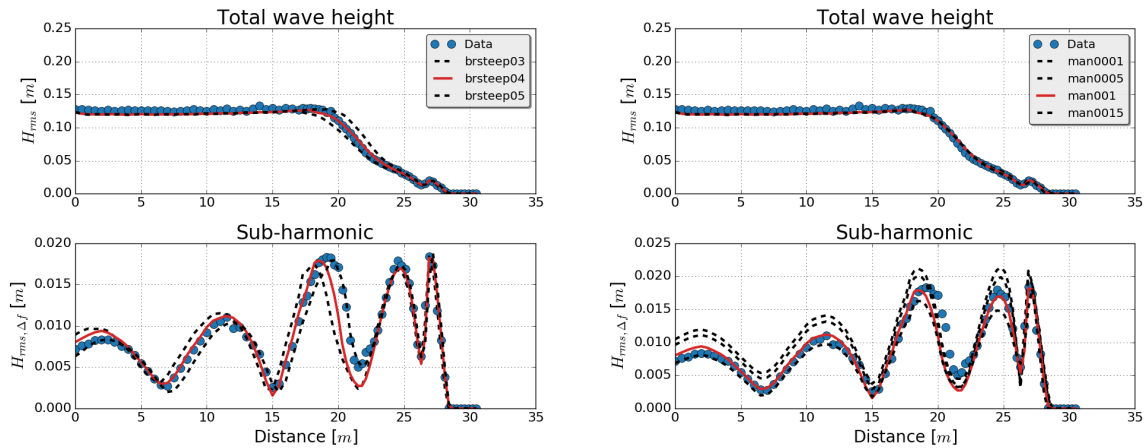


Figure A.3: The results of the H_{rms} and $H_{rms,\Delta f}$ for different breaking steepness (left panel) and friction parameter (right panel). These results are computed with nh+2DV.

A.3 Results test B4

This section shows the results for test B4 of the Noorloos experiment. In Figure A.4 the cross shore variability of the total wave height (H_{rms}), the sub-harmonic wave height ($H_{rms,\Delta f}$) and the super-harmonics ($H_{rms,(f_1+f_2)}$) is shown. The results of the different runs are shown with different lines. It can be seen that the breaking point is just to far onshore, which will also affect the sub-harmonic.

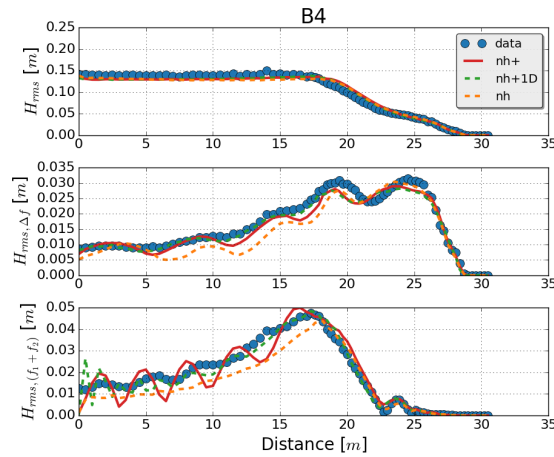


Figure A.4: Results of the Van Noorloos experiment B4 . The upper panel show the H_{rms} and the lower panel the filtered low frequency $H_{rms,\Delta f}$.

The spectrum of test B4 is shown in Figure A.5. Compared to test A1 and B4 the energy density variance of the sub and super harmonics is much larger. This can be seen in figure A.6, where the time series of test B4 are shown. The amplitude of the sub-harmonic is almost the same as the primary wave for location $x = 26.3m$. Moreover, the breaking of the low frequency waves is clearly visible for the on-shore locations.

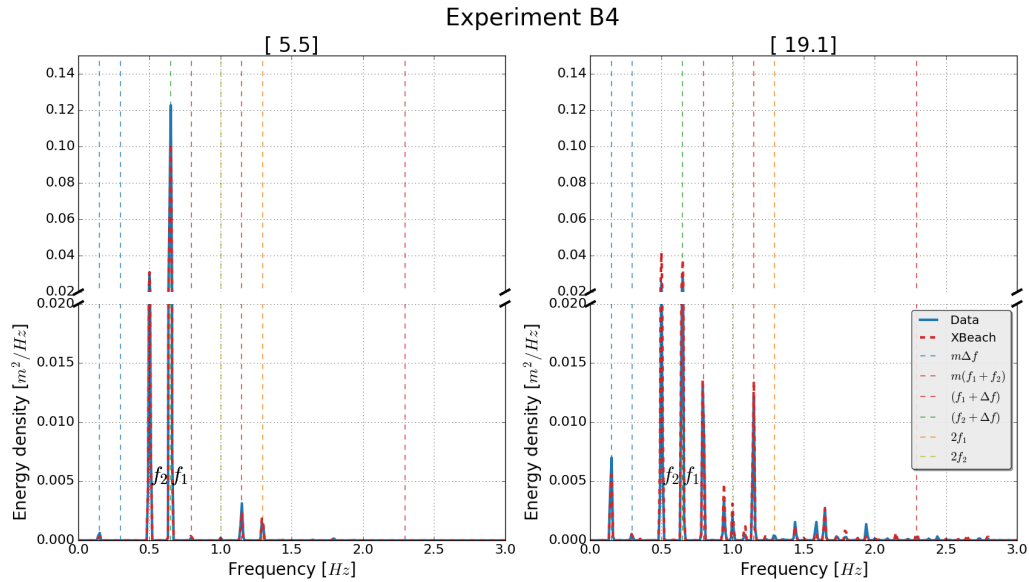


Figure A.5: energy density spectrum of test B4 for two locations. The dashed lines show the different wave components.

APPENDIX A. NOORLOOS EXPERIMENT

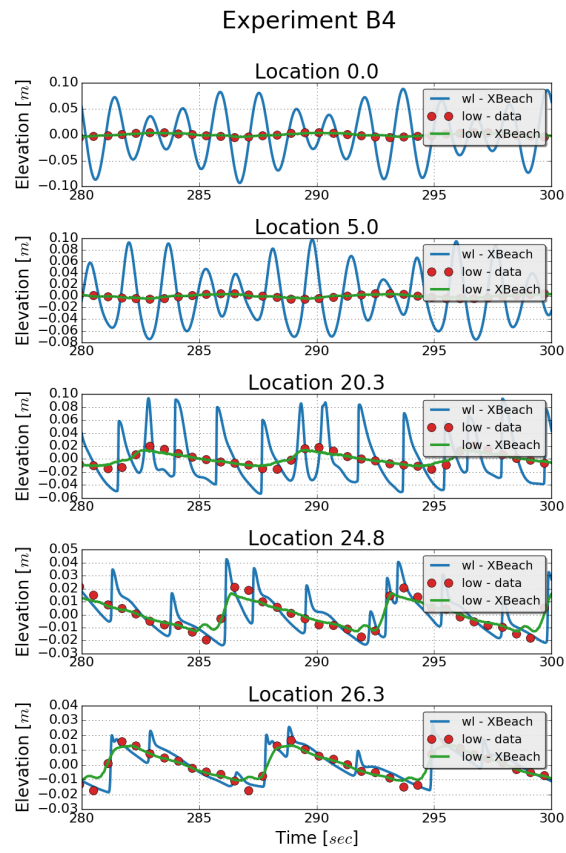


Figure A.6: The time series for run B4.

B

Buckley experiment - smooth

This section shows the results of the calibration of the smooth Buckley experiment and the accuracy of the measured data.

B.1 Accuracy Buckley experiment

The simulation period determines the certainty of the statistical skill scores. The period of the measurements is 2000 seconds. This corresponds with roughly 800 short waves and 400 low frequency waves. This means that the statistics of the short waves can be given more accurate than those of the low frequency waves. To estimate the accuracy of the relative bias and scatter index, multiple runs of 2000 seconds were compared to a run of 6000 seconds. This resulted in a mean skill score, which gives an idea of the accuracy that can be achieved. These mean skill scores are shown in Table B.1.

Table B.1: Mean errors for 7 runs with period of 2000 sec compared to a run of 600 sec run. The margin of the error is estimated by $z \frac{\sigma}{\sqrt{n}}$ with the standard deviation, σ , sample size, $n = 7$, and the level of confidence (95%), $z = 1.95$.

H_{rms}		$H_{rms,LF}$		$\bar{\eta}$	
\overline{SCI}	$\overline{ Bias }$	\overline{SCI}	$\overline{ Bias }$	\overline{SCI}	$\overline{ Bias }$
0.012 ± 0.005	0.0077 ± 0.008	0.037 ± 0.008	0.011 ± 0.005	0.018 ± 0.014	0.012 ± 0.0187

B.2 Calibration

B.2.1 Grid resolution

For test 4 the grid resolution was varied to determine the final grid size. In Table B.2 the accuracy is shown for different grid resolutions and Figure B.1 shows the results for different grid

resolutions. These simulations were done with a breaking steepness of 0.8 and a manning coefficient of $0.01 s/m^{1/3}$. It can be seen that 80 point per wave length gave the best results and therefore 80 ppwl were used for all the simulations.

Table B.2: Accuracy of the model for different grid resolutions. The grid resolution is expressed as the point per wave length (ppwl).

ppwl	H_{rms}		$H_{rms,LF}$		$\bar{\eta}$	
	SCI	Bias	SCI	Bias	SCI	Bias
20	0.11	-0.058	0.39	-0.32	0.42	-0.27
40	0.10	-0.04	0.32	-0.24	0.3	-0.16
60	0.09	-0.023	0.3	-0.24	0.25	-0.13
80	0.08	-0.01	0.29	-0.19	0.24	-0.12
100	0.08	-0.022	0.3	-0.22	0.25	-0.11

APPENDIX B. BUCKLEY EXPERIMENT - SMOOTH

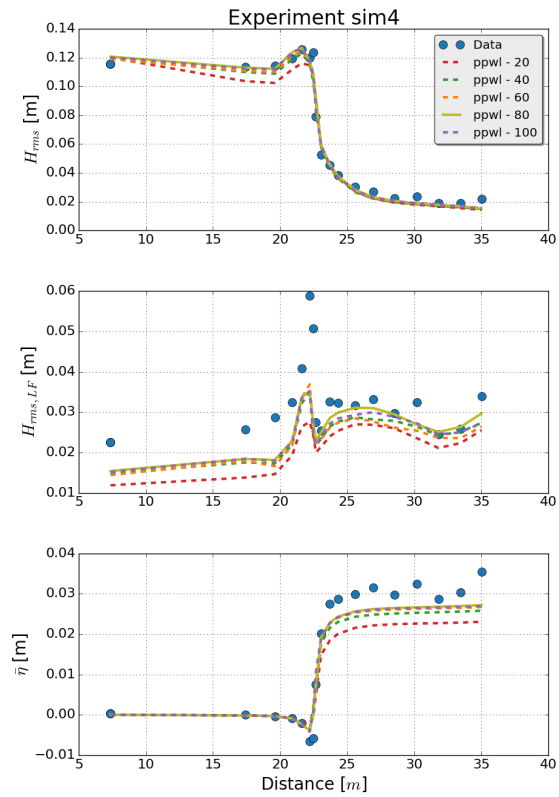


Figure B.1: The result for different grid resolutions. The different runs are indicated with a point per wave length (ppwl)

B.2.2 Breaker steepness and bottom friction

The calibration of the breaker steepness and manning coefficient for XBeach-nh+2DV is shown in table B.3. The results of XBeach-nh+1DV is shown in Table B.4. To show the improvement of the calibration Figure B.2 shows the results for the calibration of nh+2DV.

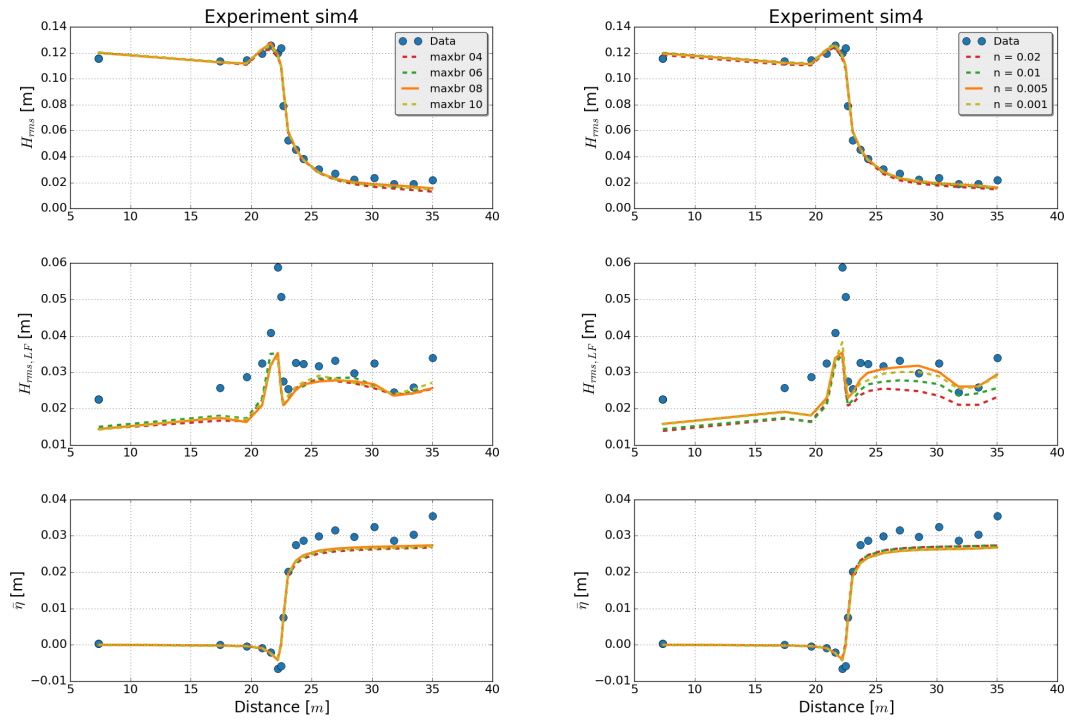
Table B.3: The computed error for the different friction formulations of all the output points.

nh+1DV breaking steepness	H_{rms}		$H_{rms,LF}$		$\bar{\eta}$	
	SCI	Bias	SCI	Bias	SCI	Bias
0.4	0.1	-0.047	0.38	-0.31	0.28	-0.15
0.6	0.09	-0.03	0.36	-0.29	0.26	-0.13
0.8	0.09	-0.015	0.36	-0.3	0.23	-0.11
1.0	0.08	-0.019	0.35	-0.3	0.25	-0.13
1.2	0.08	-0.005	0.33	-0.26	0.23	-0.12
1.4	0.08	-0.005	0.34	-0.28	0.23	-0.12
Manning coefficient						
0.001	0.08	-0.005	0.33	-0.26	0.23	-0.12
0.005	0.08	-0.003	0.32	-0.25	0.24	-0.13
0.01	0.09	-0.025	0.41	-0.36	0.22	-0.1
0.02	0.08	-0.019	0.33	-0.25	0.26	-0.15

Table B.4: The computed skill scores for the different friction formulations and breaker steepness

nh+2DV breaking steepness	H_{rms}		$H_{rms,LF}$		$\bar{\eta}$	
	SCI	Bias	SCI	Bias	SCI	Bias
0.4	0.09	-0.029	0.33	-0.26	0.26	-0.13
0.6	0.09	-0.018	0.31	-0.24	0.24	-0.13
0.8	0.08	-0.01	0.32	-0.25	0.23	-0.11
1.0	0.09	-0.016	0.32	-0.24	0.24	-0.12
Manning coefficient						
0.001	0.08	-0.01	0.32	-0.25	0.23	-0.11
0.005	0.08	-0.011	0.28	-0.18	0.25	-0.14
0.01	0.08	-0.01	0.32	-0.25	0.23	-0.11
0.02	0.09	-0.031	0.34	-0.29	0.23	-0.1

APPENDIX B. BUCKLEY EXPERIMENT - SMOOTH



(a) Breaking steepness

(b) Manning coefficient

Figure B.2: Results for the calibration of the breaker steepness and the manning coefficient

B.3 Effect layer distribution

The results for different α values is shown in Table B.5. These results were computed for simulation 4 of the Buckley test. These results show that the default α of 0.3 gives the best results.

Table B.5: The skill scores for different layer distributions (α).

Layer distribution	H_{rms}		$H_{rms,LF}$		$\bar{\eta}$	
	SCI	Bias	SCI	Bias	SCI	Bias
0.1	0.08	-0.012	0.27	-0.17	0.25	-0.14
0.33	0.08	-0.005	0.28	-0.18	0.24	-0.13
0.5	0.08	-0.011	0.27	-0.18	0.25	-0.13
0.66	0.08	-0.015	0.28	-0.19	0.25	-0.14
0.9	0.08	-0.013	0.29	-0.19	0.24	-0.13

C

In-canopy model - bottom correction

Besides of the resistance, the canopy will also affect the flux area. When the water level is relative shallow compared to the vegetation there will be less "space" to flow. In this section it is verified whether an adjusted flux area would increase the results. Therefore the bottom level is updated according to,

$$z_b = \begin{cases} z_b - h_c \lambda_p & h_c < h_0 \\ z_b - h_0 \lambda_p & h_c > h_0 \end{cases} \quad (\text{C.1})$$

Where the bottom level, z_b , is positive downwards. With this changed bottom level, the continuity equation is more accurate computed. For an emergent vegetation the initial water depth is used as canopy height.

The effect of the bottom correction is tested by simulating different h_c/h ratios. Monochromatic waves ($f = 0.6$ and $a = 0.1$) are modelled for a depth of 0.7 m. A 1/20 slope is used to dissipate the waves at the end of the domain. The canopy height is varied with 0.35, 0.1, 0.05, 0.7 and 1.0 m. The canopy-induced force is set to zero to show the effects of the bed level change. In figure C.1 the H_{rms} is plotted for different canopy heights.

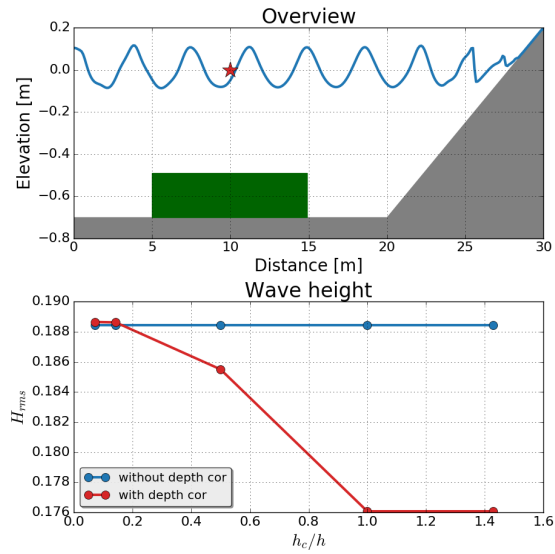


Figure C.1: The effect of the bed correction on the wave height. The upper panel shows the domain and the vegetation (green patch). For the location of the red star wave height is plotted for different canopy heights.

The depth correction is studied by comparing the simulation with and without depth correction of the rough Buckley experiments. These results are shown in Figure C.2. Apparently, the simulation without depth correction do not improve the results. Other processes are negatively affected by this bed correction. For example, wave breaking could be slightly different for an increased bed.

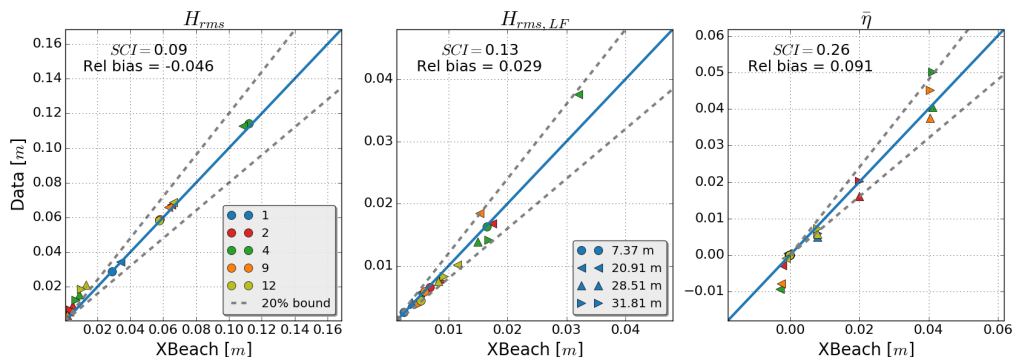


Figure C.2: XBeach results, without depth correction, is plotted against the data.

D

Buckley experiment - rough

The results for different Manning coefficients is shown in Table D.1. Based on the LF-wave height, a friction coefficient of $0.05s/m^{1/3}$ was used for all the simulated experiments. A higher Manning coefficient would give a better result for the short waves, but have a much worse prediction for the LF-wave height (see Figure D.1).

Table D.1: The computed error for the different friction formulations of all the output points.

n [$s/m^{1/3}$]	H_{rms}		$H_{rms,LF}$		$\bar{\eta}$	
	SCI	Rel. bias	SCI	Rel. bias	SCI	Rel. bias
0.01	0.14	0.1	0.48	0.4	0.15	-0.03
0.05	0.08	0.024	0.14	-0.10	0.21	0.11
0.1	0.07	-0.001	0.29	-0.25	0.22	0.07
0.15	0.07	-0.002	0.28	-0.24	0.22	0.07

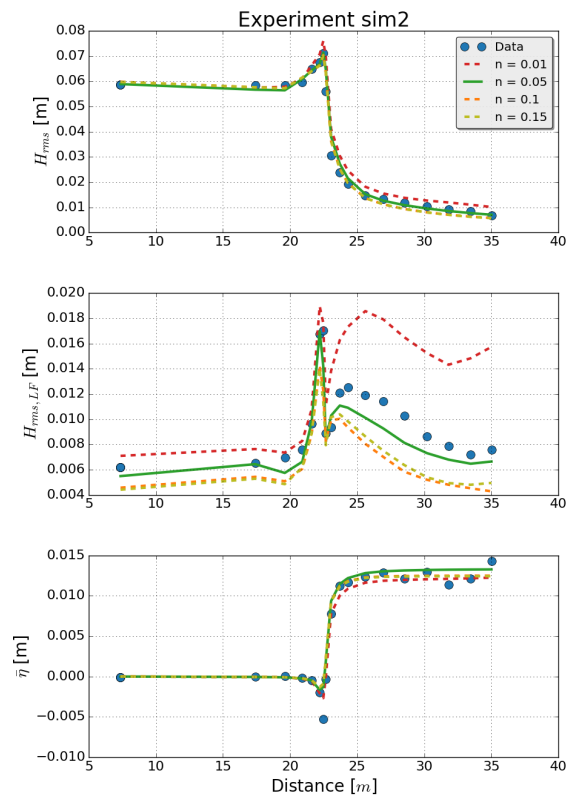


Figure D.1: The results for different values of the Manning coefficient compared to the measurements.

E

Ningaloo reef

This section shows the sensitivity to the grid size and domain size, results for the calibrated shear stress runs and additional results for the in-canopy run.

E.1 Sensitivity

A 6 hour simulation was used to verify the effect of the y resolution and neglecting the channels. Due to a semi diurnal tide, a low and a high water is present in this simulation. The simulations starts at the same moment which is used for the calibration runs. All these simulation were computed with a constant manning of $0.01 s/m^{1/3}$ and a breaking steepness of 0.4. The results are shown in Table E.1. Although these skill scores are very bad (due to the un-calibrated settings), these results show that the simplification in the domain does not have a very large effect on the hydrodynamics. It can be seen that the setup is slightly better for the larger domain (including the channels). Furthermore, the smaller y resolution only shows a better result for the short waves. Thus, it is assumed that the reduced domain with a y-resolution of $10m$ gives a reasonable prediction.

Table E.1: The accuracy of different runs for Ningaloo reef. The reference run is a simulation including the channels, whereas the reduced run is without the channels.

Run	H_{rms}		$H_{rms,LF}$		$\bar{\eta}$	
	SCI	Rel. bias	SCI	Rel. bias	SCI	Rel. bias
reference and $dy = 10m$	0.84	0.637	3.01	2.64	-1.32	0.637
reduced and $dy = 10m$	0.87	0.679	2.82	2.49	-1.47	0.679
reduced and $dy = 7.5m$	0.86	0.658	2.87	2.56	-1.5	0.658

E.2 Results Ningaloo reef - run: shear stress formulation

The results for the run with the calibrated shear stress formulation is shown in this section. Figure E.1 shows the short and the low frequency wave time series and Figure E.2 the results the mean water level. This figure clearly shows the overestimation of the short waves and the underestimation of the LF-waves.

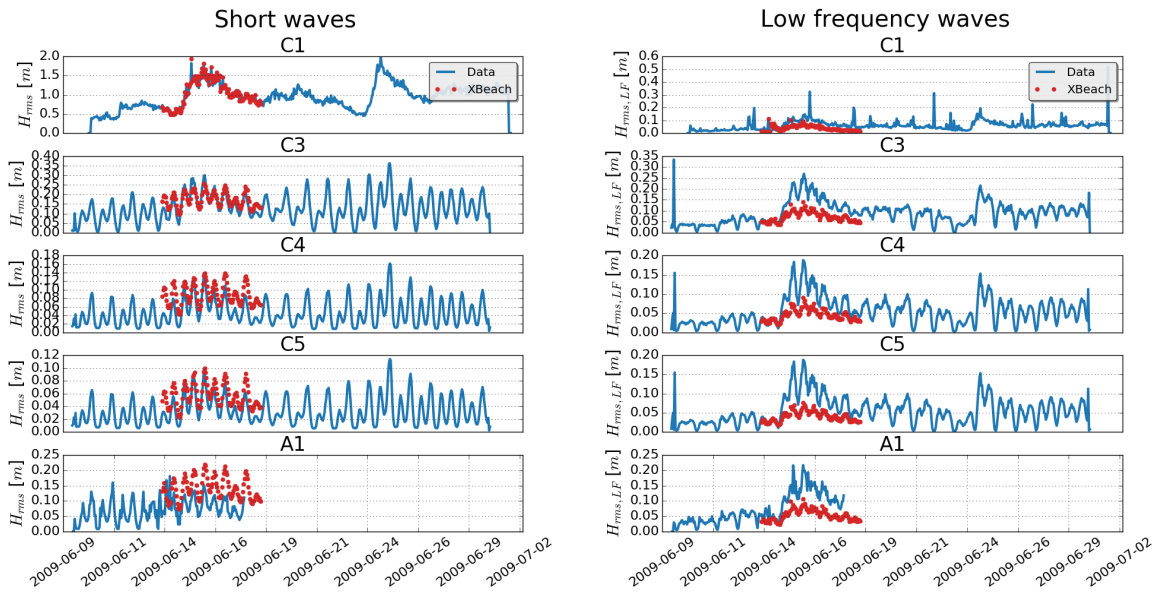


Figure E.1: The time series of the XBeach results compared to the measurements. The left panel shows the short wave heights and the right panel the low frequency waves.

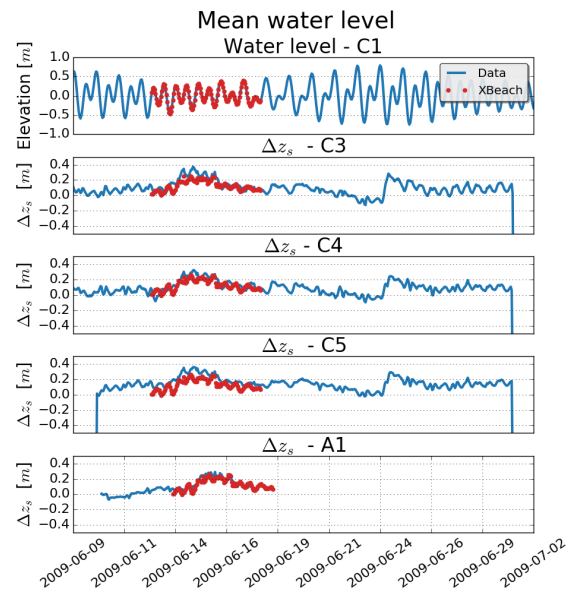


Figure E.2: The time series of the XBeach results and the measurements of the mean water level (C1) and the setup (C-3-5)

F

Skill scores

To quantify the skill of a result, the scatter index (SCI) and the relative bias (rel bias) as given in van der Westhuysen (2010) were used within this thesis. The scatter index is computed as,

$$SCI = \frac{\sqrt{\langle(\tilde{y} - y)^2\rangle}}{\langle y \rangle} \quad (\text{E.1})$$

Where y is the measured data and \tilde{y} the model output. This scatter index is actually the standard deviation normalized by the mean of the data. The relative bias is given by,

$$bias = \frac{\sum_{i=1}^N \tilde{y}^i - y^i}{\sum_{i=1}^N y^i} \quad (\text{E.2})$$

where y is the measured data and \tilde{y} the model output. The relative bias represents the deviation of the predicted output with the respect to the data.



G

XBeach-nh background

G.1 XBeach non hydrostatic

XBeach-nh is the non-hydrostatic mode within the XBeach model. This mode solves the non-linear shallow water equation with the addition of the non-hydrostatic pressure and the vertical velocity. The non-hydrostatic term is necessary to correctly model wave propagation. Without the non-hydrostatic pressure frequency dispersion is absent, which causes that waves of different wavelength to travel with different speeds.

For example, the breaking point can not be modelled without the non-hydrostatic pressure. In hydrostatic models waves will only become steeper due to non-linear terms. The non linear terms will cause the waves to deform, whereas frequency dispersion will stabilize the wave. The second order waves will travel slower than the primary wave, which stabilizes the wave. Thus, the breaking point is determined by the balance between frequency dispersion and the wave deformation.

G.2 Governing equations

The governing equation in Xbeach-nh are based on the Navier-stokes equations. The Navier-stokes equations are nothing more than the conservation of momentum with the assumption of (1) in-compressible, (2) homogeneous and (3) Newtonian flow. For coastal applications it is common to assume an in-compressible flow. Secondly, a homogeneous fluid has no variation in density. In reality there are variation in density caused by differences in salinity or temperatures. Only for the scale of wave propagation there are no major density differences. At least, Newtonian fluid is a fluid where the viscose stresses are linear with the deformation. This implies that a constant viscosity can be used to describe the viscose

stresses. With these assumption the Navier-stokes equations are given by,

$$\frac{\partial \mathbf{U}}{\partial t} + \nabla(\mathbf{U} \otimes \mathbf{U}) = -\frac{1}{\rho} \nabla P + \mathbf{g} + \nabla T \quad (\text{G.1})$$

Where \mathbf{U} is the velocity vector, P the pressure, \mathbf{g} the gravitational force and T the viscose stresses.

The pressure can be divided into two parts: the hydrostatic pressure and the dynamic pressure. Following this approach the pressure is given by,

$$P = \rho g(\eta - z) + \rho q + P_0 \quad (\text{G.2})$$

Where η is the water level, z the water depth, q the dynamics pressure and P_0 atmospheric pressure.

It is not possible to solve the Navier-stokes equations on the scale of turbulence for large coastal regions. Therefore, the velocity is split into two parts: the mean flow (u) and the turbulent motion (u'). To remove the turbulent motion, the equation is averaged over the turbulent scales. This will introduce new terms in the equation which are the turbulent stresses (the Reynolds stress). Using the Boussinesq hypothesis these stresses are expressed in mean flow properties. This result in a turbulent stress as,

$$\tau_{ij} = \rho \nu_t \left(\frac{\partial U_i}{\partial x_j} + \frac{\partial U_j}{\partial x_i} \right) \quad (\text{G.3})$$

Where ν_t is the turbulent eddy viscosity. The turbulent eddy viscosity can be determined from a close module. This is due to the fact that the turbulent stresses are much larger than the viscous stresses, the viscose stress can be neglected.

With the above described formulations the Navier-stokes equations for the x-direction in component form holds,

$$\frac{\partial u}{\partial t} + \frac{\partial u^2}{\partial x} + \frac{\partial uv}{\partial y} + \frac{\partial uw}{\partial z} = \frac{\partial q}{\partial x} - g \frac{\partial \eta}{\partial x} + \frac{1}{\rho} \frac{\partial \tau_{xx}}{\partial x} + \frac{1}{\rho} \frac{\partial \tau_{yx}}{\partial y} + \frac{1}{\rho} \frac{\partial \tau_{zx}}{\partial z} \quad (\text{G.4})$$

Next to the conservation of momentum also conservation of mass hold for a fluid. This continuity equation is given by,

$$\frac{\partial \rho}{\partial t} + \frac{\partial \rho u}{\partial x} + \frac{\partial \rho v}{\partial y} + \frac{\partial \rho w}{\partial z} \quad (\text{G.5})$$

Due to the incomprehensibility the conservation of mass can be simplified to the conservation of volume,

$$\nabla \mathbf{U} = 0 \quad (\text{G.6})$$

For free surface flows, another equations is necessary to determine the free surface elevation. An expression for the free surface is obtained by integrating the continuity equation over the depth,

$$\int_{-d}^{\xi} \nabla \mathbf{U} dz = \int_{-d}^{\xi} \frac{\partial u}{\partial x} dz + \int_{\xi}^{-} d \frac{\partial v}{\partial y} dz + w|_{z=\xi} + w|_{z=-d} \quad (\text{G.7})$$

APPENDIX G. XBEACH-NH BACKGROUND

The vertical velocity at the free surface is equal to the material derivative of the free surface. The vertical velocity at the bottom is given by the material derivative of the bottom. These boundary condition are called the kinematic boundary conditions,

$$w|_{z=\xi} = \frac{D\xi}{Dt} = \frac{\partial \xi}{\partial t} + u \frac{\partial \xi}{\partial x} + \frac{\partial \xi}{\partial y} \quad (\text{G.8})$$

$$w|_{z=-d} = u \frac{\partial d}{\partial x} + \frac{\partial d}{\partial y} \quad (\text{G.9})$$

When both kinematic boundary equations are substitute in the depth averaged continuity equations and applying the Leibniz rule of integration the equations becomes,

$$\frac{\partial \xi}{\partial t} = \frac{\partial UH}{\partial x} + \frac{\partial VH}{\partial y} \quad (\text{G.10})$$

Where U and V are the depth averaged velocities. This equation is used to determine the surface elevation and is called the global continuity equation.

In Xbeach-nh the depth averaged Navier stokes equations are solved. This can be done by integrating the momentum equations with respect to the depth. The procedure is very similar to the three momentum equation. Thus it is only showed for the x momentum equations(equation G.4). The integration is shown for different terms separately.

First the time derivative will be integrated,

$$\int_{-d}^{\xi} \frac{\partial u}{\partial t} dz = \frac{\partial}{\partial t} (HU) - u \frac{\partial \xi}{\partial t} \Big|_{z=\xi} - u \frac{\partial d}{\partial t} \Big|_{z=-d} \quad (\text{G.11})$$

The bottom will not change in the scale of the fluid motion. Therefore the last term can be neglected from the equation.

Secondly the advection terms are integrated. To do this the Leibniz rule of integration is used,

$$\begin{aligned} \int_{-d}^{\xi} \left(\frac{\partial u^2}{\partial x} + \frac{\partial uv}{\partial y} + \frac{\partial uw}{\partial z} \right) dz &= \frac{\partial}{\partial x} \left(HU^2 - \int_{-d}^{\xi} (u-U)^2 dz \right) \\ &\quad - \frac{\partial}{\partial y} \left(HUV - \int_{-d}^{\xi} (u-U)(v-V) dz \right) - u \left[u \frac{\partial z}{\partial x} + v \frac{\partial z}{\partial y} + w \right]_{z=-d}^{z=\xi} \end{aligned} \quad (\text{G.12})$$

When the last term is combined with G.11 the integration term cancel out. The term including the integral represent the dispersion of the flow. When the vertical velocities are small, these terms are close to zero and are neglected from the equation.

The depth integrated pressure term is given by (assuming atmospheric pressure of 0),

$$\int_{-d}^{\xi} \left(\frac{\partial q}{\partial x} + g \frac{\partial \xi}{\partial x} \right) dz = \frac{\partial (H\bar{q})}{\partial x} - \left[q \frac{\partial z}{\partial x} \right]_{z=-d}^{z=\xi} + gH \frac{\partial \xi}{\partial x} = \frac{\partial (H\bar{q})}{\partial x} + q \frac{\partial d}{\partial x} + gH \frac{\partial \xi}{\partial x} \quad (\text{G.13})$$

Where \bar{q} is the depth averaged dynamic pressure.

At least integrating the stress terms,

$$\frac{1}{\rho} \int_{-d}^{\xi} \left(\frac{\partial \tau_{xx}}{\partial x} + \frac{\partial \tau_{yx}}{\partial y} + \frac{\partial \tau_{zx}}{\partial z} \right) dz = \frac{1}{\rho} \frac{\partial}{\partial x} (H\bar{\tau}_{xx}) + \frac{1}{\rho} \frac{\partial}{\partial y} (H\bar{\tau}_{yx}) + \frac{\tau_{s,x}}{\rho} + \frac{\tau_{b,x}}{\rho} \quad (\text{G.14})$$

Where $\bar{\tau}$ are the depth averaged turbulent stresses, $\tau_{s,x}$ the surface stress and $\tau_{b,x}$ the bottom shear stress. These stresses can be related to the wind force and the bottom friction.

Combing equation G.10, G.11, G.12 and G.13 gives the depth averaged conservative momentum equation for the x-direction,

$$\frac{\partial}{\partial t} (HU) + \frac{\partial}{\partial x} \left(HU^2 + H\bar{q} - \frac{1}{\rho} H\bar{\tau}_{xx} \right) + \frac{\partial}{\partial y} \left(HUV - \frac{1}{\rho} H\bar{\tau}_{yx} \right) = -gH \frac{\partial \xi}{\partial x} - q \frac{\partial d}{\partial x} + \frac{\tau_{s,x}}{\rho} + \frac{\tau_{b,x}}{\rho} + \frac{F_{veg}}{g} \quad (\text{G.15})$$

Where F_{veg} is included as the vegetation force. The same equations can be derived for the y and z direction. These equations are given by,

$$\frac{\partial}{\partial t} (HV) + \frac{\partial}{\partial x} \left(HUV + H\bar{q} - \frac{1}{\rho} H\bar{\tau}_{xy} \right) + \frac{\partial}{\partial y} \left(HV^2 - \frac{1}{\rho} H\bar{\tau}_{yy} \right) = -gH \frac{\partial \xi}{\partial y} - q \frac{\partial d}{\partial y} + \frac{\tau_{s,y}}{\rho} + \frac{\tau_{b,y}}{\rho} + \frac{F_{veg}}{g} \quad (\text{G.16})$$

$$\frac{\partial}{\partial t} (Hw) + \frac{\partial}{\partial x} \left(HUW - \frac{1}{\rho} H\bar{\tau}_{zx} \right) + \frac{\partial}{\partial y} \left(HVW - \frac{1}{\rho} H\bar{\tau}_{zy} \right) = q_{bottom} - q_{surface} \quad (\text{G.17})$$

Besides of momentum equations also the (local) continuity equation is integrated over the depth. By applying the Leubniz rule of integrating, the following equation is obtained,

$$\frac{1}{\rho} \int_{-d}^{\xi} \left(\frac{\partial u}{\partial x} + \frac{\partial v}{\partial y} + \frac{\partial w}{\partial z} \right) dz = \frac{\partial HU}{\partial x} + \frac{\partial HV}{\partial y} + w|_{z=\xi} + w|_{z=-d} \quad (\text{G.18})$$

The global continuity equation to solve for the free surface is given as equation G.10.

G.3 Domain definitions

The domain of the model is bounded by the free surface, the bottom and by the four sides of the domain. Vertically the domain is bounded by a single values free surface ($z = \eta$) and the bottom ($z = -d$). The vertical zero axis is defined at the mean water level. Thus, the water level is defined as the elevation from $z = 0$ and the bottom is defined as the distance from $z = 0$ to the bed. This result in a total water depth of,

$$H = \eta + d \quad (\text{G.19})$$

An overview of the domain is given in figure G.1. In this figure the local and global coordinate system is shown. These coordinate system are related by anti-clockwise translation α .

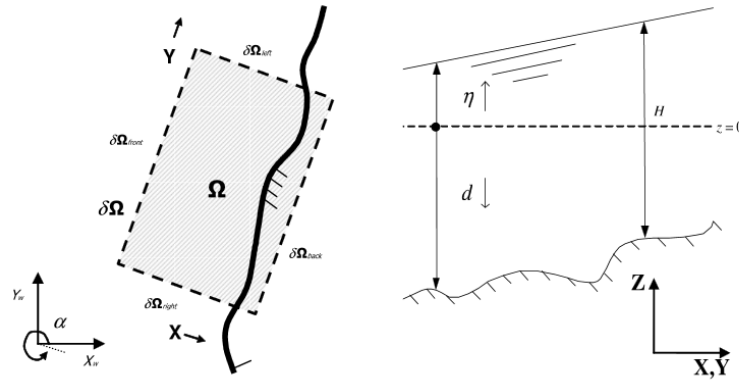


Figure G.1: Xbeach domain definitions.

These equations need boundary conditions to have a unique solution. The boundary conditions need to be determined for the free surface, the bottom and the four sides of the domain. The dynamic pressure at the free surface is assumed to be zero. This is already described in the previous section, where the dynamic pressure at the free surface is left out. If wind is included the wind stress can be specified at the free surface. The bottom shear stress is given as,

$$\tau_{b,x} = c_f \rho |U|U \quad \tau_{b,y} = c_f \rho |V|V \quad (\text{G.20})$$

Where c_f is the friction coefficient.

The four side boundaries can be specified as open or closed boundaries. A closed boundary means a no flow through to boundary. This is applied by setting the normal velocity to zero and setting the gradient of the tangential velocities to zero (free-slip condition). At the open boundaries the normal velocity is used as the boundary condition, whereas the gradient of the tangential velocities is set to zero.

G.4 Numerical domain

The numerical domain consist of multiple cells. A staggered arrangement is used for horizontal layout. This means that the velocities are not at the same location defined as the water level point. The advantage of a staggered arrangement is that an explicit method could be used to solve the coupled system. The cell centers represent the water level points and the middle of a cell faces the velocity points. The layout is shown in figure G.2.

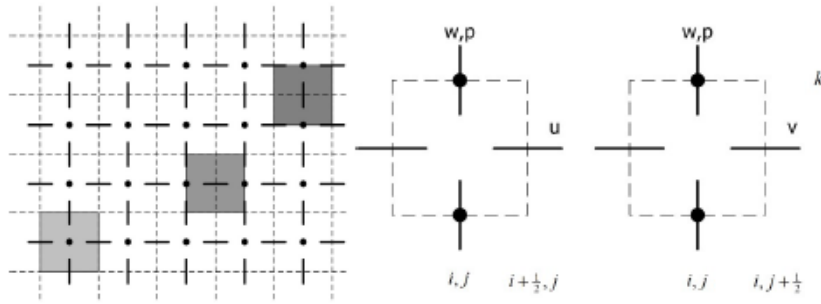


Figure G.2: Xbeach numerical domain.

The cell centers are defined at location $\mathbf{X}_{i,j}$ and is bounded by the lines $x_{i\pm 1/2,j}$ and $y_{i,j\pm 1/2}$, the bottom ($-d = -d(\mathbf{X}_{i,j})$) and the free surface ($\eta = \eta(\mathbf{X}_{i,j})$). The grid sizes are given by,

$$\Delta x_{i,j} = x_{i+1/2,j} - x_{i-1/2,j}, \quad \Delta y_{i,j} = y_{i,j+1/2} - y_{i,j-1/2}, \quad (\text{G.21})$$

The vertical layout layout is not staggered. The dynamic pressure, water level and bottom are all defined at the cell face. This approach is used to easily determine the boundary condition for the dynamic pressure. At the free surface the dynamic pressure is set to zero which means that only the dynamic pressure for the bottom needs to be computed. Stelling and Zijlema (2003) showed that this Keller box scheme is appropriate to model dispersive waves.

G.5 Breaking

Breaking is initiated when $\partial_t \eta / \sqrt{gh} < \alpha$ where α is a breaking steepness parameter. When this condition is met the cell becomes hydrostatic and a bore will develop. When breaking is initialized the α in the neighbor points is reduced to 0.3. This parameter is not changed within all the simulations. The breaking steepness is used to calibrate the model for the right location of the breaking point and can thus have a significant impact on the computation.